Performance of Direct Sequence Spread Spectrum Techniques for High Rate Communications in the High Frequency Band

by
Michel Drapeau, B. Eng.

A THESIS
submitted to the school of Graduate Studies and Research
in partial fulfillment of the requirements
for the degree of
MASTER OF APPLIED SCIENCE
in
Electrical Engineering

Ottawa-Carleton Institute for Electrical Engineering
Department of Electrical Engineering
Faculty of Engineering
University of Ottawa
Ontario, Canada

May, 1993

ISBN 0-315-89656-6

Canada

UNIVERSITÉ D'OTTAWA
UNIVERSITY OF OTTAWA

I hereby declare that I am the sole author of this thesis.

I authorize the University of Ottawa to lend this thesis to other institutions or individuals for the purpose of scholarly research.

Michel Drapeau

I further authorize the University of Ottawa to reproduce the thesis by photocopying or by other means, in total or in parts, at the request of other institutions or individuals for the purpose of scholarly research.

Michel Drapeau

Table of Contents

Abstract

For the last decade or so, major development in the fields of Large Scale Integration and Digital Signal Processing have revived the interest in the HF skywave channel (3 - 30 MHz) and more particularly in the use of wideband signalling to either increase the transmission rate or to improve the system efficiency. This thesis is aimed at the performance estimate of a wideband HF communication system using direct sequence spread spectrum.

In this study, an HF channel model referred to as the Ionospheric Parameter Model is implemented in software and used to simulate a variety of channel conditions. BER performance for a communications systems transmitting at a rate of 2400 bits per second is estimated through 'Monte-Carlo' simulations. More specifically, direct sequence spread spectrum combined with a RAKE receiver implementation is evaluated under quiet and disturbed ionospheric conditions. Performance is compared for different processing gains and levels of multipath diversity. Finally, performance obtained with the addition of block coding and convolutional coding with and without interleaving is provided.

To Corinne, Etienne, and Dominic

Acknowledgments

I would like to express my sincere appreciation to Mr. Claude Bilodeau of the Communications Research Centre for the numerous advice in helping me to solve many problems encountered throughout this work. I would like to thank him for the time spent on several fruitful discussions, on making constructive criticisms in reviewing this document, and foremost, for his patience and for his availability of all instant. Further, I wish to thank Dr. Gerard Nourry for providing me the opportunity to use the Communications Research Centre facilities, and my thesis supervisors Dr. Jean-Yves Chouinard and Dr. Abbas Yongaçoglu for their knowledgeable guidance throughout this thesis. Finally, I would like to thank my wife Corinne whose sense of humour and continuous support made this thesis possible.

List of Figures

List of Tables

List of Acronyms

AGARD	Advisory Group for Aerospace Research and Development
AWGN	Additive White Gausian Noise
BCH	Bose, Chaudhuri, and Hocquenghem Code
BER	Bit Error Rate
bps	bit per second
CCIR	Comité Consultatif International des Radiocommunications International Radio Consultative Committee
CDF	Cumulative Distribution Function
CDMA	Code Division Multiple Access
DPSK	Differential Phase Shift Keying
DSP	Digital Signal Processing
DSSS	Direct Sequence Spread Spectrum
FEC	Forward Error Correction
FH	Frequency Hopping
FIR	Finite Impulse Response
FSK	Frequency Shift Keying
GF	Galois Field
HF	High Frequency
I&D	Integrate and Dump
IIR	Infinite Impulse Response
IPM	Ionospheric Parameter Model
ISI	Inter-Symbol Interference
ITS	Institute for Telecommunication Sciences (US)
LSI	Large Scale Integration
MUF	Maximum Usable Frequency
NY	New-York
NWT	North-West Territories
PCA	Polar Cap Absorption

pdf	Probability Density Function
PG	Processing Gain
PN	Pseudo-Noise
PSK	Phase Shift Keying
QWSS	Quasi-Wide Sense Stationary
QWSS-US	Quasi-Wide Sense Stationary Uncorrelated Scattering
RS	Reed-Solomon Code
Rx	Receiver
SF	Spread Factor
SID	Sudden Ionospheric Disturbances
SNR	Signal to Noise Ratio
SNIR	Signal to Noise and Interference Ratio
TOA	Time of Arrival
Tx	Transmitter
WKB	Wentzel, Kramers, and Brillouin Solution
WSS	Wide Sense Stationary

List of Symbols

a_j	Amplitude of the jth interference signal; j = 1, ..., J
A	Amplitude of the transmitted signal
A_b	Amplitude of the information bit
A_c	Amplitude of PN chip
b_i	Amplitude of the ith impulsive noise component; i = 1, ..., I
$\hat{b}_k$	kth estimated received bit
B_D	Doppler spread
$(B_D)_n$	Doppler spread of the nth return
c	Speed of light in free-space: $c = 3.0 \times 10^8$ meter/second
$c_n(t)$	Time-varying tap gain of a transversal filter; n = 0, 1, 2, ...
$\tilde{c}_n(t)$	Sample of the Gaussian distribution; n = 0, 1, 2, ...
$c(t)$	Baseband spreading signal
C	Channel capacity
$C_n(f)$	Tap gain spectrum of the transversal filter; n = 0, 1, 2, ...
$C(t)$	Correlation factor
d_{min}	Minimum distance of a code
D	Distance between the terminals
e	Electronic charge
e_j	Error value of the jth error; j = 1, ..., t
el./m^3	Number of electrons per cubic meter
E_b	Energy per bit
E_{Jc}	Energy of the interference per chip
E_s	Sporadic-E layer
f	Frequency
f_c	Carrier frequency
f_j	Frequency of the jth interference; j = 1, ..., J
f_N	Plasma frequency
f_p	Penetration frequency

$(f_p)_n$	Penetration frequency of the nth return; $n = 0, 1, 2, ...$
f_r	Reflection frequency at oblique incidence
$f_R(r)$	PDF of a Rayleigh distribution
f_v	Reflection frequency at vertical incidence
$f_X(x)$	Probability density function (pdf) of a random variable 'x'
$F_X(x)$	Cumulative distribution function (CDF) of a random variable 'x'
$g(x)$	Generator polynomial
$G(t)$	Time-varying white Gaussian noise component
h	Height of reflection
$\bar{h}_n(f)$	Virtual height of reflection of the nth return; $n = 0, 1, 2, ...$, as a function of frequency
h_o	Height of maximum ionization
$(h_o)_n$	Height of maximum ionization of the nth return; $n = 0, 1, 2, ...$
$\|H_B(f)\|^2$	Squared magnitude of the low-pass Butterworth filter
$H_n(f)$	Transfer function of the nth return; $n = 0, 1, 2, ...$
$\|H_n(f)\|$	Magnitude of the transfer function of the nth return; $n = 0, 1, 2, ...$
$H(f,t)$	Time-varying transfer function
Hz	Hertz = Cycle per second
$I(t)$	Time-varying impulsive noise component
$J(t)$	Time-varying interference component
J_o	Average interference density
k	Number of information bits (or symbols) per codeword
kHz	Kilohertz (10^3 Hertz)
km	Kilometer
l	Interleaving degree
L	Level of diversity
m	Degree of the PN sequence
m	Constraint length of the convolutional code
m_e	Mass of an electron
msec	Millisecond

MHz	Megahertz (10^6 Hertz)
n	Number of bits (or symbols) per codeword
N	Cyclic period of a PN sequence
N_e	Electron density
N_I	Number of impulsive noise components
N_J	Number of interference components
N_o	Average noise density
$N(t)$	Time-varying complex wideband noise function
O	Ordinary wave
$p(t)$	Baseband data signal
P_b	Probability of bit error
$P'(f)$	Group path as a function of frequency
$P_m(x)$	Primitive polynomial of degree m
$r(t)$	Baseband received signal
$r(x)$	Received codeword polynomial
R_b	Transmission rate or bit rate
R_c	Chip rate
R_{min}	Minimum transmission rate
R_s	Sampling rate
$s(t)$	Transmitted signal
$s(x)$	Codeword polynomial to be transmitted
S_k	kth decoding syndrome
$S(\tau;\nu)$	Scattering function
$S_c(\Delta f;\nu)$	Doppler power spectrum
$S_b(f)$	Power spectrum of the data signal
$S_c(f)$	Power spectrum of the spread signal
$T(\tau)$	Delay amplitude factor
t	Time
t	Number of bits (or symbols) a code can correct
t_i	Arrival time of the ith noise impulse

T_b	Signaling interval or bit period
T_c	Chip period
T_m	Multipath spread
T_n	Delay dispersion of the nth return; $n = 0, 1, 2, ...$
T_s	Sampling period
$T(\tau)$	Delay amplitude function for the IPM model
$(T_\tau)_n$	Delay dispersion from $(\tau_L)_n$ to τ_n
$u(t)$	Square-pulse signal
$u(x)$	Information data polynomial
$U[n]$	nth sample of a uniformly distributed sequence
$v(t)$	Baseband modulated signal
W	Signal bandwidth
W_{ss}	Spread bandwidth
α_n	Amplitude of the nth return; $n = 0, 1, 2, ...$
$\alpha_n(t)$	Time-varying attenuation of the nth return; $n = 0, 1, 2, ...$
β	Roll-off factor for the band-limiting filter
βj	Error location of the jth error; $j = 1, ..., t$
χ	Solar zenith angle
Δf	Frequency interval
$(\Delta f)_c$	Coherence bandwidth
Δf_j	Frequency difference between the jth interference and f_c; $j = 1,..., J$
Δt	Time interval
$(\Delta t)_c$	Coherence time
$\Delta\phi_j$	Phase difference between the jth interference and the legitimate signal; $j = 1,..., J$
ε_o	Permittivity of free-space: $\varepsilon_o = \frac{10^{-9}}{36\pi}$ farad/meter
ϕ_n	Angle of incidence with respect to the vertical at the nth layer; $n = 0, 1, 2, ...$
$\phi_s(\tau, \nu; t)$	Phase function for the Ionospheric Parameter Model
ϕ_τ	Phase shift associated with a median delay τ

γ_b	Signal-to-noise ratio (SNR) per bit
$\bar{\gamma}_b$	Average Signal-to-noise ratio (SNR) per bit
γ_{Jb}	Signal-to-noise-and-interference ratio (SNIR) per bit
η	Refractive index
η_n	Refractive index of the nth layer; $n = 0, 1, 2, ...$
η_r	Refractive index at the reflection point
$\varphi_c(\Delta t;\Delta f)$	Channel auto-correlation function
$\varphi_c(\tau;\Delta t)$	Multipath intensity profile
$\varphi_c(\tau, \nu; t)$	Channel auto-correlation function for the IPM model
$\varphi_{PN}(\tau)$	Auto-correlation of the PN sequence
ϑ	Collision frequency
$\Lambda(x)$	Error-locator polynomial
μ_o	Permeability of free-space: $\mu_o = 4\pi \times 10^{-7}$ Henry/meter
μsec	Microsecond
ν	Doppler shift
$(\nu_L)_n$	Doppler shift at $(\tau_L)_n$ of the nth return; $n = 0, 1, 2, ...$
ν_n	Doppler shift of the nth return; $n = 0, 1, 2, ...$
$\nu_n(t)$	Time-varying Doppler shift of the nth return; $n = 0, 1, 2, ...$
ν_t	Doppler shift at time 't'
π	Pi = 3.14159...
θ	Phase shift
$\theta_n(f)$	Phase shift of the nth return as a function of frequency; $n = 0, 1, 2, ...$
$\theta_n(t)$	Time-varying phase shift of the nth return; $n = 0, 1, 2, ...$
σ	Layer Thickness
σ_n	Layer thickness of the nth return; $n = 0, 1, 2, ...$
τ	Delay
$\tau(f)$	Median delay as a function of the frequency
$(\tau_L)_n$	Minimum median delay of the nth return; $n = 0, 1, 2, ...$
τ_n	Median delay of the nth return; $n = 0, 1, 2, ...$

$\tau_n(f)$	Median delay of the nth return as a function of frequency; $n = 0, 1, 2, ...$
$\tau_n(t)$	Time-varying median delay of the nth return, $n = 0, 1, 2, ...$

Chapter 1
Introduction

1.1 Background

From the first radio link established between Newfoundland and England by Marconi in 1901 to the advent of satellite communications in the early 70's, the use of the skywave medium was the principal means of achieving communications by over-the-horizon radio links. From the onset of that period, use of the property of the ionosphere to refract radio waves in the frequencies ranging from 3 to 30 MHz, offered the fantastic opportunity for communicating overseas. However, the lack of technology to mitigate the detrimental effects of severe signal fading caused by the ionosphere's dynamic behavior and multipath characteristics resulted in poor communications reliability. These facts have long helped promote the skywave medium as being an "unavoidable necessity" where only limited transmission rates could be achieved. Indeed, a transmission rate of 75 bauds over the regulated 3 kHz bandwidth has been the de facto standard for a significant period of time.

The advent of satellite communications has opened new horizons in the field of long range communications. Because the satellite communications channel does not suffer from extensive multipath fading that the ionospheric medium produces, much higher transmission rates with better reliability are possible. The future of HF skywave communications was then considered limited and many believed that long-range communications would depend exclusively on satellites.

Since the early 70's, phenomenal improvements in Large Scale Integration (LSI) and Digital Signal Processing (DSP) techniques combined with several advantages of HF systems such as their low implementation cost, their improved security, and their wide coverage, have altered the way of looking at this venerable medium and revived the interest in it. The use of adaptive channel equalization and Forward Error Correction (FEC) techniques, originally developed for land line communications, have brought the standard transmission rate of current HF modems from 75 bits per second (bps) to a respectable 2400 bps.

Research has obviously not stopped there and still considerable efforts are being spent at looking for techniques that will either increase the transmission rate or improve the 3 kHz channel's reliability. Although a bandwidth of 3 kHz has long represented a compromise between accommodating as many users as possible within a 30 MHz wide spectrum and providing sufficient bandwidth for transmitting voice with analog-based

technologies, bandwidth may become one of the limiting factor as modem performance reaches the theoretical bound for the channel capacity defined by Shannon under the well-known relation:

$$\frac{C}{W} = \log_2[1 + \gamma_b]; \tag{1.1}$$

The use of a wider bandwidth ($W >> 3$ kHz) appears as a potential alternative for satisfying future channel capacity requirements. However, it presents system designers two additional problems that can usually be neglected for systems operating over a 3 kHz bandwidth. These are that delay dispersion of the individual signal returns cannot be ignored for wideband signals and that interference due to spectrum congestion become particularly important.

While these problems have been known for years, and numerous solutions to mitigate their detrimental effects have been designed and implemented successfully on communications systems operating over other frequency bands, the difficulty of testing these over the HF channel remains. The spectrum congestion prevents system designers from conducting extensive field tests and the variability of the channel makes comparison between results difficult. These facts have forced researchers to look for other methods to estimate system performance and brought them back to the more basic problem of adequate modeling of wideband HF channels.

1.2 Channel Modeling

Among the different methods offered to system designers for estimating system performance, analytical methods are certainly the most appealing because of the reduced amount of processing required. However, when performance evaluations are required over a full range of realistic conditions, analytical evaluations become intractable and "Monte-Carlo" type simulations with an appropriate channel model are the only remaining option.

For years, simulations of the HF channel have been based on the model proposed by Watterson in 1970 [Watt70]. Despite its important restrictions regarding its bandwidth applicability and the assumed stationarity of the channel, the Watterson model has been used as the standard within the HF community for comparing HF modem performance. In its original paper, Watterson stated that his model was representative of the HF channel for bandwidths less than 12 kHz. Subsequent papers by other researchers questioned this statement and concluded that a more conservative bandwidth of 3 kHz was a more appropriate limit on its validity [Vogl88b]. In addition, it was clearly demonstrated that the assumed stationarity of the channel encompasses only a very restrictive number of conditions [Vogl88a].

Based on this information, the CCIR suggested that the Watterson model, although providing a simple model for a basis of comparison, be used with caution in drawing conclusions [CCIR90]. With these limitations in mind and the emerging trend of using more bandwidth, research in the field of wideband HF modeling has gone through increasing activity over the last few years. Several papers have been published on the subject. Some of them proposed only minor modifications to the Watterson model to account for delay dispersion effects[1] [Bern91]; but, others have proposed completely new approaches [Vogl88b] [Mala81].

The channel model adopted here for carrying out the simulations of this thesis was proposed by Vogler and Hoffmeyer in 1988 [Vogl88a]. The model is known as the *"Ionospheric Parameter Model"* (IPM). It has the advantage of being relatively easy to implement in software while being based on a minimum number of assumptions regarding the channel statistical behavior. It is therefore possible to simulate skywave channels over a wide variety of conditions and bandwidths, and to thoroughly evaluate several types of wideband modem implementations under the same statistical conditions.

1.3 Channel Mitigation Techniques

Many techniques are available for mitigating the effects due to signal band-limiting and to the time-varying multipath characteristic of the wideband skywave channel. Price and Green published in 1958 their well known paper on the RAKE receiver [Pric58]. This receiver exploits channel in-band diversity by discriminating between different channel returns and has the double advantage of mitigating the effects of multipath fading and inter-symbol interference (ISI). Later, Turin demonstrated that the RAKE implementation when used in conjunction with direct sequence spread spectrum (DSSS) techniques is nearly optimum in a multipath environment [Turi80]. Subsequently, the capability of the HF channel to support wideband transmission was the next logical question to answer before more efforts be put in maximizing performance.

That question was answered by Perry in the early 80's. He showed that the HF channel could support bandwidths in the order of 1 MHz and that wideband adaptive equalization was effective against ISI introduced by delay dispersion [Perr83]. Based on Perry's work and knowing that the advance in technology would make viable the implementation of DSSS RAKE receivers, Bello presented an estimate of the performance for different RAKE implementations over a 1 MHz bandwidth, [Bell88], [Wagn89]. Although his estimate was for transmission rates of 75 bps and quiescent channel condi-

1. Delay dispersion inflicting each return is also present over a 3 kHz bandwidth but, it is negligible when compared to the signalling period.

tions, the results showed promises in the use of such implementation for high transmission rates.

Besides providing robustness against interferences and multipath fading, the use of spread spectrum allows several users to share a common portion of the spectrum through Code Division Multiple Access (CDMA), [Purs87], [Ziem85]. CDMA, although not covered in this thesis, is an additional advantage of spread spectrum techniques which is worth considering in view of the limited spectrum availability in the HF band.

1.4 Outline of the Thesis

The aim of this thesis is twofold. The first point consists of implementing in software a wideband HF channel simulator. The second point evaluates and compares bit error rate (BER) performance of a Direct Sequence Spread Spectrum HF modem under a variety of simulated channel conditions. Focus is placed on comparing RAKE receivers having different number of taps. Information rate is set at 2400 bps and moderate processing gains are tried. The simulations are carried out at baseband where perfect synchronization and perfect delay estimate are assumed. Different FEC techniques are also used and compared. Previous works published on coding have clearly stated the potential of using interleaving for optimizing the FEC performance, [Cohn68], [Bray68]. Interleaving is therefore implemented in a number of simulations with error correction coding.

The main body of this thesis is divided into four chapters. Chapter 2 provides a brief description of the physical constituents of the ionosphere in order to understand the role of the different parameters affecting radio wave propagation. Analytical characterization of the stochastic process taking place during transmission with a description of the channel models currently being used to conduct system simulations follow. Emphasis is given on the description of the Ionospheric Parameter Model used for carrying out the simulations. Finally, the problem of wideband noise is addressed and a model for representing it is summarized.

Chapter 3 provides an overview of the theory related to spread-spectrum and FEC techniques. The advantages of using spread-spectrum and the method for implementing direct-sequence spread spectrum are presented. Pseudo-noise sequences are briefly addressed and the advantages of exploiting multipath diversity are covered through the description of the RAKE receiver. Finally, the fundamentals of error control coding are summarized. Block coding and convolutional coding with their respective decoding techniques, namely the Berlekamp and the Viterbi algorithms, are presented. A description of different interleaving techniques concludes the chapter.

Chapter 4 provides an exhaustive description of the method used for simulating in software the wideband HF links. The transmitter and the receiver implementations as well as the method used to simulate the HF skywave channel are treated. Since scattering functions provide a good representation of the channel conditions, some have been selected and are presented in Chapter 5 for each type of channel being simulated. Finally, the results obtained through "Monte-Carlo" simulations are provided and analyzed.

A chapter summarizing the findings and suggesting numerous areas where further research could be oriented, completes the thesis. Finally, three appendices provide substantial information on specific topics. They respectively cover the derivation of the refractive index of the ionosphere, the Breit and Tuve and the Martyn's theorems, and an IIR filter implementation for a Rayleigh fading source. An extensive bibliography is also provided at the end for reference.

Chapter 2
The Ionospheric Medium and its Models

2.1 Introduction

Communications in the HF band i.e., in the frequencies ranging from 3 MHz to 30 MHz, make extensive use of the refracting properties of the ionosphere to achieve transmission over the curvature of the earth. The success achieved on such links is dependent upon the physical structure of the ionosphere and the performance of the communication systems. It is therefore important to understand the different processes involved in radio wave propagation in order to assess their relative importance and to be able to characterize them; the goal is to develop a representative model of the channel which may be used to evaluate and compare different system implementations.

In this chapter, a brief description of the physical constituents of the ionosphere is presented. Sections 2.2 and 2.3 provides the required knowledge to understand the role of the different parameters affecting radio wave propagation through the ionosphere. Section 2.4 provides a review of the analytical characterization of the stochastic process taking place during transmission, while Section 2.5 presents a description of the channel models currently being used to conduct system simulations. Emphasis is given on the description of the Ionospheric Parameter Model, which is used for carrying out the simulations presented in this thesis. Finally, a model for representing broadband noise within the channel is summarized in Section 2.6.

2.2 The Ionosphere

The ionosphere is a part of the atmosphere from about 50 km to roughly 2000 km in altitude in which free ions exist in sufficient quantities to affect the propagation of short waves. Based on its electron density, the ionosphere has been divided into three major regions termed D, E, and F [Davi65]. Research that followed the discovery of those three regions, showed that under special conditions further subdivisions were required to identify minor regions where significant variations of the physical and propagation properties occur. These minor regions were termed E_n and F_n (n = 1, 2, 3...) according to their similarity with the E and F region respectively. Figure 2.1 [CCIR82b] depicts a simplistic view of the different regions of the ionosphere that can be observed during a typical 24-hour cycle.

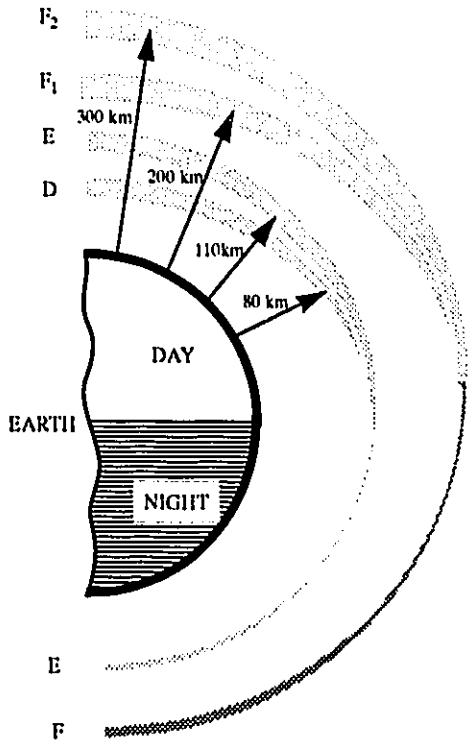

FIGURE 2.1. The Ionospheric Regions

2.2.1 The Ionization Process

The sun plays a major role in the level of ionization of the atmosphere. More specifically, solar electromagnetic radiation in the ultra-violet and X-ray portions of the spectrum as well as energetic charged solar particles are among the principal sources of ionospheric ionization. The dependence of the ionization process from the sun may be better observed by the rate at which ionization occurs during typical solar cycles.

The rate of ionization depends upon two factors: the intensity of the radiation, and the density of the atmospheric gas atoms and molecules [Boit83]. The intensity of the radiation translates into the radiation ability to free electrons from neutral atmospheric gases; while the density of the atmosphere determines the maximum number of ionized particles that can be produced. These two factors evolve however in an opposite manner. As radiation go deeper into the atmosphere, the radiation is absorbed and its intensity decreases; conversely, the atmospheric density increases as the altitude decreases. These phenomena result in an ionization rate which increases up to a certain altitude and, then, decreases as the atmospheric gas atoms and molecules become rarified.

Figure 2.2 [Boit83] shows a characteristic profile of the electron density as a function of altitude. Maximum atmospheric ionization occurs when radiation reach the

lower layers of the atmosphere with sufficient energy. This, usually, happens when the atmospheric path is the shortest; thus, at noon local-time or, in other words, at a solar zenith angle, χ, equal to zero.

2.2.2 Collision Frequency

The electron density N_e does not increase indefinitely through the ionization process but is counter-balanced by collisional recombinations of electrons and positive ions, and by the attachment of electrons to neutral atoms and molecules. Although the latter process produces ionized particles, their large mass prevents them from playing any significant role in radio wave propagation.

The number of collisions between atmospheric particles is also an important factor to consider because of the role it plays in radio wave attenuation. In general terms, the collision frequency, ϑ, which is defined as the average number of collisions per unit of time within a specified unit of volume, decreases with increasing altitude. Figure 2.2 shows a characteristic profile of ϑ as a function of the altitude. Figure 2.2 shows that ϑ decreases rapidly up to an altitude of 250 km. The light increase after this point with an inflection point around 350 km is due to the large number of electrons at this altitude.

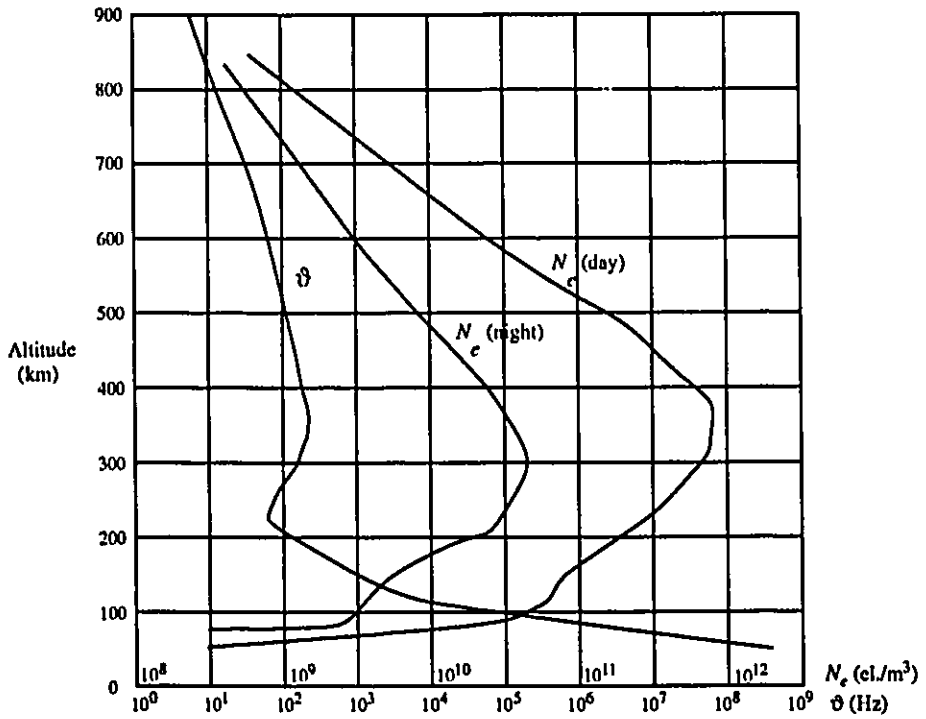

FIGURE 2.2. Variation of Electron Density and Collision Frequency with Altitude

2.2.3 Ionospheric Layers

The three major regions of the ionosphere, whose characteristics have significant impact on radio wave propagation, display time, geographical, and seasonal variations as well as a strong solar cycle dependence. In addition, the region characteristics are continuously varying in a random manner and their constituents are not homogeneously spread throughout. Discontinuity in the density of electrons and other particles are often observed, and lead to unexpected propagation behaviors [Good90].

D Region

The D region is located between an altitude of 50 km and 90 km. It displays a low average electron density due to the joint effect of an high collision frequency and a low ionization rate. The high collision frequency is representative of the important density of particles at this altitude while the low ionization rate reflects the receptions of radiations heavily absorbed by the upper layers of the atmosphere. The D region is a day-time only phenomenon and its maximum ionization rate occurs at noon local-time with a seasonal maximum during summer. Its role in HF communications is mainly absorptive [Masl87].

E Region

The E-region which includes the 'normal' and the 'sporadic' E layers, is located at altitudes that range from 90 to 130 km. The 'normal' E-layer displays a strong solar zenith angle dependence with a maximum ionization rate at noon, and a seasonal maximum in summer. Its level of ionization becomes negligible at night.

The sporadic E layer, E_s, may be described as clouds of high ionization level which refract radio waves at frequencies that usually travel through the 'normal' E layer. These clouds are strongly latitude dependent; for instance, the E_s layer is mainly a night phenomenon at high latitudes while it becomes a day-time phenomenon at equatorial latitudes.

Depending on the operating frequency, the role of the E region is twofold. If the operating frequency is low enough, the region acts as a reflector. On the other hand, if the operating frequency exceeds a certain value, the region does not bend the incoming radio wave sufficiently and the wave escapes the E region to continue its course toward upper regions. In this case, the E region becomes mainly absorptive. The difference between the absorption process of the E region and the D region stands in the fact that the electron density is sufficient in the E region to diffract the incoming waves [Budd61]. Absorption, where noticeable diffraction occurs, is referred to as deviative absorption and results in a higher angle of incidence of the radio wave at the upper ionospheric regions.

F Region

The F region extends upward from 130 km to the ionosphere limit and can be divided during day-time into the F_1 and the F_2 layers. The F_1 layer, which extends from 130 km to 210 km, displays similar characteristics as the 'normal' E layer, and merges with the F_2 layer at night.

The F_2 layer is the highest ionospheric region and is the major refracting region for HF communications. Its electron density profile does not display solar zenith angle dependence as the other regions; rather, it reaches its maximum later in the afternoon. This may be explained by the low collision frequency which allows the particles to keep received solar energy for several hours.

The F_2 layer is also characterized by a seasonal maximum in winter and by embedded irregularities in its electron distribution. These irregularities, which cause reflected pulses to have much longer duration than the transmitted pulses, happen particularly at night and are referred to as spread-F phenomena.

2.2.4 Ionospheric Disturbances

As mentioned before, the characteristics of each region of the ionosphere display a strong solar dependence. Hence, strong solar phenomena such as flares have serious effects on the physical behavior of the ionosphere. These effects may be catastrophic for HF communications systems by causing service interruptions that may last for days. Among the major disturbances, sudden ionospheric disturbances (SID) ionospheric storms, and polar cap absorption (PCA) are certainly the most important. Figure 2.3 [Masl87] lists these disturbances and their causes.

Sudden Ionospheric Disturbance

Sudden bursts of solar energy may produce abnormal ionization in the different layers of the ionosphere. Usually, the D-region ionization rate is the factor that is affected the most. This results in a higher density of particles in the region than usual. Thus, the probability of collision increases and so does the level of absorption.

Ionospheric Storms

Ionospheric storms are caused by streams of solar charged particles deflected by the earth's magnetic field toward the auroral zone. They result in a higher absorption in the D region and an expansion of the F_2 layer. The latter phenomenon causes a decrease of the frequency at which a reflection usually occurs and an increase of the time disper-

sion. Ionospheric storms are usually accompanied by auroral effects and by abnormal fluctuations of the earth's magnetic field, referred to as magnetic storms.

Polar Cap Absorption

Following a major solar flare, solar protons guided by the earth's magnetic field toward the polar regions increase the D-region ionization. The increase in the ionization level results in strong absorption and may cause total radio blackout for up to a day.

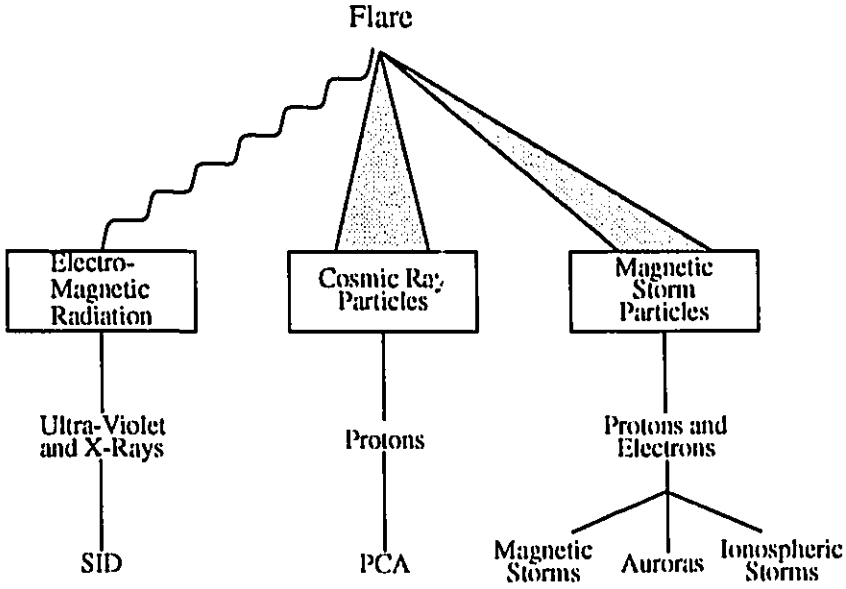

FIGURE 2.3. Ionospheric Disturbances

2.3 Wave Propagation in the Ionosphere

When a radio wave is transmitted, the energy may be radiated in several directions and at different elevation angles depending on the antenna directivity and its side-lobe pattern. However, it is possible to approximate the situation with the view of having the radiated energy travel along a number of distinct rays [Schw66] as shown in Figure 2.4. Each of the rays, while traveling through the ionosphere, experiences different processes which impinge on its transmission path and its attenuation. In addition of being absorbed and delayed, the rays may be refracted, be split, or may simply cross the layers and be lost.

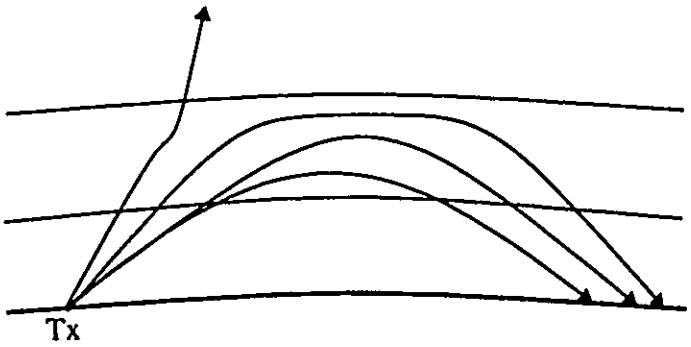

FIGURE 2.4. Example of Possible Ionospheric Ray Paths

2.3.1 Radio Wave Refraction

A ray traveling through the ionosphere traverses a continuum of layers each having a different electron density N_e. As shown in Appendix A, the electron density is related to the refractive index, η, of the medium through the Appleton-Hartree formula [Budd61]. In the absence of collision and of the earth's magnetic field[1], the formula simplifies to:

$$\eta^2 = 1-\left(\frac{f_N}{f}\right)^2 , \tag{2.1}$$

where f_N is the plasma frequency given by:

$$f_N = \frac{N_e e^2}{2\pi\varepsilon_0 m_e}. \tag{2.2}$$

Equations 2.1 and 2.2 show an inverse relationship between the refractive index η and the electron density N_e. Referring to Figure 2.2, it can be observed that the electron density increases steadily for altitudes under the F_2 layer; i.e., under about 350 km during daytime and 300 km at night. It can therefore be deduced that the refractive index will display a decreasing profile for a fixed frequency f as the altitude increases up to that layer.

From optics, it is well known that electro-magnetic waves traveling through media of different refractive indexes are refracted at their boundaries. The refraction process is described by the Snell's law which may be expressed as:

$$\eta_0 \sin\phi_0 = \eta_1 \sin\phi_1 = \ldots = \eta_n \sin\phi_n; \tag{2.3}$$

1. The general expression for the refractive index of the ionosphere where the collisions and the earth's magnetic field are considered may be found in Appendix A.

where ϕ_n are the angles of incidence with respect to the vertical at the layer transitions and η_n are the refractive indexes of each of the different layers [Masl87]. The whole process may be seen at Figure 2.5.

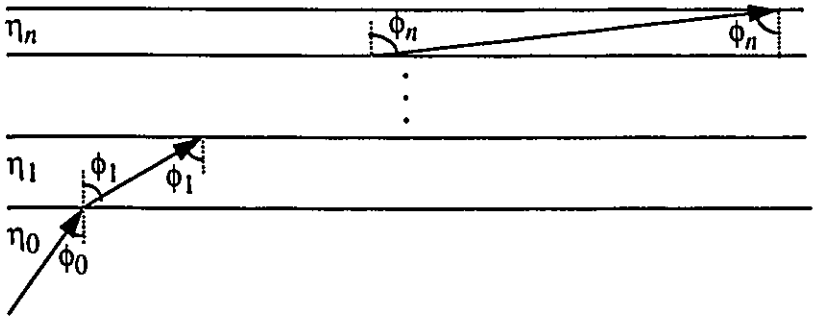

FIGURE 2.5. Refraction in a Layered Medium.

Equation 2.3 shows that decreasing the refractive index results in increasing the angle of incidence of the incoming ray. Hence, a ray transmitted at oblique incidence is gradually bent down as it travels through the ionosphere. If the ionosphere thickness is sufficient, the angle of incidence of the ray will increase up to 90 degrees. At this point, the ray will start going downward as it would have been reflected by a mirror, allowing communications links around the curvature of the earth to be achieved.

2.3.2 Frequency Dependence of HF Propagation

Equation 2.1 showed a dependence of the refractive index on the frequency of the radio wave. As the frequency is increased, the refractive index tends toward unity more abruptly and sufficient ray bending to cause a reflection ceases to occur; i.e., the ray continues its course and eventually escapes the ionosphere. The maximum frequency at which a reflection is still possible, is referred to as the penetration frequency, f_p, or the maximum usable frequency (MUF). The angle of incidence, ϕ_0, of the ray entering the first layer of the ionosphere plays a role in determining the MUF. From (2.3), it is possible to determine the refractive index at which reflection occurs in terms of the angle of incidence.

If the refractive index under the ionosphere is assumed to be unity[1], the refractive index at the reflection point; i.e., the point at which the angle of incidence ϕ_n is 90^0, may be expressed as:

$$\eta_r = \sin\phi_0. \tag{2.4}$$

1. Although the refractive index of the atmospheric layers other than the ionosphere is not exactly unity (the refractive index of free-space), it is usual to assume so for radio waves in the HF band [Budd61].

Equations 2.1 and 2.4 may then be used to derive the reflection frequency f_v for the case of vertical incidence, and the reflection frequency f_r for oblique incidence ϕ_0. Using (2.4), the refractive index at the reflection point for a ray transmitted at vertical incidence; i.e., $\phi_0 = 0$, is equal to zero. Equation 2.1 indicates that the refractive index is zero when the frequency is equal to the plasma frequency, f_N. Replacing f_N by f_v and η by (2.4) in (2.1) leads to the desired relation:

$$f_r = f_v \sec\phi_0. \tag{2.5}$$

The above expression, known as the secant law [Davi65] implies that the more oblique a radio wave is, higher is the frequency at which a reflection is possible.

2.3.3 Delay Distortion

The time taken by a particular ray to travel some distance introduces an average transmission delay that is often termed 'median path delay'. Because the path followed by a particular ray is dependent on its frequency, the median path delay is also a function of frequency. The theorems of Breit and Tuve, and Martyn covered in Appendix B provide the means to determine the group path P' (path length) followed by a ray, and thereby the frequency-dependent median path delay $\tau(f)$ by[1]:

$$\tau(f) = \frac{P'(f)}{c}; \tag{2.6}$$

where c is the speed of light in free-space; and $P'(f)$ is the group path at frequency f.

Figure 2.6 shows an hypothetical ionogram for a long-range HF communications link in which the dependence of the median path delay upon the frequency can be observed.

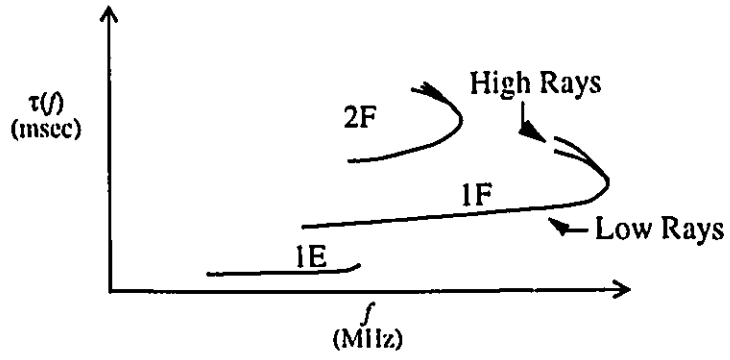

FIGURE 2.6. Hypothetical Ionogram

1. The curvature of the earth and a wave velocity slightly smaller than the speed of light introduce a factor which is omitted here and in the characterization of the communications channel in general. The interest is more on the differential delays between each ray than their absolute delay.

The delay dependence upon frequency is a major factor to consider when designing communications systems using large bandwidths. Because the propagation delay is not the same for all frequency components across the signal bandwidth, waveform distortion is observed within each return. It must be noted that delay distortion constitutes one of the most limiting impairments to data transmission over the wideband HF channel.

2.3.4 Multipath Propagation

As mentioned before, the energy reaching the receiver may be viewed as arriving in the form of a set of distinct "rays". According to the secant law and due to the non-homogeneity of the ionosphere structure, a varying number of these rays may be reflected from different heights, and may follow distinct paths that connect to the same receiving point. The received signal becomes the resultant of all the skywave returns dispersed in time; i.e., the received signal is a set of attenuated and delayed replicas of the transmitted signal.

Figure 2.7 shows some of the possible skywave returns that can be received simultaneously[1].

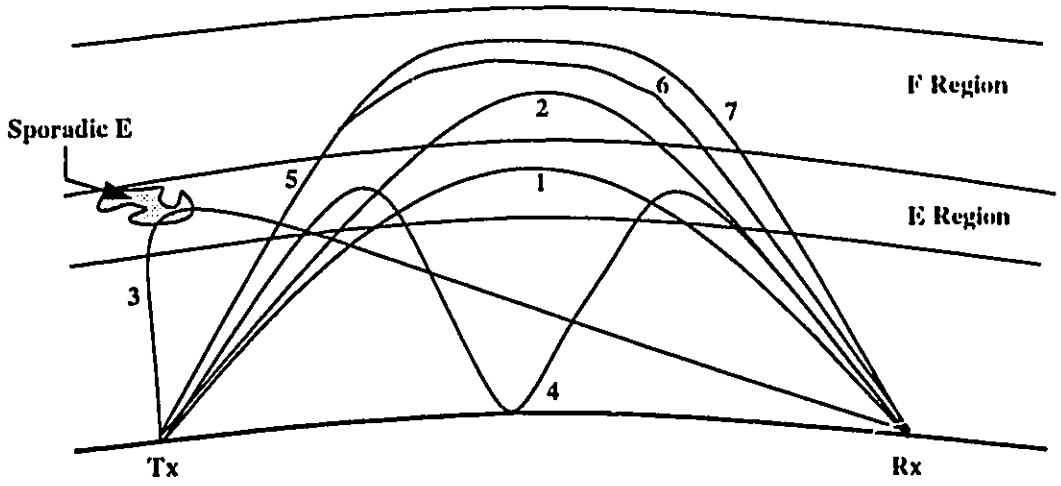

FIGURE 2.7. Example of Multipath Propagation

Transmitted rays may be reflected by the different ionospheric regions or by ionospheric irregularities such as sporadic E layers, and may achieve single-hop links with the receiver (rays 1, 2, 3 and 5). Furthermore, the earth surface being a good reflector for radio waves, multi-hop links may also be achieved (ray 4). In addition, Figure 2.7 shows that two returns are possible from the same ionospheric region when the operating fre-

1. Ground wave links are being omitted in Figure 2.7 and are not considered in this thesis.

quency is close to the MUF. These two returns referred to as the low and the high rays respectively, are often observed in the upper part of the F region (rays 2 and 5). Finally, the same ray may be split in two (rays 6 and 7) under the effect of the earth's magnetic field. This phenomenon known as magneto-ionic splitting will be discussed in the next sub-section. Although an infinite number of returns may be received, most of them are heavily attenuated and only a few are effectively detected; the others being accounted as loss in the path link budget [Masl87].

2.3.5 Absorption, Dispersion, and Ray-Splitting

In the previous sub-sections, the collisions between particles and the earth's magnetic field were neglected in order to focus on the dependence of the refractive index, η, upon the electron density, N_e, and the carrier frequency, f_c. These two factors, however, play a significant role in skywave propagation and must be considered to fully characterize the process.

Rays traveling through the ionosphere impart a quantity of their energy to the electrons present in the atmosphere. The electrons dispose of this energy either by re-radiating it in different directions or by dissipating it into heat during collisions with other particles. The former process leads to signal scattering and results in returns that are diffused over a certain period of time. The latter process is related to signal attenuation. Attenuation, which is mainly a D-region phenomenon, is directly proportional to the collision frequency. Hence, the more the electrons collide, the greater is the attenuation.

In addition to the transfer of energy, the ray traveling through the ionosphere creates an electric field which exerts a force onto the electrons. This force added to the force induced by the earth's magnetic field imparts a motion to the electrons which follow a helical path parallel to the electric field. This phenomenon results in two significant propagation effects: polarization mismatches and ray-splitting.

Because electrons follow an helical path, their re-radiated energy tends not to have the same polarization as the incident waves. Thus, the polarization of the resultant wave, which consists of the vectorial sum of the incident wave with a portion of the re-radiated waves, changes continuously as it traverses the ionosphere [Masl87]. The probability that the polarization of the transmitting and the receiving antennae be the same becomes quite small; resulting in signal fading due to polarization mismatches.

Secondly, as the electrons are travelling the helical path, they are submitted to forces which either increase or decrease the radius of the helix depending on their sense of rotation, thus creating two streams of electrons. The two streams form the magneto-ionic components which are referred to as the ordinary, O, and the extraordinary, X, waves; the extraordinary wave being the one for which the radius of the electronic stream is

increased. Although the two waves travel as separate entities, they are very similar, except for a larger attenuation for the X wave. Indeed, they become distinguishable[1] only in the upper F-region as shown in Figure 2.7.

2.4 Channel Characterization for Communications

For communications applications, the ionosphere is recognized as being a time-variant dispersive channel which behaves in a random manner. The channel must therefore be characterized statistically based upon the different phenomena which affect the signal waveform [Proak89], [Stei87], and [Schw66]. Among them, dispersion, which occurs in both the frequency and the time domains, results in signal distortion that may be observed through inter-symbol interferences, ISI, and fading phenomena. ISI is exclusively related to the time dispersion which is a consequence of the multipath characteristic of the medium. Fading, on the other hand, may have several causes including mutual interferences between returns, movements and irregularities of the ionosphere which result in Doppler phenomena and frequency dispersion, variations of the signal absorption, and rotations of the axes of polarization.

A statistical description of the HF medium resides in the characterization of the random time variations which exhibit short-term characteristics superimposed upon 'long-term' characteristics. Short-term variations, which are a direct consequence of the dynamic behavior of the ionosphere, continuously affect the details of the received waveform, thus, influencing the system performance. On the other hand, variations of the long-term characteristics, which result in significant changes of the median values associated with the short-term characteristics of the different paths, occur at a rate that can range from several seconds to hours, and are often not observable during a typical transmission. For this reason, the long-term parameters are related to the availability of the channel; and are often taken as constant in the characterization of the communications medium.

2.4.1 Multipath Fading Channel

It is generally agreed that for a short period of time (less than 10 minutes) and a narrow bandwidth (less than 10 kHz), the HF medium may be described by its short-term statistics conditioned upon the instantaneous values of the long-term parameters [Stei87], [Masl87]. Following this approach, it is possible to model the short-term variations with quasi-wide sense stationary (QWSS) statistics as long as the channel correlation functions change sufficiently 'slowly' with changes in frequency and with changes in time [Bell63]. The concept of QWSS is appealing because it provides the means of representing the

1. Distinguishable means that the differential median delay between paths is sufficient to have them recognized as independent sequential returns.

medium as a WSS[1] channel, which is easier to deal with analytically. This concept is therefore exploited in the following characterization in conjunction with the fact that the different paths are considered as uncorrelated scatterers; i.e., the random behavior of energy dispersion in both time and frequency is independent from one path to another.

For a QWSS-Uncorrelated Scatterers (QWSS-US) channel, the multipath phenomenon may be described as the reception of a set of n distorted replicas of the transmitted signal with random delays and attenuation factors. If the baseband transmitted signal is expressed as $p(t)$, then the baseband representation of the received signal, $r(t)$, is the summation of all the detected returns:

$$r(t) = \sum_n \alpha_n(t)\, e^{-j\theta_n(t)}\, p(t-\tau_n(t)); \tag{2.7}$$

where $\alpha_n(t)$, $\tau_n(t)$, and $\theta_n(t) = 2\pi f_c \tau_n(t)$ are the random time-varying attenuation, the delay, and the phase associated with the nth path respectively.

Each path may be described with a random complex Gaussian process where fading may be described by its envelope and phase statistics. For the HF radio channel, it is widely accepted that the fading envelope is Rayleigh distributed and that the phase is uniformly distributed over the interval $[0, 2\pi[$ [CCIR82a].

Since the channel may be modeled as the sum of independent Gaussian processes, it is completely characterized by its scattering function $S(\tau;\nu)$ [Macc91], [Mala85], and [Papo84]:

$$S(\tau;\nu) = \int_{-\infty}^{\infty}\int_{-\infty}^{\infty} \varphi_c(\Delta t;\Delta f)\, e^{-j2\pi\nu\Delta t} e^{j2\pi\tau\Delta f}\, d\Delta t\, d\Delta f; \tag{2.8}$$

where $\varphi_c(\Delta t;\Delta f)$ is the channel auto-correlation function.

The scattering function of the received multipath signal may be regarded as a description of the signal's power density spread in both the time-delay and the Doppler-shift domains where the dispersion in time is referred to as the multipath spread, T_m, and the dispersion in Doppler shifts is termed as Doppler spread, B_D. These two parameters characterize well the short-term distortion of the HF channel [CCIR82a].

Figure 2.8 [Macc91] provides the relationships between the different Fourier transform pairs of the correlation functions when WSSUS statistics are assumed (F repre-

1. The statistics only depend on the time and frequency intervals Δt and Δf rather than the specific location of these intervals in terms of time, t, and frequency, f. Without loss of generality, the nominal propagation delay and frequency shift may be set to zero.

sents the Fourier transform and F^{-1} represents its inverse). The meaning of each of these functions is provided in the next sections.

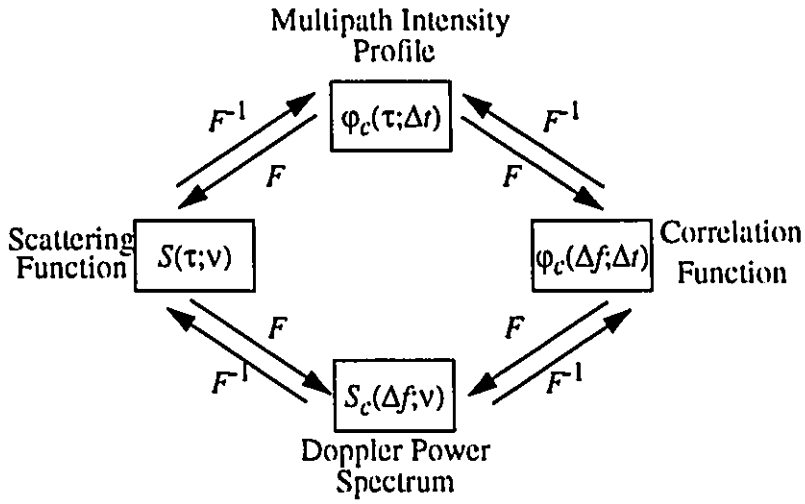

FIGURE 2.8. Relationships Between Correlation Functions

Multipath Spread

The range of delay over which the multipath intensity profile is not zero determines the multipath spread which may be related to the width of the received pulse when an impulse is transmitted. The Fourier transform of the multipath intensity profile with respect to 'τ' evaluated at $\Delta t = 0$ leads to the power spectrum of the channel as a function of frequency intervals Δf:

$$\varphi_c(\Delta f) = \int_{-\infty}^{\infty} \varphi_c(\tau)\, e^{-j2\pi\Delta f\tau} d\tau. \tag{2.9}$$

The range of frequencies over which (2.9) is not negligible is referred to as the coherence bandwidth, $(\Delta f)_c$. The coherence bandwidth may be described as the bandwidth over which the various frequency components of the signal are affected in a similar way. It is therefore a measure of the frequency 'selectivity' of the channel and is approximately related to the multipath spread T_m by:

$$(\Delta f)_c \approx \frac{1}{T_m}. \tag{2.10}$$

Doppler Spread

The Doppler spread, for its part, is defined as the range of Doppler shifts over which the Doppler Power spectrum is not zero when evaluated at $\Delta f = 0$. The time span

over which the inverse Fourier transform of the Doppler power spectrum with respect to Doppler shifts is not negligible determines the coherence time $(\Delta t)_c$:

$$\varphi_c(\Delta t) = \int_{-\infty}^{\infty} S(\nu) e^{j2\pi\Delta t\nu} d\nu \ . \tag{2.11}$$

The coherence time may be regarded as the time the channel takes for changing state and is usually related to the rapidity of fading or time selectivity. The coherence time is related to the Doppler spread B_D as follows:

$$(\Delta t)_c \approx \frac{1}{B_D} \ . \tag{2.12}$$

2.4.2 Type of Channels

Obviously, the influence of the propagation channel on a transmitted signal is a function of the relationship between the signal characteristics, in terms of its bandwidth and signalling interval, and the correlation properties of the channel in terms of the coherence bandwidth and the coherence time. Since the coherence parameters are related to the multipath spread T_m and Doppler spread B_D parameters, it is possible to estimate the signal characteristics required to avoid distortion in both the frequency and the time domains and to customize the channel model upon the type of distortion introduced.

For a system design where the signalling interval, T_b, is selected to be almost equal to the reciprocal of the signal bandwidth W; i.e.,

$$W \approx \frac{1}{T_b}, \tag{2.13}$$

a sufficient condition to avoid distortion in the frequency domain is to select a signal bandwidth that is much less than the coherence bandwidth; i.e.:

$$W << (\Delta f)_c. \tag{2.14}$$

In such a case the channel is referred to as a *frequency non-selective channel* and the frequency components of the signal are influenced in a similar manner across the signal bandwidth.

Similarly, a sufficient condition to ensure time coherence across the signalling interval is to choose W much greater than the inverse of the time coherence or much larger than the Doppler spread; i.e.:

$$W >> \frac{1}{(\Delta t)_c} \Leftrightarrow W >> B_D \ . \tag{2.15}$$

In this case, the signal is faced with a slowly fading channel; its attenuation and phase shifts are essentially fixed for the duration of one signalling interval.

The ideal case would be to avoid distortion in both time and frequency. This is only possible if the product of the multipath spread and Doppler spread, referred to as the spread factor SF, is much less than one; i.e.:

$$\mathrm{SF} = T_m B_D; \quad \mathrm{SF} \ll 1. \tag{2.16}$$

If condition (2.16) is met, which is usually the case for HF channels, and that the transmission rate, R_b, is selected to be nearly equal to the signal bandwidth, $R_b \approx W$, then it is possible to determine the minimum transmission rate, R_{min}, at which no distortion in both frequency and time can be achieved [Stei87]:

$$R_{min} = \frac{1}{2T_b}\sqrt{\frac{T_m}{B_D}}. \tag{2.17}$$

Using (2.17), it is possible to classify the type of channel by comparing the transmission rate with R_{min}:

- *Frequency and time non-selective channel.* This type of channel is also termed in the literature as flat-flat fading channel or frequency non-selective slow fading channel:

$$R_b \approx R_{min}. \tag{2.18}$$

- *Frequency selective and time non-selective channel.* The channel is also termed as frequency selective time-flat channel or frequency-selective slow fading channel:

$$R_b > R_{min}. \tag{2.19}$$

- *Frequency non-selective and time selective channel.* The channel is also termed as frequency flat-time selective channel or frequency non-selective fast fading channel:

$$R_b < R_{min}. \tag{2.20}$$

In general, the communications channel over the HF medium may be regarded as a frequency selective slow fading channel. However, during high solar activities, the medium may become sufficiently disturbed that fast fading occurs. In this last case, the channel is referred to as doubly dispersive; and distortion in both the time and the frequency domains are observed.

2.4.3 Typical Parameters for an HF Channel

Typical values for multipath spread T_m, Doppler shifts v, Doppler spread B_D and relative attenuations between signal returns depend on numerous factors including the path length used, the number of hops, the geographical location, the transmission duration, and, obviously, the ionospheric conditions. For instance, the E layer has usually a short path delay and a positive Doppler shift due to the downward motion of the layer, while the F layer has a longer path delay and a negative Doppler shift due to the upward motion of the layer. Other paths may involve ionospheric irregularities and will have significant multipath spreads, Doppler shifts, and Doppler spreads. Furthermore, Doppler spread tends to be more important at sunrise and sunset because of the significant changes in the ionospheric structures at these times of the day. Obviously, multiple-hop paths have higher attenuation than single-hop paths because of their longer path lengths [Gott91], [Mala81]. Table 2.1 provides typical ranges for the different parameters [Masl87], [CCIR90], [Proa89]. These figures are not absolute and values outside these ranges can be observed.

TABLE 2.1. Typical Values for the HF Channel Parameters

Condition	Multipath Spread T_m (msec)	Doppler Shift v (Hz)	Doppler Spread B_D (Hz)
Quiet	.001-1	.01-1	.01-.2
Disturbed	1-2	5-10	1-2
Auroral Belt	5-10	10-20	10-40

2.5 Channel Models

In order to compare performance of different communications systems under some specific channel conditions, it is required that the medium characteristics be similar for each of the systems under evaluation. This is not possible unless an independent real-time or on-the-air testing platform for each of the systems is used. This approach is, however, rather expensive and still leaves the communications engineers with a system evaluation that is restricted to some specific link conditions or that can only be repeated in a laboratory environment.

Three options are available to reduce testing costs while ensuring repeatability. The first alternative consists of deriving analytical solutions for determining system performance. Although this approach offers the advantage of obtaining performance without having to run long simulations, it is difficult to obtain, in the case of the wideband HF channel, a definitive statistical characterizations of the different channel parameters [Bello88].

The second alternative consists of recording the reception of a probe signal during a certain time interval and replaying it (or a processed version of it) at will to conduct the required tests. This approach, although inexpensive, limits the evaluation of the systems to the recorded set of atmospheric conditions. Moreover, since the channel variations are unpredictable, it is necessary to monitor the channel over a very long period of time in order to ensure that the recording includes most of the significant channel conditions.

The third alternative which is the one adopted in this thesis, is based on the analytical modeling of the statistical behavior of the medium and resides in the simulation of the channel. Naturally, the simulator characteristics must be as close to the reality as possible in order to produce meaningful results. The advantages of a simulator are well known and include: accuracy, regularity of performance, repeatability, availability, large range of channel conditions, reliability, and low cost [CCIR90].

[CCIR90] mentions a number of simulators that have been proposed over the years for modeling the HF medium. Even though most of these simulators have adopted different approaches, all of them deal with narrow bandwidth channels in which the random process may be considered as wide-sense stationary. Among them, the model proposed by Watterson [Watt70] has served as the basis for the Gaussian-scatter channel model described in [CCIR90]. This model has been widely used over the last 20 years [Ehrm82], [Daws84], [Lin90], and is described in the next sub-section.

Although the problem of modeling the HF channel under wideband conditions is not new, specific efforts in this area for deriving a representative model are recent and relatively few papers are available on the subject. A series of articles on the work performed at the US Institute for Telecommunication Sciences (ITS) has reported a promising approach to model wideband HF channel. The model is summarized hereafter [Mast91], [Hoff91], and [Vogl88b].

2.5.1 Gaussian-Scatter Channel Model

Because the HF medium is a time-variant dispersive channel, it may be modeled as a chain of filters with time-varying gains [Bello63]. Following this argument, Watterson proposed the model depicted in Figure 2.9. The model is based on two major assumptions about the channel characteristics which restrict its use to limited signal bandwidths [CCIR90]:

- the channel statistics are wide-sense stationary in both frequency and time; and

- the channel is composed of a discrete number of independent paths with no time dispersion; i.e., the median path delay is constant over the frequency band.

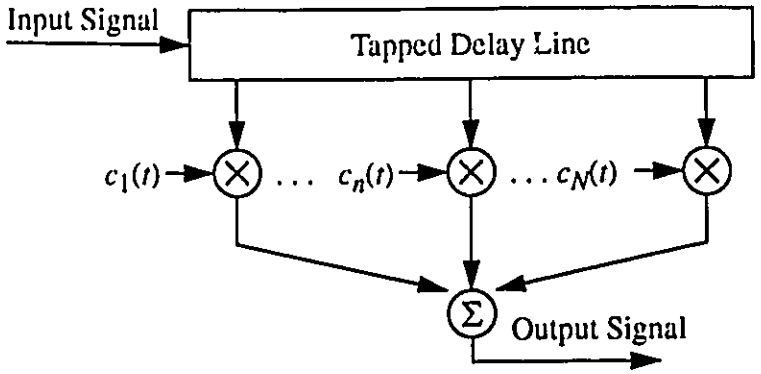

FIGURE 2.9. Gaussian-Scatter Channel Model.

The time-varying transfer function of the model may be expressed as:

$$H(f,t) = \sum_{n=1}^{N} c_n(t)\, e^{-j2\pi\tau_n f}; \tag{2.21}$$

where $c_n(t)$ is the time-varying tap gain function, and τ_n is the median delay, both associated with the nth propagation path.

The tap-gain functions, $c_n(t)$, introduce the short-term characteristics of the channel where the fading envelope voltage is Rayleigh distributed and the phase is uniformly distributed over the interval $[0, 2\pi[$. $c_n(t)$ may be expressed as:

$$c_n(t) = \tilde{c}_n(t)\, e^{j2\pi\nu_n t}; \tag{2.22}$$

where ν_n represents the Doppler shift associated with the nth path, and $\tilde{c}_n(t)$ is a sample function of an independent complex Gaussian process which has a Doppler spectrum described by:

$$C_n(f) = \frac{\alpha_n}{\sqrt{\frac{\pi}{2}(B_D)_n}} \exp\left[\frac{-(f-\nu_n)^2}{\frac{1}{2}(B_D)_n^2}\right]. \tag{2.23}$$

The spectrum is Gaussian shaped and the Doppler spread of each of the multipath components is determined by the bandwidth of their respective spectra.

2.5.2 Wideband Channel Models

The appropriateness of the Gaussian-scatter channel model is lost as the signal bandwidth is increased. Indeed, measurements which were originally conducted to validate this model showed that it stays representative of the HF medium over a maximum bandwidth of 12 kHz during day-time and of 2.5 kHz at night when ionospheric conditions are stable; i.e when the medium displays relative stationarity in both time and frequency [Watt70]. Over wider bandwidth, the median-delay dependence upon frequency becomes significant, particularly, at operating frequency close to the MUF; and the assumption regarding channel stationarity does not hold. This was verified by wideband measurements which effectively showed that the ionospheric channel is neither stationary in time nor in frequency over larger bandwidths [Lin90], [Belr88], and [Bell65].

The inadequacy of the Gaussian-scatter model and the growing interest in using HF over wide bandwidths has called upon the development of a few 'so-called' wideband HF models. Most of these models aim at including the frequency dependence on the median delay of each path. They vary in complexity depending on the goals they wish to achieve.

The simplest approach consists in keeping the basic elements of the narrowband model and in assuming a quadratic or higher order relationship between the median delay and the frequency [Bern91], [Mal85]. From (2.21), the transfer function can be expressed as:

$$H(f,t) = \sum_{n=1}^{N} c_n(t)\, e^{-j2\pi\tau_n(f)f}; \tag{2.24}$$

with:

$$\tau_n(f) = \tau_{n0} + \tau_{n1} f + \tau_{n2} f^2 + \ldots; \tag{2.25}$$

where $\tau_n(f)$ indicates the frequency-dependent median delay of the nth path.

Although this approach takes into consideration the variations of the median delay across the frequency band of interest, it still leaves aside the dependence of the time-varying tap gain function, $c_n(t)$, upon frequency. Furthermore, the difficulty in fitting (2.25) to measured ionogram data may become overwhelming if the ionospheric conditions are not stable as it might be expected for wideband channels.

Malaga [Mala81] proposed a generalization of the above approach by providing the means for determining the median value of the delay based on physical ionospheric parameters, and by describing the time-varying tap-gains as a function of frequency. His

approach is far superior than the previous ones since it accounts for the time variations of the median characteristics of the medium; but Malaga recognized that his model was aimed at modeling the mid-latitude HF channel where, usually, stable ionospheric conditions are observed.

Ionospheric Parameter Model

In 1988, Vogler and Hoffmeyer of ITS proposed a novel approach for modeling the HF channel [Vogl88a]. Their model does not assume WSS statistics and relates the propagation properties of the medium to its physical characteristics in terms of geographical location, season, and time while considering the delay dispersion associated with each return. In brief, the model provides an analytical expression relating the operating frequency and the median delays of each propagation mode. This approach can cover a variety of ionospheric conditions and provides a deterministic base around which statistical variations are added. The model is referred to as the Ionospheric Parameter Model and its main parts are shown in Figure 2.10.

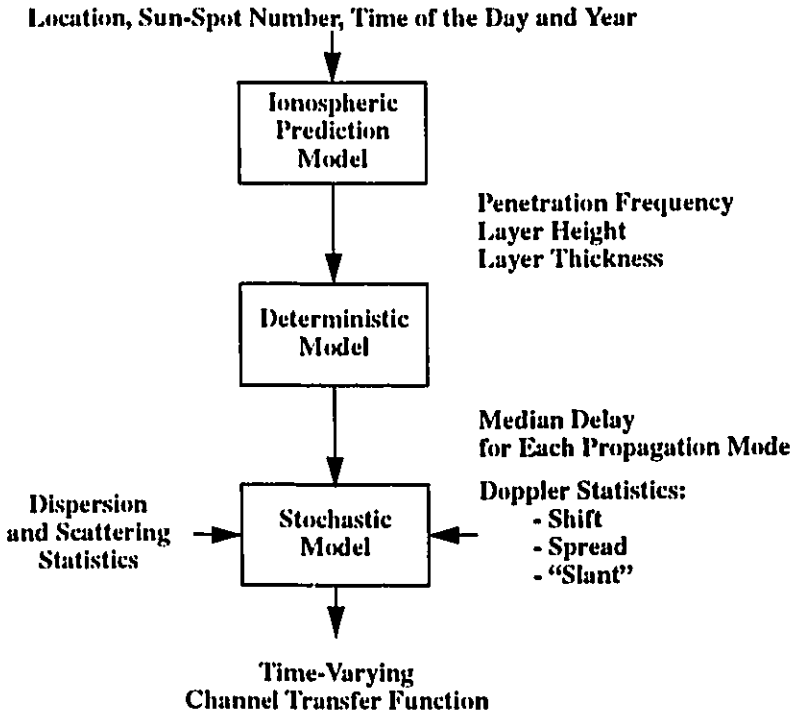

FIGURE 2.10. Ionospheric Parameter Model.

The first block of the model diagram serves to predict the physical characteristics of the communications medium with regard to time of the day and year, path geometry and latitude, and other propagation factors such as the sun-spot number. More specifically, three parameters are required by the model to represent the channel under a wide

variety of conditions, namely: the layer height of maximum ionization, h_o, the layer thickness, σ, and the penetration frequency, f_p.

The model chosen to predict these three physical parameters is a user-preference and may be any of the ones having been developed over the years. A detailed description of those different models is beyond the scope of the work presented in this thesis and the readers are referred to the report published by AGARD on this matter [AGAR90] or the paper by Rush [Rush86].

Deterministic Model

The second block of the diagram shown in Figure 2.10 is the deterministic model. The model [Vogl88a] is responsible for describing the variation of the median path delay as a function of the operating frequency and the three physical parameters provided by the ionospheric prediction model. The analytical expression derived by Vogler and Hoffmeyer is based upon the assumptions that there is no magnetic field, that the collision frequency is negligible[1], and that the electron density profile may be approximated by a hyperbolic secant squared (sech^2) function [Budd61] such that:

$$f_N^2 = f_p^2 \text{sech}^2\left[\frac{h_o - h}{2\sigma}\right]. \tag{2.26}$$

Keeping these assumptions in mind, the transfer function of one particular return at vertical incidence may be derived from the Maxwell's equation using the WKB solutions[2] [Budd61], [Davie65]. The end result may be expressed as:

$$H_n(f) \approx \left|H_n(f)\right| e^{-j2\pi\theta_n(f)}. \tag{2.27}$$

The first derivative of $\theta_n(f)$ with respect to frequency is associated with the median path delay, $\tau_n(f)$, and may be approximated by:

$$\tau_n(f) = \frac{\theta'_n(f)}{2\pi} = \frac{d\theta_n(f)}{2\pi df} \approx t_{o,n} - k_{o,n}\left[\ln\left(\frac{(f_p)_n}{f}\right) - 1\right]; \tag{2.28}$$

---

1. These two assumptions are not very restrictive for communications analysis purposes while allowing the use of a simplified expression for the refractive index η as given by (2.1). Indeed, most of the returns are from the E and F layers where the collision frequency is negligible. Moreover, the effect of the earth's magnetic field is to introduce magneto-ionic components which may be incorporated in the model as two separate returns if so is the need, and to cause additional fading due to polarization mismatches.

2. A complete derivation of the transfer function will not be provided here but may be found in [Budd61]. The use of the WKB solutions, which stand after Wentzel, Kramers, and Brillouin, those who first proposed them, is covered in most quantum mechanic books and the readers are referred to [Merz70] for a thorough description.

where:

$$t_{o,n} = \frac{2(h_o)_n}{c}; \text{ and} \tag{2.29}$$

$$k_{o,n} = \frac{2\sigma_n}{c}. \tag{2.30}$$

Rewriting (2.28) to define the virtual height of reflection[1] $\bar{h}_n(f)$ as:

$$\bar{h}_n(f) = \left(\frac{c}{2}\right)\frac{\theta'_n(f)}{2\pi} = (h_o)_n - \sigma_n \ln\left[\frac{(f_p)_n}{f} - 1\right], \tag{2.31}$$

it is possible to derive the relationship between the virtual height of reflection and f_v. The expression may be written as:

$$f_v = (f_p)_n \left\{1 + \exp\left[\frac{(h_o)_n - \bar{h}_n(f)}{\sigma_n}\right]\right\}^{-1/2}. \tag{2.32}$$

Equations 2.31 and 2.32 may now be used in conjunction with the theorems of Breit and Tuve, and Martyn (see Appendix B) to determine the median delay between two terminals separated by a distance D; i.e. for oblique incidence:

$$\tau_n(f) = \frac{\theta'_n(f)}{2\pi} = \frac{2\bar{h}_n(f)}{c}\sqrt{1 + \left(\frac{D}{2\bar{h}_n(f)}\right)^2}, \tag{2.33}$$

and the relationship between the carrier frequency and the virtual height of reflection:

$$f_c = (f_p)_n \sqrt{\frac{1 + (D/2\bar{h}_n(f))^2}{1 + \exp\left[\frac{((h_o)_n - \bar{h}_n(f))}{\sigma_n}\right]}}; \tag{2.34}$$

It can be noted that the last two equations, (2.33) and (2.34), reduce to (2.28) and (2.32) respectively in the case of vertical incidence; i.e. $D = 0$. Furthermore, it can be seen from (2.34) that for a specific carrier frequency, two solutions of $\bar{h}_n(f)$, and therefore $\tau_n(f)$, may be found: one for each of the high and the low rays.

---

1. The virtual height of reflection may be interpreted as the height at which the reflection would occur if the ionosphere behaved as a perfect reflector rather than as a superposition of refractive layers. The concept of virtual height is better explained in Appendix B.

Stochastic Model

The third block in the diagram shown in Figure 2.10 is the stochastic model [Vogl90]. The stochastic model is based on the use of the scattering function which relates the group delay and the Doppler frequency, for characterizing the time-varying ionospheric channel. The scattering function may be determined by the Fourier transform of the received signal auto-correlation function with respect to time. The expression may be written as:

$$S(\tau, \nu) = \int_{-\infty}^{\infty} \varphi_c(\tau, \nu; t)\, e^{-j2\pi ft}\, dt; \tag{2.35}$$

with the auto-correlation function $\varphi_c(\tau, \nu; t)$:

$$\varphi_c(\tau, \nu; t) \equiv T(\tau)\, C(t)\, e^{j\phi_s(\tau, \nu; t)}; \tag{2.36}$$

where τ and ν are respectively the median path delay and the Doppler shift at time t; and the functions $T(\tau)$, $C(t)$, and $\phi_s(\tau, \nu; t)$ are the delay amplitude factor, the correlation factor and the phase function respectively. Each one of these functions are discussed in more detail hereafter.

While the function $T(\tau)$ of the Gaussian-scatter model reduces to a set of Dirac functions evaluated at particular instances of τ; i.e. $\delta(\tau - \tau_n)$; $T(\tau)$ of the wideband model introduces the distortion of the transmission pulse caused by delay dispersion. The function may then be viewed as a shaping factor giving a measure of the multipath spread present in the received pulse. The expression proposed for this function is [Vogl90]:

$$T(\tau) = \sum_n \left[\alpha_n y^{\rho_n} e^{\beta_n (1 - y_n)}\, \delta(\tau - \tau_n) \right]; \tag{2.37}$$

where:

$$y_n = \frac{\tau - (\tau_L)_n}{\tau_n - (\tau_L)_n}; \tag{2.38}$$

and ρ_n, and β_n determined according to the following equation set:

For $0 \le y \le 1$, $((\tau_L)_n \le \tau \le \tau_n)$:

$$\rho_n = \frac{(1 - y_2) \ln |A_1| - (1 - y_1) \ln |A_2|}{d}; \tag{2.39}$$

$$\beta_n = \frac{(\ln[y_1]\ln[A_2]) - (\ln[y_2]\ln[A_1])}{d}; \tag{2.40}$$

where:

$$d = (1-y_2)\ln[y_1] - (1-y_1)\ln[y_2]; \tag{2.41}$$

$$A_2 = \exp\left[\frac{(1-y_2+\ln[y_2])\ln[A_1]}{(1-y_1+\ln[y_1])}\right]; \text{ and} \tag{2.42}$$

y_1, y_2, and A_1 being set to 0.01, 0.5, and to the receiver threshold A_{fl} respectively. These values were found to fit specific measured scatter functions more closely [Vogl90].

For $y > 1$, $(\tau > \tau_n)$:

$$\rho_n = \frac{(y_2-1)\ln[A_1] - (y_1-1)\ln[A_2]}{d}; \tag{2.43}$$

$$\beta_n = \frac{(\ln[y_2]\ln[A_1]) - (\ln[y_1]\ln[A_2])}{d}; \tag{2.44}$$

where:

$$d = (y_2-1)\ln[y_1] - (y_1-1)\ln[y_2]; \tag{2.45}$$

$$y_1 = \frac{y_2+1}{2}; \tag{2.46}$$

$$y_2 = \frac{T_n}{(T_\tau)_n}; \tag{2.47}$$

$$A_2 = \frac{A_{fl}}{A_n}; \text{ and} \tag{2.48}$$

A_1 being set to 0.5.

The variable $(\tau_L)_n$ indicates the smallest value of the median delay belonging to the nth return while T_n indicates the delay dispersion within the same return and $(T_\tau)_n$ is the time difference between τ_n and $(\tau_L)_n$. τ_n is determined by the deterministic model.

$C(t)$ is the correlation factor needed to model the fading effects caused by the Doppler phenomena. As mentioned in Section 2.4.1, it is widely agreed that the Doppler

spectrum displays a Gaussian shape[1] and this approach is adopted here also. $C(t)$ may then be expressed as:

$$C(t) = \sigma_f e^{-\pi(\sigma_f t)^2}; \tag{2.49}$$

with:

$$\sigma_f = \frac{B_D}{2}\sqrt{\frac{\pi}{\ln\left[\frac{A}{A_{fl}}\right]}}. \tag{2.50}$$

Finally, the term $\phi_s(\tau,\nu;t)$ in (2.36) introduces the variations of the frequency components as a result of the time variations of the physical parameters of the ionosphere. In the Ionospheric Parameter Model, these variations are assumed independent between each return and are approximated through a linear relationship between the group delay and the Doppler shift. The following expression is evaluated for each of the distinguishable returns:

$$\phi_s(\tau, \nu_n; t) = \phi_\tau + 2\pi\left[b(\tau_n - \tau)\right]t; \tag{2.51}$$

with:

$$b = \frac{(\nu_L)_n - \nu_n}{\tau_n - (\tau_L)_n}; \tag{2.52}$$

where $(\nu_L)_n$ is the frequency shift respective to the minimum median delay $(\tau_L)_n$, and ϕ_τ is the phase shift associated with a delay τ.

It is recognized that many forms of dependency other than a linear relationship between the frequency shift and the delay can be adopted. However, the added complexity does not appear to provide any additional information when the model is aimed at performance evaluations of communications systems [Vogl90].

1. Vogler and Hoffmeyer suggested that a 'peak' shape arising from variates having an exponential autocorrelation function might be more appropriate for describing the multipath fading over an HF channel. They supported their statement by showing the great similarity between simulations using this type of distribution and real measurements [Vogl90].

2.6 Noise and Interferences

In addition to time and frequency dispersion, communications signals transmitted over the HF medium are subjected to noise and interferences. The characteristics of ambient noise and interference signals are of major importance in communications system designs. Indeed, they are often the limiting factors which determine whether or not the received signal can be properly detected and used for gathering reliable information.

For the HF propagation medium, it is generally agreed that the noise comprises both narrowband and wideband components. The narrowband noise component is the resultant of a multitude of signals originating from many sources. Since all the sources are independent from each other, the narrowband noise component may be described via the central limit theorem as a zero-mean Gaussian distribution where its total average power is specified by its variance. On the other hand, the wideband noise components result from impulsive phenomena generally associated with atmospheric noise such as lightning discharges, or with man-made noise arising from motor ignition or power lines located at the proximity of the receiving antenna. Because atmospheric and man-made noise cause significant variations in the median characteristics of the narrowband noise, they must be considered as separate entities; thus, resulting in an overall ambient noise which cannot be described as additive white Gaussian noise (AWGN) [Orei82].

Interferences within the HF spectrum are usually narrowband signals originating from legitimate transmitting radio stations. Their effects on the system performance depend upon their relative power and similarity with the transmitted signal. They are usually accounted as separate processes in the description of the transmission channel and in the calculation of the system signal-to-noise ratio.

2.6.1 Wideband Noise Model

The wider the channel bandwidth, the higher will be the probability of running across intervals of bursty noise, and of being subjected to interferences. For this reason, the noise cannot be white across the transmission bandwidth [Gott91], [Masl87]; it comprises other components such as interference and impulsive noise. The overall noise, $N(t)$, is usually expressed as:

$$N(t) = G(t) + I(t) + J(t) \tag{2.53}$$

where $G(t)$, $I(t)$, and $J(t)$ represent the average amplitudes of the white Gaussian components, the impulsive noise components and the interferences respectively.

Several studies have been conducted over the years for describing each one of the terms of (2.53) independently. However, very few models have been proposed to characterize the wideband process as a whole; and the difficulty of statistically characterizing

the amplitude and the occurrence rate of the last two terms is still an area of research [Vogl88b]. A model developed in parallel with the IPM model was published in a series of paper [Lemm90], [Vogl88b]; and is described hereafter.

Lemmon developed a model based on both the approach proposed by Middleton for jointly describing narrowband and wideband noise, and on an approach proposed by Hall for modeling atmospheric noise [Lemm90]. The model may be summarized as follows:

$$N(t) = G(t) + \sum_{i=1}^{N_i} \left\{ b_i \frac{\sin[2\pi W(t-t_i)]}{(t-t_i)} \sin(2\pi f_c t_i) \right\} + \sum_{j=1}^{N_j} \{ a_j \cos(2\pi \Delta f_j t + \Delta\phi_j) \} \tag{2.54}$$

where $N(t)$ represents the amplitude of the complex noise with independent and identically distributed imaginary and real components.

The first term of (2.54), $G(t)$, represents the white Gaussian noise components where the average power level is determined by the variance of the distribution, the second term, $I(t)$, represents the impulsive noise components where N_i is the number of impulses at time t, b_i is the amplitude of the ith impulse, W is the bandwidth of the received filtered signal, and t_i is the arrival time of the ith impulse. It is further assumed that the time of arrival of a specific impulse t_i is uniformly distributed over the transmission interval, and that the amplitude, b_i, of each impulse is distributed according to the probability density function proposed by Hall:

$$f_B(b) = \frac{b(\theta_b - 1)\gamma_b^{(\theta_b - 1)}}{(b^2 + \gamma_b^2)^{(\theta_b + 1)/2}}; \tag{2.55}$$

where θ_b and γ_b are numerical parameters set to fit particular impulse characteristics.

The third term of (2.54), $J(t)$, deals with the interference signals. Lemmon assumes that their amplitudes are distributed in the frequency domain in the same manner as the impulsive noise components are distributed in the time domain. Thus; the amplitude a_j are distributed according to (2.56) which is repeated hereafter with the appropriate variables:

$$f_A(a) = \frac{a(\theta_a - 1)\gamma_a^{(\theta_a - 1)}}{(a^2 + \gamma_a^2)^{(\theta_a + 1)/2}}. \qquad (2.56)$$

It must be noted that the values of θ_a and γ_a are different from θ_b and γ_b. Furthermore, it is assumed that Δf_j, the frequency difference between the carrier frequency of the jth interference and f_c, and $\Delta\phi_j$, the phase difference between the jth interference and the legitimate signal, are uniformly distributed over the signal bandwidth W and over the interval $[0, 2\pi[$ respectively.

2.7 Conclusion

In this chapter, the medium is described as a time-varying dispersive multipath channel where its characteristics, which depends upon the physical structure of the ionosphere, evolve in a random manner. While the channel may be modeled by wide sense stationary statistics for the narrowband case, it is emphasized that the delay dispersion introduced by the delay-frequency dependence cannot be neglected over wider bandwidths. The Ionospheric Parameter Model, which relates the wideband channel transfer function with the physical characteristics of the medium is then described. Finally, the problem of characterizing wideband noise is addressed and a model for describing the whole process is summarized.

From this study, the communications systems must use different techniques to mitigate the effects of the propagation medium if acceptable performance are to be achieved. In the next chapter, a number of these impairment mitigation techniques are addressed. Emphasis, is given on the utilization of frequency diversity, and more particularly on direct sequence spread spectrum for minimizing the perturbing effects of multipath and delay dispersion.

Chapter 3
Mitigation Techniques for Wideband HF Channels

3.1 Introduction

Over the last few years, the trend toward faster and more reliable HF communication links has fostered the development of techniques to maximize the utilization of the limited 3 kHz allocated channel bandwidth. While major improvements have been achieved, particularly in the field of adaptive channel equalization, it has been shown that larger bandwidths could offer an attractive alternative to improve modem performance without increasing significantly the modem complexity.

In addition to allowing higher data transmission rate, wideband signalling offers the possibility of implementing spread spectrum techniques. These techniques which possess the attendant features of interference rejections, provide the means for mitigating the effects of fading caused by multipath components. Moreover, it permits to exploit the inherent diversity of the skywave channel through the use of a RAKE receiver.

The present chapter concentrates on providing fundamentals on spread spectrum techniques and more particularly on Direct-Sequence Spread Spectrum. Multipath diversity benefits are covered through the description of the RAKE receiver. The chapter includes a brief overview of error control coding and interleaving techniques as a means for introducing time diversity.

3.2 Background

The HF channel multipath structure described in Chapter 2 has so far been regarded as a nuisance which results in severe multipath fading and inter-symbol interference. For years, system designers were left with low performance standard to avoid situations in which system performance would degrade too much. Among these, the one which consists of lowering the transmission rate to a level smaller than the coherence frequency of the channel has greatly promoted the belief that the skywave medium could only support low data transmission rates; i.e., 75 bps or less.

In the 60's, major projects were initiated to acquire a better knowledge of the physical structure of the ionosphere. The results of these large endeavors permit the development of a series of channel prediction models [AGAR90]. These models forecast

the physical properties of the ionosphere with relative good accuracy and provide the means for determining the optimum operating frequency of a particular link. Based on this data, HF operators are now able to optimize their system performance and can achieve data transmission rates in the order of 300 to 600 bps with acceptable efficiency [Bray87]. Based on the same idea, 'frequency-agile' serial modems were thereafter developed. These modems make use of a probe signal transmitted at different frequencies to scan the channel. The optimum operating frequency is determined by choosing the frequency of the received probe signal having the best signal-to-noise ratio characteristic. The performance of these modems is dependent upon the number of time the channel is sounded in order to change the frequency if necessary and the number of frequencies available to choose from.

Besides the difficulty related to spectrum management and to synchronization of 'frequency-agile' modems, the need for higher data rates has brought researchers to look for alternatives to the serial modems architecture. The result was the development of the parallel-tone modem [Stei87]. Parallel-tone modems can achieve transmission at 2400 bps by dividing the allocated 3 kHz bandwidth to a number of sub-channels over which sufficiently low transmission rates are used to minimize ISI; i.e. approximately 100 bps or less. Although parallel-tone modems presented a more complicated architecture then the one for serial modems, their performance was unequal until the advent of serial modems equipped with efficient adaptive channel equalizers.

Adaptive equalization techniques enriched with error correction coding have brought serial modems to operate at rates of 2400 bps and higher. It can therefore be expected that the current standard of 2400 bps for state-of-the-art commercial modems will soon be increased. Based on this, two major trends have emerged in the literature. While the first one consists of developing more efficient channel equalization algorithms [Clar89], the second concentrates on the use of wider bandwidth [Perr82] [Dahr82] [Vogl88b].

Even though wide bandwidth channels suffer from aggravated ISI problems due to intra-modal delay dispersion and of lower signal to noise and interference ratio (SNIR) due to an increased number of interferences, Perry [Perr83] showed that under stable ionospheric conditions, adaptive equalization was possible over a 1 MHz bandwidth. In his treatment, he restricted the channel to one mode, single-hop link, but successfully demonstrated the capability of the HF channel to support wideband signalling under real conditions. His work has encouraged several researchers to develop and implement wideband mitigation techniques, including spread-spectrum, [Chow82], [Ochs87], and multipath diversity, [Wagn89], [Bell88], [Gong90], and [Kane90], as originally proposed by Price and Green in 1958 [Pric58].

3.3 Spread Spectrum

In an interference environment such as the HF skywave medium, the optimal approach for a communication system is to ensure that the detrimental effects of the interfering signals are not worse than those caused by Gaussian noise at equivalent SNR. The system should therefore transmit a signal waveform that is as wideband as possible and be capable of processing interference signals to affect the system performance as does Gaussian noise [Vite91]. Spectrum spreading is one possible approach to transmit information over wide bandwidths. In spread spectrum system, the transmitted signal is characterized by its bandwidth W_{ss} which is much larger than the information rate R_b and by its pseudo-randomness that makes the signal appears similar to noise. Pseudo-randomness is particularly important because it is the key element behind most of the applications for such signals. Among them, the most interesting for HF systems are:

- Interference rejection;
- Multiple access;
- Multipath protection; and
- Time of arrival measurement.

It must be noted that multiple access and multipath protection are intimately related to interference rejection since all three have signal components not intended to the receiver. More specifically, users of multiple access systems share the same portion of the spectrum and see one another as interference while multipath returns may be interpreted as self-interference. On the other hand, time of arrival measurement also termed ranging, applies to radar and sounding applications. It is based on the fact that maximum correlation output is obtained when the received and spreading signals are perfectly synchronized. Thus, the traveling time of the transmitted signal may be obtained by evaluating the time shift required to maximize the correlation level with the received (reflected) signal; and thereby determining the range between the terminal and the point of reflection.

Among the different spread spectrum techniques investigated over the years, two are commonly used in digital communications systems: direct sequence spread spectrum (DSSS) and frequency hopping (FH). In the case of frequency hopping, which is primarily used in anti-jam protection and for CDMA applications, the available spreading bandwidth W_{ss} is subdivided into a large number of contiguous frequency slots approximately $1/R_b$ wide. In any signalling interval, the transmitted signal occupies one or more of the frequency slots made available in a pseudo-random manner [Proa89]. Because proper phase coherence is difficult to maintain while the signal is hopped from one frequency to another, non-coherent FSK is usually employed, leading to poorer performances than those achievable by direct sequence spread spectrum systems [Vite76].

3.3.1 Direct Sequence Spread Spectrum

Frequency hopping is based on the principle of avoiding or minimizing the time spent in portions of the spectrum where poor performances are obtained whereas direct sequence spread spectrum is based on the discrimination and suppression of all signals not intended to the receiver. Discrimination between the intended signals and the interference components is possible by "impressing" a pseudo-random sequence to the information stream before transmitting it. The effect of impressing the pseudo-random sequence is to spread the bandwidth of the original signal by a factor defined as the processing gain PG, and to reduce the level of the power spectrum density by the same factor. The processing gain may be expressed as:

$$\mathrm{PG} = \frac{W_{ss}}{R_b} = \frac{T_b}{T_c}; \quad T_b >> T_c; \tag{3.1}$$

where W_{ss} is the spreading bandwidth and its reciprocal[1] T_c is the duration of one pulse or one *chip* of the spreading sequence. Attenuation or suppression of unwanted components is occurring for any component that is one chip or more out of phase with the spreading sequence while at the same time the desired one is despread.

Direct Sequence Spread Spectrum Transmitter

Direct sequence spread spectrum signals are formed by impressing on the signal to be transmitted a sequence having a rate much higher than that of the source. Thus, the information data stream may be considered as being modulated twice before being transmitted, first by the transmitter carrier and next by the spreading sequence. The transmitted signal $s(t)$ may be expressed as:

$$s(t) = Ac(t)\,p(t)\cos(2\pi f_c t + \theta); \tag{3.2}$$

where $p(t)$ and $c(t)$ are the baseband data signal and the spreading sequence signal respectively, and A is the product of the amplitudes of both $c(t)$ and $p(t)$.

In the case where binary PSK modulation is used and where it is assumed that the spreading sequence signal has the same waveform as the baseband data signal[2], $p(t)$ and $c(t)$ may be expressed as:

$$p(t) = \sum_k b_k u_b(t - kT_b), \text{ and} \tag{3.3}$$

1. As in Chapter 2, the chip rate R_c is assumed equal to the bandwidth W_{ss} occupied by the spread signal.
2. Although not necessary, the spreading signal has usually the same form as the data signal [Ziem85].

$$c(t) = \sum_i c_i u_c(t - iT_c); \tag{3.4}$$

where $b_k = A_b e^{j\phi_k}$, $\phi_k = 0$ or π; $c_i = A_c e^{j\phi_i}$, $\phi_i = 0$ or π; and $u_b(t)$ and $u_c(t)$ are square wave signals of period $1/R_b = T_b$ and $1/R_c = T_c$ respectively.

Equation 3.2 implies that the signal resulting from the product $c(t)p(t)$ will change in phase at a rate equal to the rate of the spreading sequence signal; i.e. the phase will change 'PG' times over one bit period T_b. This concept may be better visualized if the signal is spread at baseband rather than being spread after the signal is modulated by the carrier frequency.

Spreading the signal at baseband can easily be done by altering the value of the information bits by performing a modulo-2 addition with the chips produced by the spreading sequence generator at a rate R_c ($R_c >> R_b$). Hence, the resulting signal will have a phase equal to zero every time the information and the spreading sequence bits are the same and a phase of π every time they are different. A block diagram of the transmitter implementing this approach is shown in Figure 3.1.

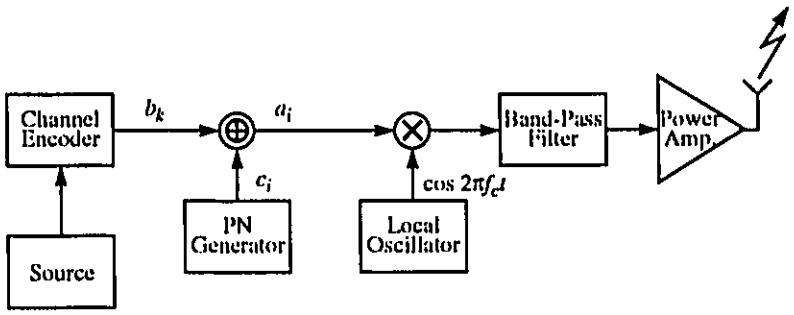

FIGURE 3.1. DSSS BPSK Transmitter

If c_i in Figure 3.1 represents the ith chip of the spreading sequence and b_k is the corresponding coded bit then the baseband spread signal may be expressed as:

$$v(t) = \sum_i a_i u(t - iT_c); \tag{3.5}$$

where $a_i = b_k \oplus c_i$; $k << i$, and $\oplus$ indicates modulo-2 addition.

The changes incurred by the information data stream as a result of the modulo-2 addition with the spreading sequence are shown in Figure 3.2. The signal in (c) is the modulo-2 sum of the signals in (a) and (b). It can be observed that the spread signal will become nearly independent from the original information data stream as the number of

chips (usually an integer number) per bit increases [Ziem85]. Indeed, the spread signal will inherit its spectral characteristics.

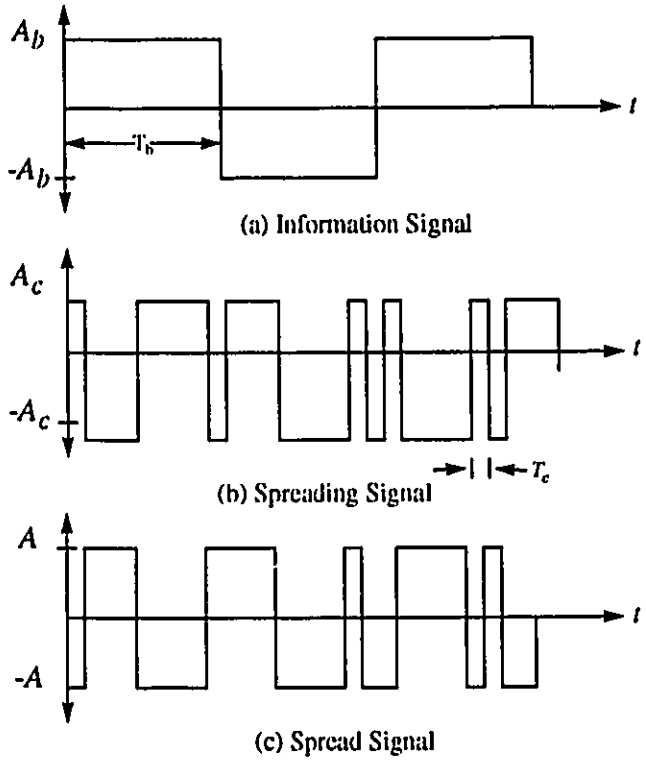

FIGURE 3.2. DS Spread Spectrum Signals

The resulting changes in the signal power spectrum caused by impressing the spreading sequence may be observed in Figure 3.3. $S_b(f)$ represents the power spectrum of the signal without spreading, $S_c(f)$ is the power spectrum of the spread signal, and A is the amplitude which results from the product A_bA_c. Attenuation of the spread signal by a factor T_b/T_c and expansion of its bandwidth by the same factor can be clearly observed in the figure.

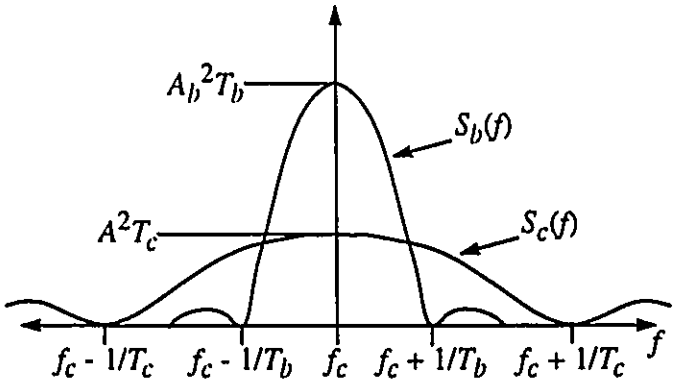

FIGURE 3.3. Power Spectrum Comparison Between Spread and Non-Spread Signals

3.3.2 Pseudo-Noise Sequence

To achieve its goals, DSSS signals must exhibit spectral and probability characteristics that are close to those of random Gaussian noise. Since these characteristics result from the specificities of the spreading sequence, it is required that the sequence displays Gaussian spectral characteristics. Unfortunately, this requirement can only be fulfilled through the use of an infinite-length random sequence. Obviously such sequence cannot be implemented since it would require an infinite amount of memory for storing it at the receiver. The sequence must therefore be deterministic in order to be reproducible at the receiver. For this reason, it is usual to generate finite-length pseudo-random sequences referred to as Pseudo-Noise (PN) sequences.

By far the most widely used binary PN sequences for spread spectrum applications are maximum length sequences. Such sequences may be generated by a linear feedback shift registers similar to the one shown in Figure 3.4.

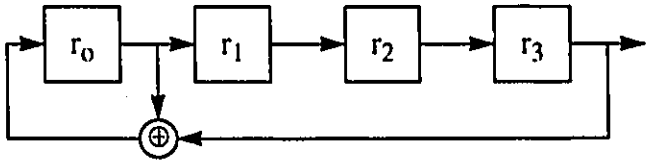

FIGURE 3.4. Example of a 4-Stage Linear Feedback Shift Register

Maximum length sequences also referred to as *m*-sequences are based on primitive polynomials in the Galois field of interest ($GF(2^4)$ in Figure 3.4). Tables of such primitive polynomials may be found in several references (e.g. [Lin83]).

The degree *m* of the primitive polynomial determines the number of shift registers required to generate a PN sequence of cyclic period *N*.

$$N = 2^m - 1, \tag{3.6}$$

The period given by (3.6) is critical because it defines the discrimination capability of the spread signal. Discrimination increases with the length *N* of the sequence and it is usual to choose a sequence having the longest cyclic period possible.

In addition to its cyclic period characteristic, *m*-sequences have some other property that is particularly useful for spread spectrum applications [Ziem85]: their auto-correlation function is similar to that of an infinite sequence and is responsible for the gain obtained in DSSS systems. Rather than consisting of a single triangle pulse of width $2/T_c$ as does the auto-correlation function of an infinite-length binary sequence, the normalized auto-correlation function $\varphi_{PN}(\tau)$ of a PN sequence may be written as:

$$\varphi_{PN}(\tau) = \begin{cases} 1 - \dfrac{\tau}{T_c}\left(1 + \dfrac{1}{N}\right), & 0 \le \tau \le T_c; \\ \dfrac{-1}{N}, & T_c < \tau < (N-1)\,T_c; \\ \dfrac{\tau_\varepsilon}{T_c}\left(1 + \dfrac{1}{N}\right) - \dfrac{1}{N}, & (N-1) \le \tau < (n-1)\,T_c; \end{cases} \tag{3.7}$$

where $\tau_\varepsilon = \tau - (N-1)\,T_c$.

The function $\varphi_{PN}(\tau)$ is shown in Figure 3.5. It can be seen that $\varphi_{PN}(\tau)$ resembles to the ideal infinite-length sequence as N is increased.

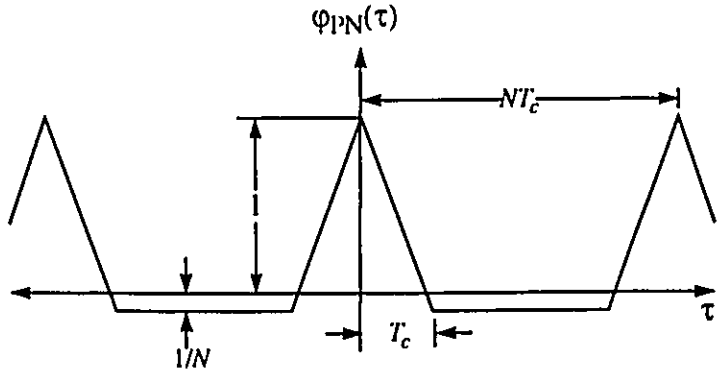

FIGURE 3.5. *m*-Sequence Auto-correlation Function

3.4 Reception of DSSS Signals

As for narrow band signalling, optimum performances are obtained when the receiver is matched to the received waveform. If problems introduced by synchronization mismatches are neglected[1], the optimum DSSS receiver for a single-path channel is as shown in Figure 3.6 [Proa89].

Despreading is accomplished by correlating the received signal with a locally generated PN sequence identical to the one used at the transmitter. When the two signals are matched, the desired signal collapses to its original bandwidth, whereas any unmatched components is spread by the local PN sequence over a bandwidth W_{ss}. The power spectrum is modified as shown in Figure 3.7 where (a) and (b) illustrate the received signal components before and after despreading respectively

1. Since synchronization must be maintained within $1/T_c$ second; synchronization problems may quickly become overwhelming as the processing gain is increased.

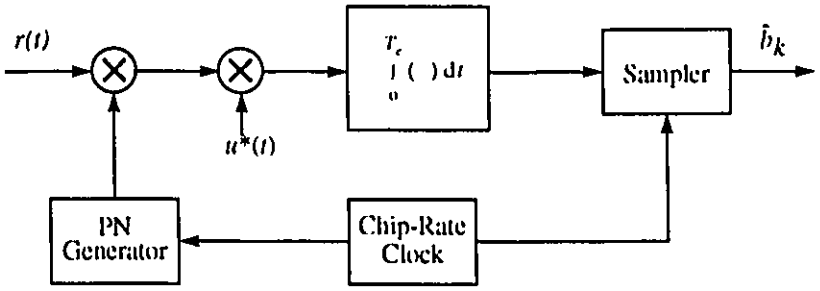

FIGURE 3.6. Spread Spectrum Correlator Receiver

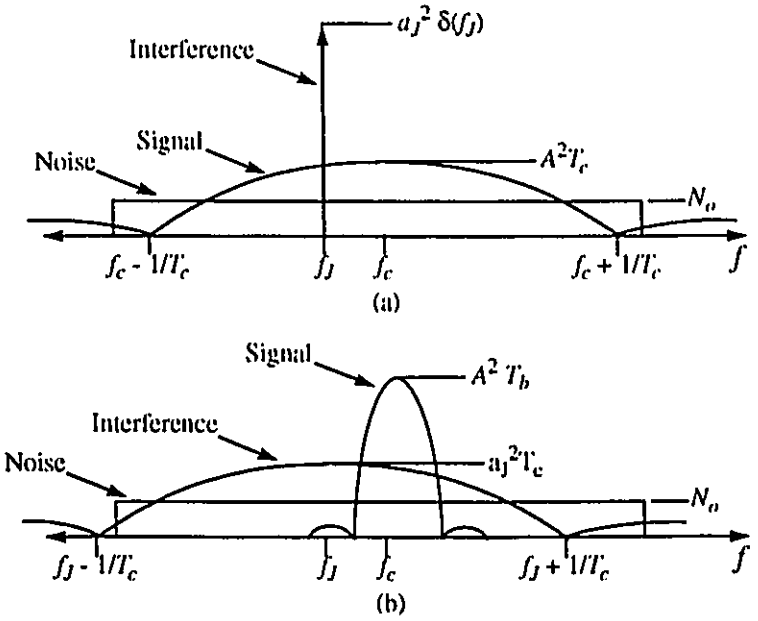

FIGURE 3.7. DS Spread Spectrum - Interference Rejection

In the case of a multipath composite signal where each signal component is despread with the same PN sequence, the DSSS ability to discriminate between each one of them is a function of the chip period T_c. Indeed, any component that is separated in time by more than one chip period will be distinguished from one another. Because discrimination is based on correlation with the local reference PN sequence, no gain should be expected in the case of a pure AWGN channel or in the case of frequency non-selective fading channel where the received signal is altered similarly across all the occupied bandwidth.

The performance of a DSSS correlator receiver in presence of interference depends on the modulation type used and the SNIR. For instances, in the case of a single-tone interference, the SNIR per bit γ_{Jb} may be expressed as [Ziem85]:

$$\gamma_{Jb} = \frac{2E_b}{N_o + E_{Jc}\mathrm{sinc}^2(f_c - f_J)}; \tag{3.8}$$

or in the case of a partial-band interference, having white Gaussian characteristics [Ziem85]:

$$\gamma_{Jb} \approx \frac{2E_b}{N_o + 0.903J_o}. \tag{3.9}$$

In both equations, variables are defined as follows:

- E_b is the energy per bit of the transmitted signal,
- E_{Jc} is the energy per chip of the interference tone,
- f_J is the interference tone frequency, and
- J_o is the interference energy density over a chip duration.

From the above two equations, it can be seen that the performance is increased by the fact that the interference energy is fractionated over the spreading bandwidth W_{ss}, rather than being concentrated in the signal bandwidth W. In other words, only a fraction of the interference energy contributes to reduce the SNIR.

3.5 Diversity Systems

The receiver structure presented in Figure 3.6 is optimum for single path time invariant channel. In the case of time varying multipath HF channel, the receiver must cope with rapid fading and ISI conditions. While the effects of the latter is usually mitigated by the use of adaptive equalization techniques, rapid fading caused by multipath returns is best handled by diversity techniques.

Diversity stands on the observation that if the same information is received redundantly over two or more independently fading channels, there is a much lower probability that all the received replicas corresponding to the same transmitted symbol or bit be simultaneously affected by a deep fade condition. In other words, if L replicas of the same signal is transmitted over L different paths and if p is the probability that a deep fade occurs; then p^L is the probability that all replicas fade simultaneously. With adequate combining of the different diversity paths at the receiver, the error performance becomes a function of the average SNR of the received signal in each of the paths. In the case where the average SNR per bit $\overline{\gamma_b}$ is assumed identical for all the paths, the expected probability of error for DPSK modulation is given by [Proak89] as:

$$P_b = \left(\frac{1-\mu}{2}\right)^L \sum_{k=0}^{L-1} \binom{L-1+k}{k} \left(\frac{1+\mu}{2}\right)^k ; \tag{3.10}$$

where:

$$\mu = \frac{\bar{\gamma}_b}{1+\bar{\gamma}_b}. \tag{3.11}$$

Equation 3.10 is used to compare the performance obtained from a simple AWGN channel with the one obtained from a Rayleigh slowly fading channel for different levels of diversity. The advantage of using diversity over fading channels can be appreciated in Figure 3.8 even for moderate levels of diversity.

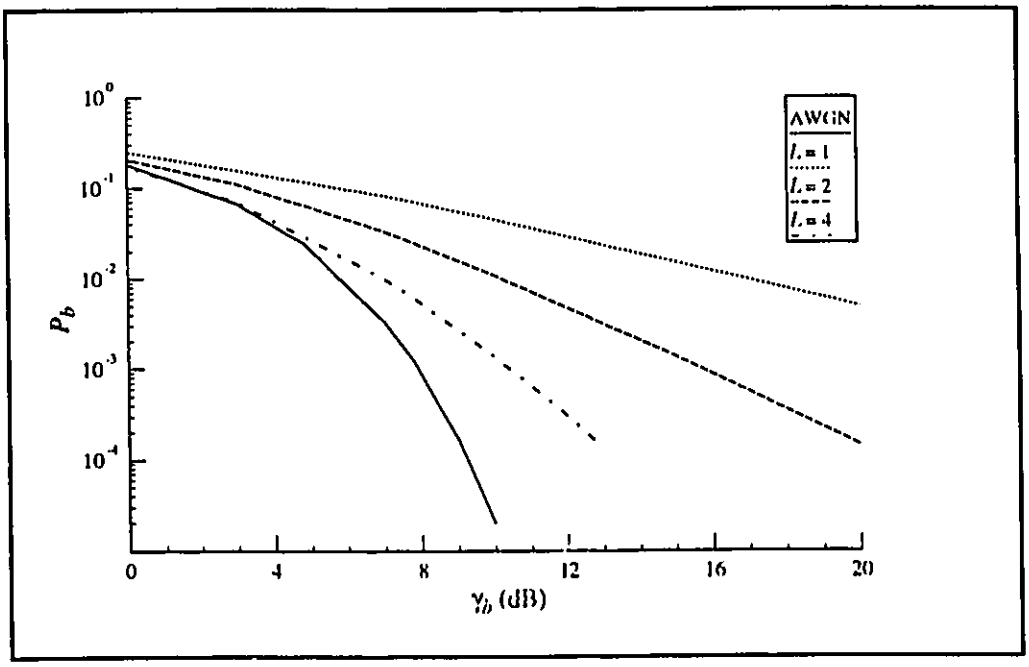

FIGURE 3.8. Theoretical Bit Error Probability for a DPSK Receiver With Different Levels of Diversity in Rayleigh Fading Channels

Among the several methods of diversity that have been proposed over the years, time and multipath diversity techniques are investigated in this work. Time diversity is based on the principle that if the same information datum is redundantly transmitted at time intervals that exceed the coherence time $(\Delta t)_c$ of the channel, the redundant data will be received with independent fading conditions. Time diversity can be implemented with error control coding and bit (or symbol) interleaving. Multipath diversity arises when different parts of the frequency band fade independently. If the bandwidth used for transmitting the signal is much greater than the coherence frequency $(\Delta f)_c$ of the channel, then one portion of the band may be in a deep fade while another can provide reliable communications.

3.5.1 Multipath Diversity

As opposed to time diversity where the level of diversity can be increased almost indefinitely, the level of multipath diversity is rather implicit and is limited by the channel. As a rule of thumb, the level of diversity L that can be achieved over a dispersive channel is usually approximated by the ratio of the signal bandwidth to the coherence frequency of the channel [Proak89]; i.e:

$$L \approx \frac{W}{(\Delta f)_c}. \tag{3.12}$$

To increase the level of diversity, it is therefore necessary to use a signalling bandwidth as wide as possible and to design a receiver structure able to recover the transmitted energy present in all of the diversity paths available.

3.5.2 RAKE Receiver

In a frequency-selective environment like the HF medium, a standard spread spectrum one-path correlator receiver demodulates the signal received from the main path and suppresses the signal components received from the other paths. A better receiver makes use of the inherent diversity of the skywave channel by using a number of taps synchronized with each return [Ochs87]. The well-known RAKE receiver in its form of a multipath diversity combiner seems to be the optimum implementation in such a case. Since the achievable performance increases with the level of diversity, the ideal case is when the number of taps equals the number of diversity paths. However, in most applications it is necessary to restrict this number to the processing capability available.

Numerous RAKE receiver architectures have been suggested in the literature [Wagn89]. However, the most common design employs coherent detection with maximal gain ratio combining or differential detection with equal gain combining. Clearly the use of coherent detection with maximal gain ratio combining would provide the best results if channel conditions could be estimated perfectly. However, differential detection, despite its poorer performance, may appear more convenient because it does not require complex synchronization device [Turi81]. Differential PSK (DPSK) is therefore adopted in the remaining of this work.

The block diagram of a baseband DPSK RAKE receiver is illustrated in Figure 3.9. The structure of the L-tap delay line is made of one-chip delay element embedded between each tap. The multipath components that are delayed by more than one chip duration will be processed by different taps. Elimination of 'noise-only' taps may be performed by examining the average power of each tap output and rejecting those that are not likely to contain the desired signal. The L delayed signal components are correlated with

the local PN sequence. The correlation involves multiplication of the locally generated complex conjugate modulated chips with the received chips. Correlation is followed by successive integrate and dump (I&D) operations over one bit duration. In the case of DPSK, the tap weights are simply the conjugate of the previous I&D outputs and the input to the decision device is the algebraic summation of all tap outputs.

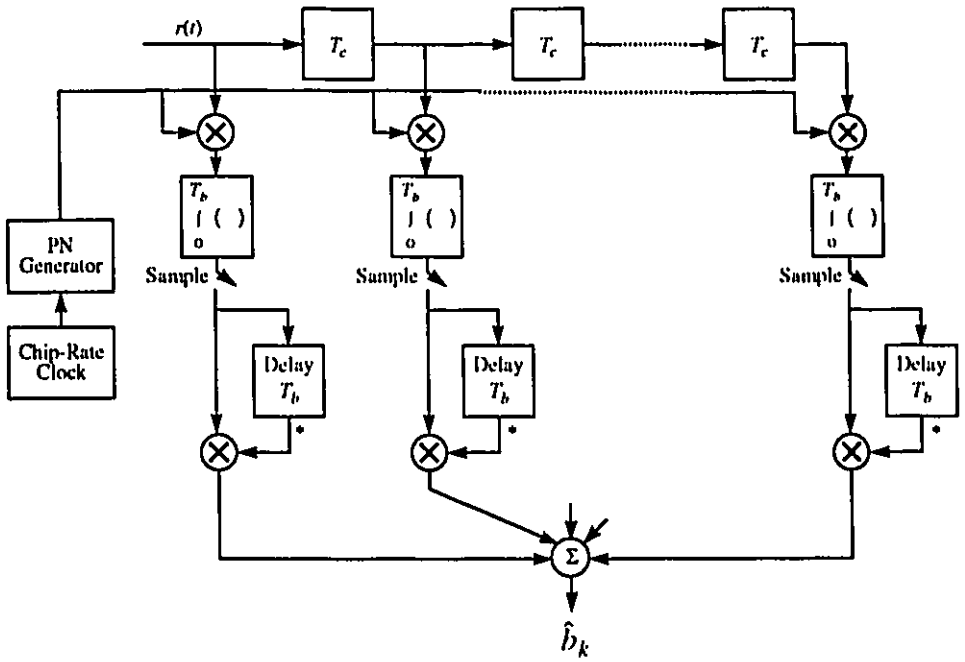

FIGURE 3.9. Baseband DPSK Rake Receiver

3.6 Error Control Coding

As mentioned previously, time diversity implies that the redundant information is transmitted over independent fading period. Time diversity can be implemented as a repetition code where the level of diversity depends on the codeword length. Thus, performance is expected to improve as longer codes are used. Repetition codes are however a trivial form of coding with low code rates and one is expected to employ more efficient error control coding schemes.

While, the primarily goal of error control coding is to insert redundant information into the bit stream for the purpose of detecting and/or correcting transmission errors at the receiver, Proakis showed that systems employing error control codes can benefit, as those employing repetition codes, of time diversity [Proa89]. Both block and convolutional codes are presented hereafter.

3.6.1 Block Codes

In block coding, the information bit stream is partitioned into blocks of k bits. Each k-bit information block is encoded with an n-bit codeword ($n > k$). Thus, every n transmitted bits contain only k bits of information so that the rate of the code is 'k/n'. As a result of transmission errors, the n received bits can be any of the 2^n possible n-bit vectors. Since there are only 2^k possible codewords that could have been transmitted ($2^k < 2^n$), the decoder can decide what was the most likely codeword that was originally transmitted and thereby identify the k information bits.

The ability of a decoder to identify properly the k information bits from a corrupted set of n bits depends on the error-correction capability of the code. Since the error-correction capability is related to the minimum distance property of the code, maximum codes such as the well-known Reed-Solomon (RS) code are particularly popular. RS codes are a subclass of non-binary BCH (Bose-Chaudhuri-Hocquenghem) codes with symbols defined from the Galois field GF(q); q being any integer. An RS code with an error-correction capability of t is characterized as follows:

- Codeword length: $n = q - 1$;
- Number of parity-check digits: $n - k = 2t$; and
- Minimum distance: $\mathbf{d_{min}} = 2t + 1$.

If we restrict the discussion to RS codes having code symbols taken from GF(2^M), M being the number of information bits per symbols to be encoded, it can be said that RS codes are particularly convenient for M-ary modulation. In the case of binary modulation, they present an efficient structure to correct the error bursts that are typical over time-variant fading channel such as the HF medium. In addition, RS codes offer the advantage of generating long codewords that are well suited for applications where a high level of time diversity is required.

Encoding

The encoding of a block code is based on a generator polynomial tailored to the type and the error-correcting capability required. In the special case of an RS code, the generator polynomial may be expressed as:

$$g(x) = (x+\alpha)(x+\alpha^2)\ldots(x+\alpha^{2t}); \tag{3.13}$$

where α is a primitive element in GF(2^M).

Encoding is usually performed in a systematic form meaning the block of k information bits can be found unaltered in the generated codeword. The different encoding operations are summarized in the following expression:

$$s(x) = [x^{(n-k)}u(x) \bmod g(x)] + x^{(n-k)}u(x); \quad (3.14)$$

where:

- $u(x)$ is the polynomial representing the k information symbols to be encoded;
- $s(x)$ is the polynomial representing the codeword to be transmitted; and
- 'mod' denotes the modulo operation over GF(2^M).

It can be seen from (3.14) that the information symbols of M bits will be located in the first k positions of the codeword while the 'n-k' remaining positions will be occupied by parity-check symbols.

Decoding

An important reason for the popularity of RS codes is the existence of efficient hard-decision decoding algorithms making possible and practical the implementation of relatively long codes. Among those, the Massey-Berlekamp algorithm is one of the most efficient [Lin83]. This algorithm provides the mean to determine the location and the value of the errors corrupting the received codewords. It may be summarized as follows:

- Calculate the syndrome values S_i, $i = 1, 2, ..., 2t$;
- Determine the error-locator polynomial $\Lambda(x)$ from the syndrome values;
- Determine the roots of $\Lambda(x)$ and thus the error location indexes;
- Given the error location indexes, calculate the error values; and
- Correct the indicated errors.

The '$2t$' syndrome values are determined by evaluating the received codeword $r(x)$ at the roots of the generator polynomial defined in (3.13); i.e.,

$$S_i = r(\alpha^i),\ i = 1, ..., 2t. \quad (3.15)$$

The error-locator polynomial is determined by finding the minimum-degree polynomial which satisfies the Newton's identity within the error correction capability of the code, i.e.

$$S_\nu + \Lambda_1^{(2t)} S_{\nu-1} + ... + \Lambda_{\nu-2}^{(2t)} S_2 + \Lambda_{\nu-1}^{(2t)} S_1 = 0; \quad (3.16)$$

where ν is the number of errors present in the received codeword ($\nu \le t$) and Λ_ν are the coefficients of $\Lambda(x)$[1]. This can be done through the iterative process shown in Table 3.1.

1. $\Lambda_j^{(i+1)}$'s are the coefficients of $\Lambda^{(i+1)}(x)$.

The variables d_i and l_i, and the polynomial $\Lambda^{(i)}(x)$ are updated at each of the iteration step as follows:

$$d_{i+1} = S_{i+2} + \Lambda_1^{(i+1)} S_{i+1} + \ldots + \Lambda_{l_{i+1}}^{(i+1)} S_{i+2-l_{i+1}}; \text{ and} \tag{3.17}$$

if $d_i = 0$ then

$$l_{i+1} = l_i; \text{ and} \tag{3.18}$$

$$\Lambda^{(i+1)}(x) = \Lambda^{i}(x); \tag{3.19}$$

else

$$l_{i+1} = \max(l_i, l_\rho + i - \rho); \text{ and} \tag{3.20}$$

$$\Lambda^{(i+1)}(x) = \Lambda^{(i)}(x) - d_i d_\rho^{-1} x^{(i-\rho)} \Lambda^{(\rho)}(x); \tag{3.21}$$

where ρ is any row prior to the ith row such that $d_\rho \neq 0$ and that the number in the last column of Table 3.1 is the largest.

TABLE 3.1. Iterative Process to Find the Error-Locator Polynomial

i	$\Lambda^{(i)}(x)$	d_i	l_i	$i-l_i$
-1	1	1	0	-1
0	1	S_1	0	0
1				
2				
.				
.				
.				
$2t$				

If there are no more than t errors present in the received codeword, then the polynomial obtained after $2t$ iterations is the correct error-locator polynomial. On the other hand, a received codeword having more than t errors would result in a polynomial of degree greater than $2t$ and could not be decoded properly.

The inverses of the roots of the error-locator polynomial indicate the error locations β_j and the error values may be determined by first defining $z(x)$ as:

$$z(x) = 1 + (S_1 + \Lambda_1^{(2t)})x + (S_2 + \Lambda_1^{(2t)} S_1 + \Lambda_2^{(2t)})x^2 + \ldots$$

$$+ (S_\nu + \Lambda_1^{(2t)} S_{\nu-1} + \Lambda_2^{(2t)} S_{\nu-2} + \ldots + \Lambda_\nu^{(2t)})x^\nu \tag{3.22}$$

Then the error values are given by:

$$e_j = \frac{z(\beta_j^{-1})}{\prod_{\substack{i=1 \\ i \neq j}}^{\nu} (1 + \beta_i \beta_j^{-1})} \tag{3.23}$$

To complete the decoding process, it suffices to correct the errors identified. This is done by adding the j values found in (3.23) to the respective symbols located at β_j in the received codeword. The addition operations are performed in the Galois field of the code.

3.6.2 Convolutional Codes

In convolutional coding, the information bit stream to be encoded is not divided into blocks as for block coding but is rather processed continuously in a linear shift register of length m. m defines the constraint length of the code and indicates the number of information bits over which each code bit depends upon. Note that a particular information bit remains in the shift register for '$\lceil m/k \rceil$' shifts and thereby influences the value of 'nm/k' consecutive code bits. Since n is the number of code bits produced for each k information bits applied at the input of the shift register, the rate of a convolutional code is defined as the ratio k/n.

As for block coding, a convolutional decoder tries to find the sequence of code bits that most closely resembles the received sequence. The comparison is facilitated by the fact that the contents of the shift register, and thereby its outputs, are highly repetitive. Only a limited number of sequences are possible as long as n and k are small integers. This is usually the case. Performance of convolutional decoders is measured in terms of the coding gain. The gain is defined as the difference in SNR required to achieve the same probability of error whether the sequence is coded or not.

Because of their simplicity of implementation and the relatively large coding gain that can be achieved, convolutional codes have been used in many applications. However, as opposed to block coding where long sequences of independent bits may be constructed, convolutional coding relies on the inter-dependency of successive coded bits. Because bursts of errors are likely to be encountered over time-varying fading channel; and, it is usual to implement interleaving techniques to make the code more efficient.

Encoding

A convolutional encoder operates on the information data stream using a linear-shift register. k bits at a time are fed to the input of an m-stage shift register. The information bits contained in the shift-register at that instant are then combined to produce n code bits. Combination of the shift register content is performed according to a set of generator polynomials $g(x)$ particular to the code used. The process is then repeated for each k bits of the information stream.

A rate 1/2 encoder with a constraint length of 3 is shown in Figure 3.10. The n generator polynomials $g_n(x)$ for such a code may be written as:

$$g_1(x) = x^2 + 1; \text{ and} \tag{3.24}$$

$$g_2(x) = x^2 + x + 1. \tag{3.25}$$

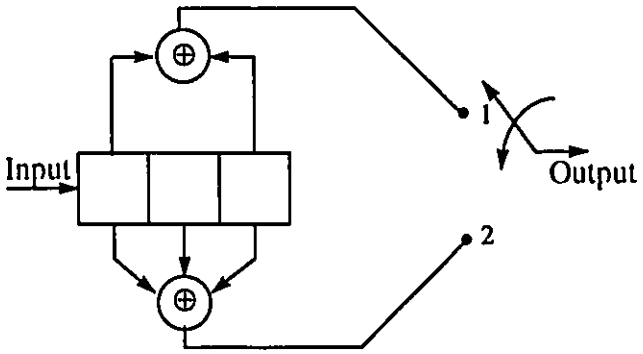

FIGURE 3.10. Rate-1/2 Convolutional Encoder With a Constraint Length of 3

As an example for the above encoder, it may be verified that for a binary sequence[1], where operations on the m-stage shift register are performed over GF(2), the following sequence of information bits:

$$[0\ 1\ 1\ 0\ 0] \tag{3.26}$$

will result in the sequence of code bits:

$$[00\ 11\ 10\ 10\ 11]. \tag{3.27}$$

Decoding

Because the coding gain achievable with a convolutional code depends on the decoding technique used, significant effort have been spent by researchers over the years

1. Although unusual, the sequence at the encoder input is not required to be binary. In that case, the operations on the m-stage shift register are performed over the Galois field defining the sequence symbols.

in designing efficient decoding techniques. Among them, sequential decoding and maximum-likelihood decoding are the two that are the most widely implemented. As oppose to sequential decoding which is mainly used for large constraint length codes, the maximum-likelihood decoding technique, referred to as the Viterbi decoding, is predominantly used for short constraint lengths ($m \leq 10$). Viterbi decoding has gained wide acceptance mainly because of its relatively simple decoder structure and of the high coding gain it achieves. Part of this gain is due to the fact that the Viterbi decoder can easily accommodate soft-decision decoding, thereby gaining 2 dB over AWGN channels and even more over time-varying fading channels [Proak89].

The convolutional encoder algorithm may be developed as a trellis where each node of the trellis identifies one of the possible states of the linear-shift register. The trellis for the encoder of Figure 3.10 is shown in Figure 3.11. Viterbi decoding is performed by determining the path through the trellis resulting in the smallest distance or metric with the received bit stream.

The Viterbi algorithm may be summarized as follows [Lin83]:

"

Step 1:Beginning at time unit $j = m$, compute the partial metric of the path entering each state. Store the path and its corresponding metric for each state.

Step 2:Increase j by 1. Compute the partial metric of all the paths entering a state by adding the branch metric entering that state to the metric of the connecting survivor previously kept at j-1. For each state, store the path having the largest metric (i.e. the survivor), together with its metric, and eliminate all other paths.

Step 3:If $j < (T_L + m)$, repeat step 2. Otherwise, stop[1].

"

As an example, the survivor path; i.e. the path that has the smallest metric, is shown in the trellis of Figure 3.11. The path results from the following received sequence of '$T_L \cdot n$' code bits, where the bit in error is underlined:

$$[00\ 11\ 1\underline{1}\ 10\ 11]. \tag{3.28}$$

The decoded output sequence is the sequence of information bits:

1. T_L identifies the sequence length.

$$[0\ 1\ 1\ 0\ 0] \tag{3.29}$$

which is identical to the sequence in (3.26).

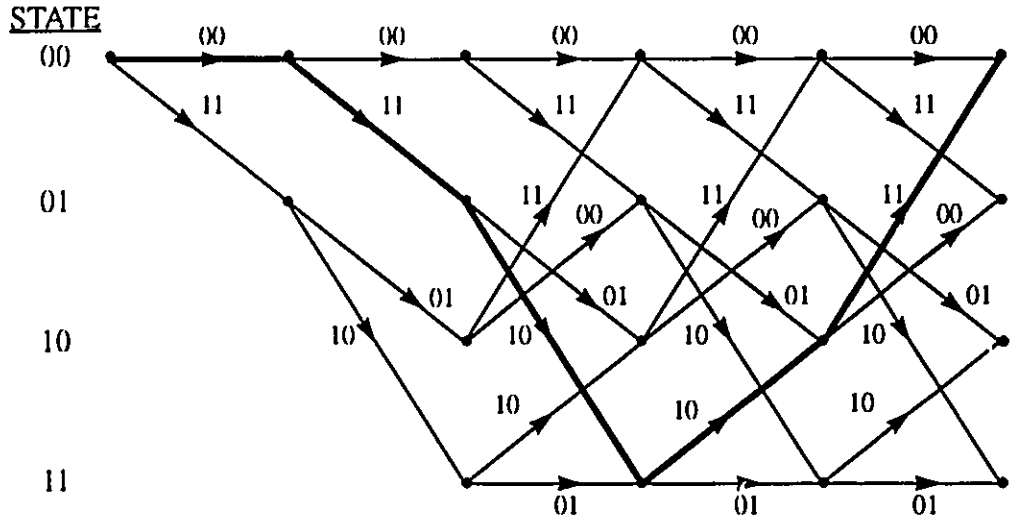

FIGURE 3.11. Trellis for a Constraint Length-3 Convolutional Code

3.6.3 Interleaving

A good method for improving the performance of any code in channel where errors tend to occur in bursts, is to permute the ordering of the encoder output sequence prior to transmission, and to perform the inverse process prior decoding. This deterministic process, referred to as *interleaving*, results in a more uniform distribution of errors at the decoder input. Two types of interleaver are commonly used: block and convolutional interleavers.

Example of a block interleaver is shown in Figure 3.12. In this type of interleaver, l generated codewords are stored in an '$l \times n$' array where each row is a codeword to be transmitted. Once the array is filled up, transmission is done column by column; i.e, l coded bits are transmitted at a time. Once all the columns of the array have been transmitted the process starts over. At the receiver, the inverse process takes place to reconstruct the codeword before performing the decoding. As it can be seen from Figure 3.12, if the time between each burst is longer than '$ln \times T_s$' and that the burst durations are smaller than l then no more than one error will be present in any one of the received codewords. When used with convolutional coding, the number of columns is usually set equal to the constraint length m. Although simple to implement, block interleaving requires large amount of memory at both the transmitter and receiver. Another potential problem is the systematic delay introduced by filling in the array. The overall memory requirement and the interleaving delay may both be computed as '$2l \times n$'.

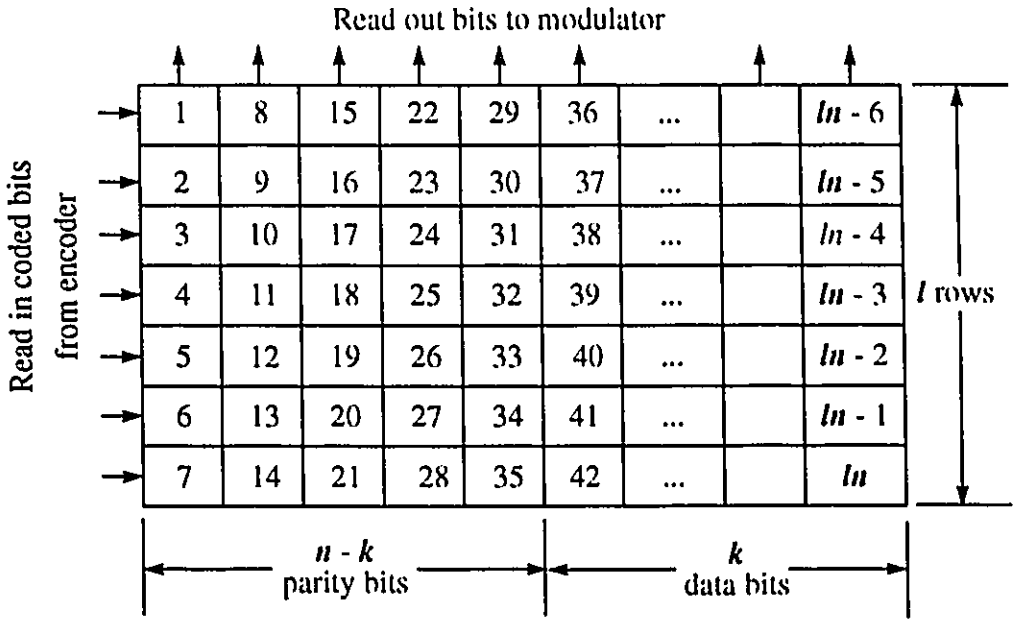

FIGURE 3.12. Block Interleaver

On the other hand, convolutional interleaving offers an alternative by reducing in half both the amount of memory required and the interleaving delay. Its operation is analogous to a time multiplexer as shown in Figure 3.13. In short, it consists in loading coded bits sequentially into a bank of linear-shift registers of increasing length. With each new coded bit, the switch changes to a new register and a new coded bit is shifted in while the oldest bits of the same register is shifted out. The input and output switches operate synchronously.

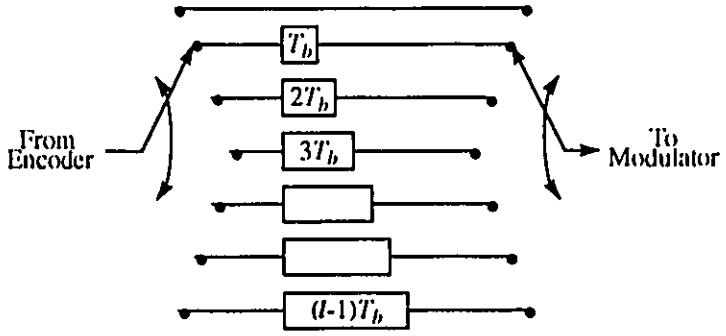

FIGURE 3.13. Convolutional Interleaver

3.7 Conclusion

In this chapter, direct sequence spread spectrum is introduced as an adequate technique for mitigating the detrimental effects of multipath fading and as a means of

exploiting the inherent multipath diversity of the HF channel. The RAKE receiver which is considered the optimum receiver implementation in such a case is described. Finally, the use of error control coding and interleaving techniques as a way of implementing time diversity is addressed.

Improvement in performance of such mitigation techniques must be assessed over a variety of channel conditions. It is however necessary that the evaluation tests take place under a controlled environment in order to draw meaningful conclusions. Computer simulation is one possible approach and is addressed in the next chapter.

Chapter 4
Description of Simulated System

4.1 Introduction

In Chapter 3, potential techniques for mitigating the detrimental effects of wideband HF channel were identified. Performance improvements that can be achieved with these techniques are usually measured in terms of the bit error probability P_b for a given SNR. The fastest method of obtaining performance information would be to derive an analytical relationship between SNR and P_b in terms of the channel parameters. However, as mentioned in Chapter 2, deriving such an expression is difficult due to the lack of definitive characterizations for the wideband HF channel parameters. It is therefore necessary to resort on the use of *Monte-Carlo* simulations with channel modeling as described in Chapter 2.

This chapter provides a description of the baseband communication system model used to measure BER performance. Description of the transmitter, the channel implementation, and the receiver are presented successively in Section 4.2, and assumptions made are pointed out.

4.2 System Description

The generalized one-way baseband communications system model used for the simulation is illustrated in Figure 4.1.

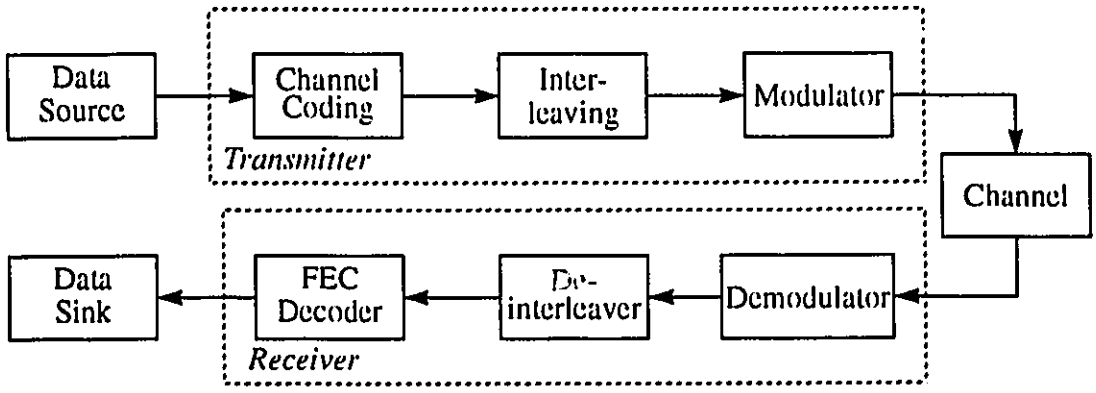

FIGURE 4.1. One-Way Communications System Model

It consists of a source producing the information to convey over the channel, a transmitter, the channel through which the information travels, a receiver to extract the wanted information from the corrupted received signal, and a data sink representing the

ultimate destination to reach. The first four blocks are described in more details in the following sub-sections. Description of the data sink is omitted because it may be any type of end-user equipment. For the purpose of the simulation carried out in this work, it is replaced by a bit comparator to determine the number of errors made over the link during a given transmission period.

4.2.1 Information Source

The information source consists of a pseudo-noise (PN) sequence of equally probable and independent binary data bits produced at a rate of 2400 bps. The sequence is an *m*-sequence of length 18 and is generated by the linear-feedback shift register depicted in Figure 4.2. The shift register primitive polynomial is [Lin83]:

$$g(x) = x^{18} + x^7 + 1. \tag{4.1}$$

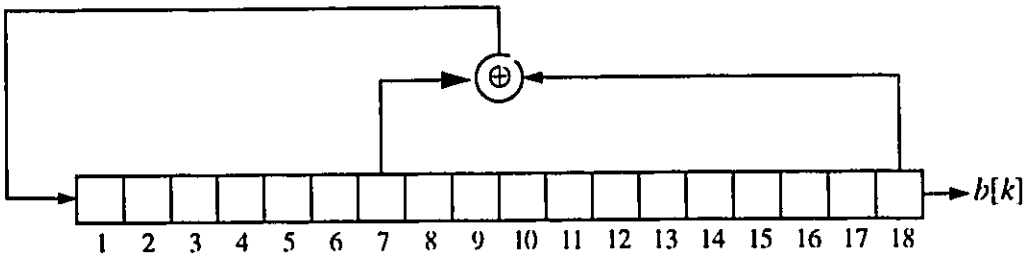

FIGURE 4.2. Linear Feedback Shift Register of Length 18 for Generating PN Sequences

4.2.2 Transmitter

The information bits received from the source generator are processed by the transmitter into a form adequate for transmission. The transmitter used for carrying out the simulation is illustrated in Figure 4.3. It consists of a channel encoder unit, a modulator unit, and a filtering unit.

Channel Encoder Unit

As mentioned in Chapter 3, the roles of the channel encoder are first to insert redundant information into the bit stream for the purpose of detecting and correcting transmission errors at the receiver, and secondly, to introduce time diversity. For the purpose of this thesis, both convolutional and Reed-Solomon codes are implemented.

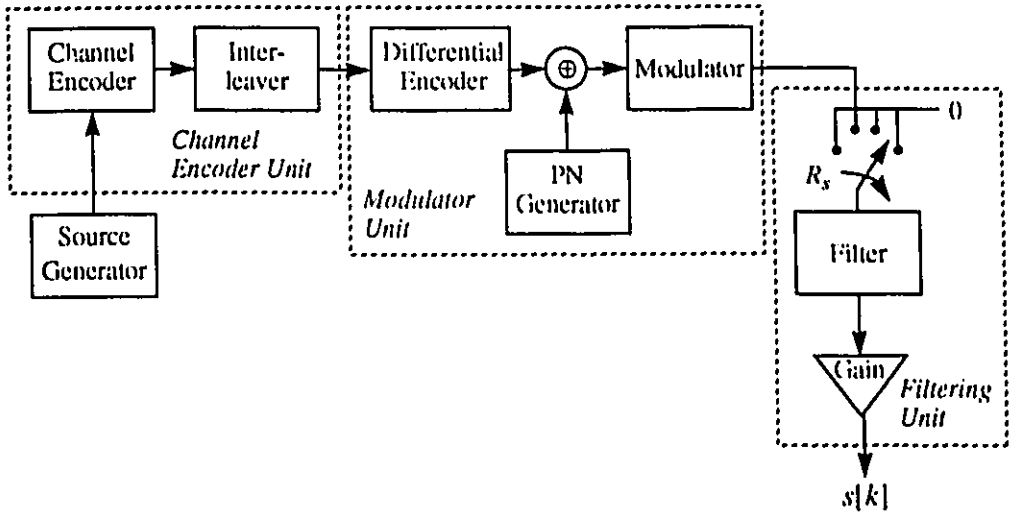

FIGURE 4.3. Baseband Transmitter Diagram

Reed-Solomon Coding

A Reed-Solomon code is constructed over GF(2^6) with the following primitive polynomial [Lin83]:

$$g(x) = x^6 + x + 1. \tag{4.2}$$

More specifically, a (63, 31) 16-error RS code and a (63, 41) 11-error RS code are implemented; thereby setting the coding rate to approximately 1/2 and 2/3 respectively. Encoding is performed in a systematic form according to (3.14).

Convolutional Coding

The common convolutional code of rate 1/2 and constraint length 7 is used. The generator polynomials are those suggested in [Lin83] when Viterbi decoding is implemented. The encoder is illustrated in Figure 4.4.

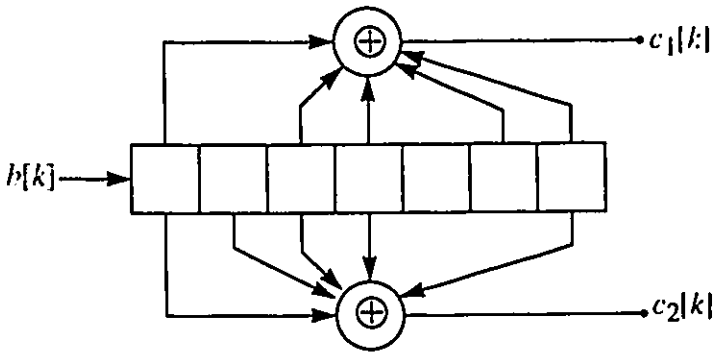

FIGURE 4.4. Convolutional Encoder

The generator polynomials for the encoder shown in the above figure may be written as:

$$g_1(x) = x^6 + x^5 + x^3 + x^2 + 1; \text{ and} \tag{4.3}$$

$$g_2(x) = x^6 + x^3 + x^2 + x + 1. \tag{4.4}$$

Interleaving

To alleviate the relatively small error-burst correcting capability of convolutional codes, further simulations are performed with interleaving. The convolutional interleaver depicted in Figure 3.13 is implemented. The number of registers is set to 8; i.e. the first multiple of n ($n = 2$) greater than the constraint length m ($m = 7$); while the interleaving degree I is adjusted to set the delay to approximately 2 sec; i.e. 4800 bits. These numbers are chosen as a reasonable compromise between the memory requirement and the simulated fading periods (between 20 msec and 5 sec).

Modulator Unit

The modulator unit assigns a particular phase pattern to each possible sequence of input bits. In the case of a DSSS non-coherent communication system, it consists of a differential encoder, a bandwidth spreading device, and a phase modulator.

Differential Encoder

The differential encoder output is complemented every time a "1" is fed at its input, otherwise the amplitude remains unchanged when it is a "0". The state diagram at the output of the encoder is illustrated in Figure 4.5.

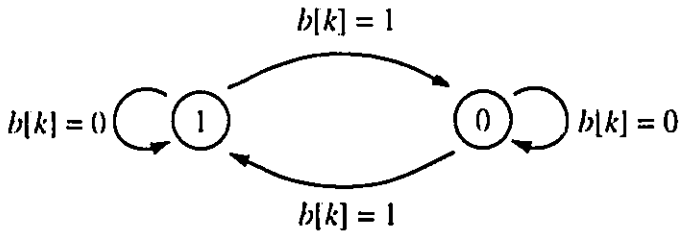

FIGURE 4.5. Differential Encoder State Diagram

The encoding operation is implemented mathematically according to the following relation with the initial bit "$b[-1]$" sets to "1":

$$d[k] = b[k] \oplus d[k-1]; \tag{4.5}$$

where:

- $b[k]$ is the kth bit generated by the information source; and
- $d[k]$ is the kth bit at the output of the encoder.

Bandwidth Spreader

For convenience purposes, the spreading sequence is applied to the information bit sequence before modulation. The operation consists of summing the differential encoder output bit with the binary digit produced by the PN generator using a modulo-2 adder. The number of chips produced over one bit interval sets the processing gain.

The PN sequence spreading the signal is the same one used for the information source. Decorrelation of the two sequences is ensured by delaying one from the other by approximately $[2^m]/2$ shifts [Jeru92]; m being set to 18.

Phase Modulator

Binary phase modulation consists of mapping an incoming chip to a phase $\theta[k] \in \{0, \pi\}$. The resulting baseband waveform may be expressed as:

$$v(t) = \sum_k A[k]\, u(t - kT_c)\,. \tag{4.6}$$

$\{A[k]\}$ is the complex valued sequence resulting from the mapping operation. $A[k]$ takes the value "1"; i.e. a phase of 0 rad, if the kth incoming chip has the value "1" while $A[k]$ takes the value "-1"; i.e. a phase of π rad, if the kth incoming chip has the value "0". The waveform $u(t)$ determines the shape of the transmitted signal spectrum. It is discussed in more details hereafter.

Filtering Unit

The filtering unit serves four purposes: sampling, pulse shaping, band-limiting, and adjusting the signal power of the signal to be transmitted.

Sampling and Pulse Shaping

The modulated signal must be sampled at a sufficient rate to obtain an adequate representation of its characteristics. As per Nyquist, a rate that is twice the chip rate is sufficient. However, because the sampling rate also affects the representation of the channel characteristics, it is often required that over-sampling of the signal be performed. A sampling rate between 4 and 16 times the chip rate is usually adequate [Jeru92]. Because the time required for carrying out the simulations increases as the sampling rate gets larger, a value of four is adopted; thereby setting the sampling rate to $4\,R_c$.

The sampler is followed by pulse shaping of the modulated chip waveform $v(t)$. Only one sample out of the four produced for each chip is kept to its current value, the other three are set to zero. Since each chip at the input of the filter appears by this operation similar to an impulse, the waveform resulting from the convolution in the time-domain between the modulated signal and the filter impulse response becomes almost independent of the signal itself. The signal to be transmitted may then be adequately shaped by choosing the appropriate band-limiting filter to minimize ISI. The energy lost by setting the three samples to zero is made for by adjusting the output amplitude of the modulated signal accordingly.

Band-Limiting Filter

In order to minimize inter-symbol interferences over a band-limited channel, the overall transmitter/receiver frequency response $H_c(e^{j\omega})$ should comply to the Nyquist criterion [Proak89]. Raised-cosine filters present such frequency response characteristics and are therefore adopted in the present implementation.

Because $H_c(e^{j\omega})$ is in fact the composite frequency response of both transmitter and receiver filters, it may be expressed as:

$$H_c(e^{j\omega}) = H_{Tx}(e^{j\omega})\,H_{Rx}(e^{j\omega}). \tag{4.7}$$

Optimal partitioning of $H_c(e^{j\omega})$ between the transmit and the receive filters was shown to be [Jeru92]:

$$H_{Tx}(e^{j\omega}) = \left|H_c(e^{j\omega})\right|^{1/2} e^{j\theta_{Tx}(\omega)}; \text{ and} \tag{4.8}$$

$$H_{Rx}(e^{j\omega}) = \left|H_c(e^{j\omega})\right|^{1/2} e^{j\theta_{Rx}(\omega)}. \tag{4.9}$$

Thus, the frequency response of both the transmitter and the receiver filters must display the same characteristics.

The normalized impulse response, $h(t)$, and squared magnitude $\left|H(e^{j\omega})\right|^2$, of the band-limiting filter implemented are shown in Figure 4.6. The filter is a square-root raised-cosine FIR filter with 13 coefficients. Its coefficients are defined by the following equation using a sampling rate of four times the chip rate R_c:

$$h(t) = \frac{1}{\pi}\left[\frac{\sin[\pi(1-\beta)\,t/T_b]}{t\left[1-(4\beta t/T_b)^2\right]} + \frac{4\beta}{T_b}\cdot\frac{\cos[\pi(1+\beta)\,t/T_b]}{1-(4\beta t/T_b)^2}\right]; \text{ and} \tag{4.10}$$

$$H(e^{j\omega}) = \begin{cases} 1 & |f| \le f_1 \\ \cos\left(\frac{\pi}{2}\left(\frac{f-f_1}{f_2-f_1}\right)\right) & f_1 < |f| < f_2 \\ 0 & |f| \ge f_2 \end{cases} ; \qquad (4.11)$$

where the roll-off factor or excess bandwidth β is set to 0.2.

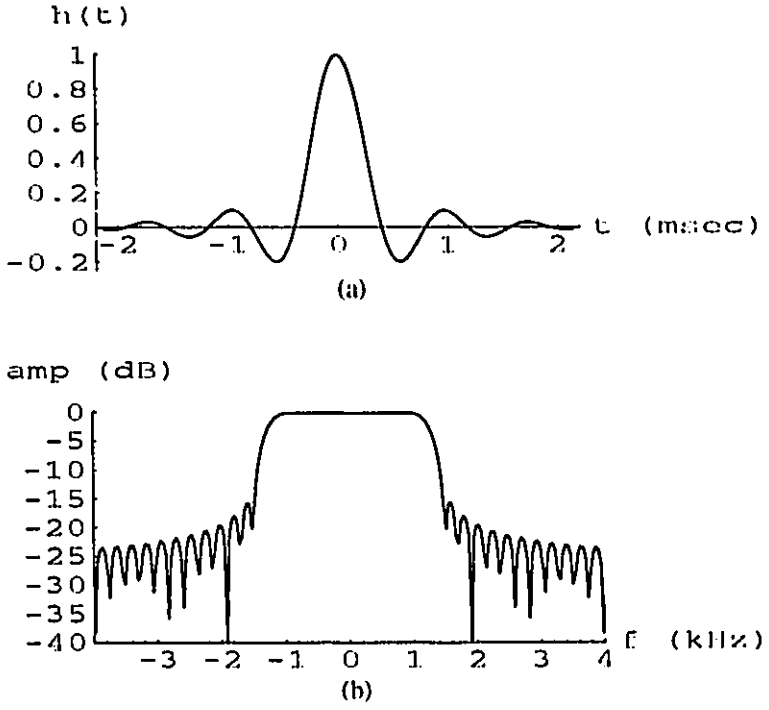

FIGURE 4.6. Band-Limiting Filter: (a) Impulse Response, (b) Squared Magnitude of the Frequency Response

The 3-dB filter bandwidth is set to a multiple of $|2400 \times (1+\beta)|$ Hz according to the processing gain used; i.e:

$$W_{ss} = PG \times (1+\beta) \times 2400. \qquad (4.12)$$

4.2.3 Channel Implementation

The Ionospheric Parameter model for wideband channel presented in Chapter 2 has been implemented in software as shown in Figure 4.7. The following assumptions have been made to reduce the simulation complexity:

- The channel is linear;

- The relative strength of each mode remains constant for the duration of the whole transmission; and
- The channel displays slow fading with regard to the bit rate R_b.

For the block diagram showed in Figure 4.7, the different variables are defined as follows:

- $s[k]$ is the kth transmitted sample;
- τ_n is the median delay of the nth path;
- $c_n[k]$ is the kth sample of the time-varying tap gain defined by the frequency dispersion of the nth path;
- $x[k]$ is the kth noise sample; and
- $r[k]$ is the kth received sample.

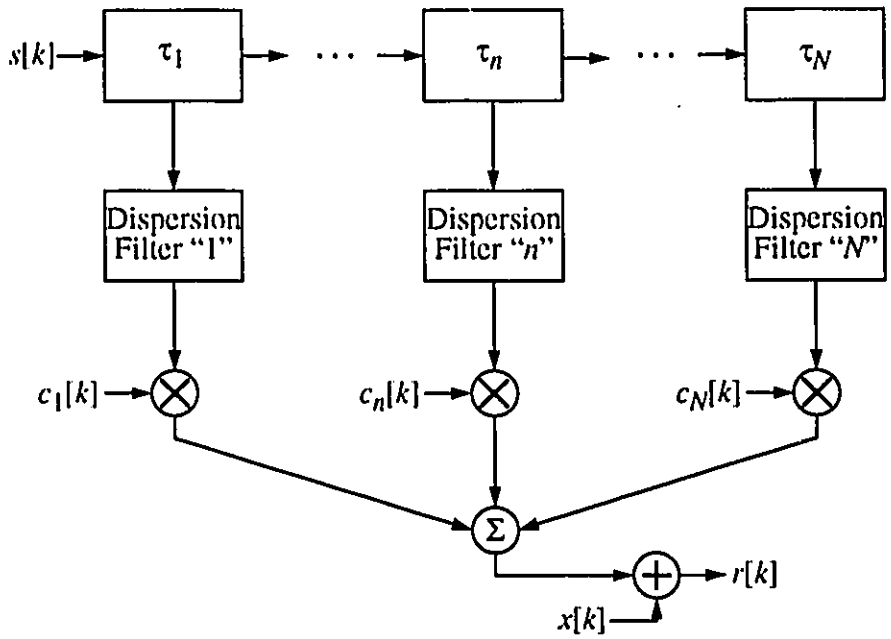

FIGURE 4.7. Wideband Channel Model Used in Simulation

Delay Dispersion

Multipath dispersion is modeled as a tap-delay line where the median delay of each path is determined using (2.33), and (2.34) of the deterministic model described in Chapter 2. On the other hand, the delay dispersion described by the stochastic model is implemented as an FIR filter. The number of coefficients characterizing the filter is a function of the dispersion in each mode (or branch) of the model. The coefficients are determined by (2.37) at the sampling rate defined for the transmitter. The magnitude of all the complex coefficients is adjusted to obtain an overall average power level of one; i.e. $E(\alpha^2) = 1$. The output of the different dispersion filters is determined by performing a

convolution in the time-domain between the delayed transmitted samples and the dispersion filter coefficients.

Frequency Dispersion

Each complex coefficient $c_n[k]$ is assumed to be Rayleigh distributed in amplitude and uniformly distributed in phase over the interval $[0, 2\pi[$. Thus, the probability density functions (pdf) for the amplitude $f_R(r)$ and for the phase $f_\Theta(\theta)$ may be expressed respectively as:

$$f_R(r) = \frac{r}{\sigma^2} e^{-r^2/2\sigma^2}, \; 0 \le r < \infty; \text{ and} \tag{4.13}$$

$$f_\Theta(\theta) = \frac{1}{2\pi}; \quad 0 \le \theta < 2\pi. \tag{4.14}$$

The average power level of each coefficient has a value of one. The coefficients are generated as shown in Figure 4.8.

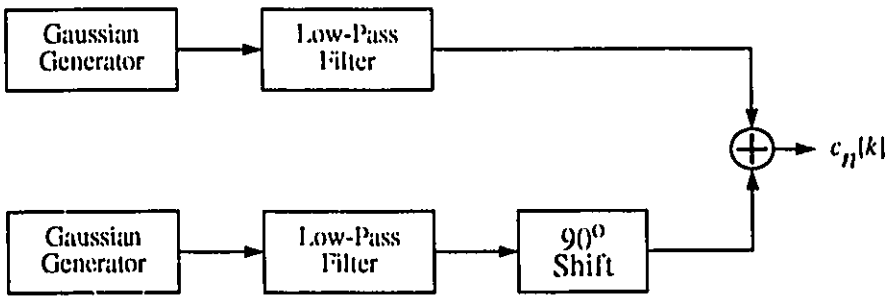

FIGURE 4.8. Generation of Tap-Gain Coefficients

The complex coefficient generation process consists of filtering samples from two independent zero-mean Gaussian generators of variance equal to one. Each low-pass filter has a 3-dB bandwidth equal to one half of the double-sided Doppler spread B_D of the corresponding path. The in-phase and quadrature outputs are then added to form the complex coefficient $c_n[k]$.

The low-pass filters are 2-pole Butterworth IIR filters whose squared magnitude of their frequency response $|H_B(f)|^2$ may be written as:

$$|H_B(f)|^2 = \frac{1}{1 + \left(\frac{f}{B_D}\right)^2}. \tag{4.15}$$

Derivation of the recursive equations required for implementing the IIR filters is summarized in Appendix C.

The coefficients $c_n[k]$ are characterized in Figures 4.9, 4.10, and 4.11 for a Doppler spread of 1 Hz. Figure 4.9 represents the squared magnitude of the frequency response $|H_B(f)|^2$ while Figures 4.10 and 4.11 show the pdf's $f_R(r)$ and $f_\Theta(\theta)$ of the coefficient $c_n[k]$. 2,500,00 samples were used to derive the simulation curves. Note that the spectra in each branch of the fading generator are identical.

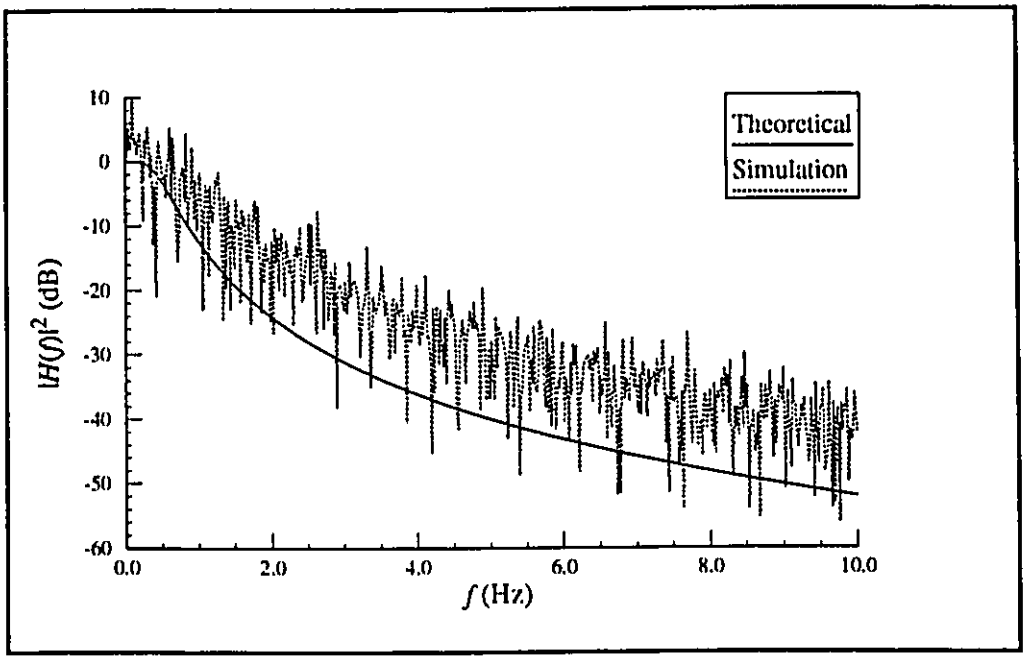

FIGURE 4.9. Squared Magnitude of the Frequency Response $|H_B(f)|^2$ of the Filtered Noise Sources

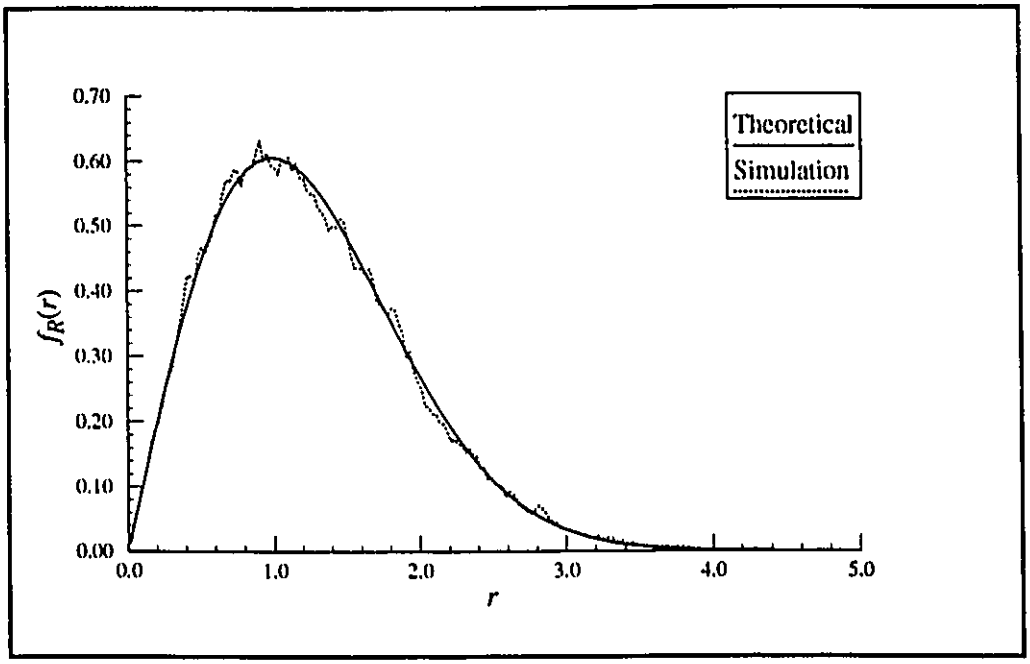

FIGURE 4.10. Probability Density Function $f_R(r)$ of the Fading Coefficient Amplitude

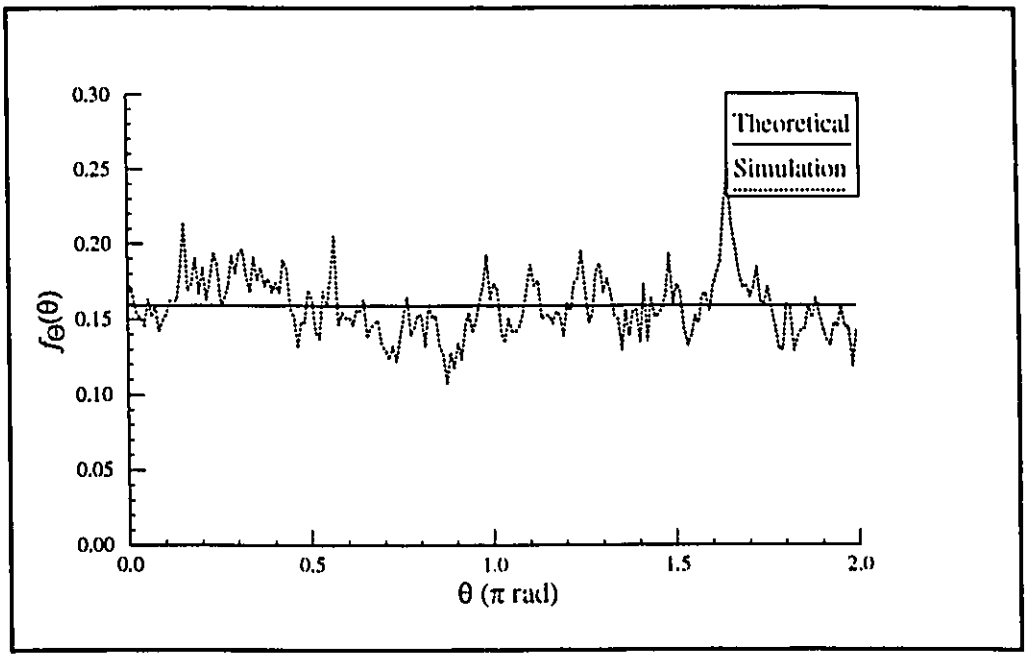

FIGURE 4.11. Probability Density Function $f_\Theta(\theta)$ of the Fading Coefficient Phase

Noise Generation

As discussed in Chapter 2, the HF channel is subject to severe noise conditions and strong interference levels. Several papers have already demonstrated the advantages of using spread spectrum techniques to mitigate the adverse effects of interference and bursty noise on system performance [Ziem85], [Proak89]. For this reason, only zero-mean complex white Gaussian noise have been included in the channel model.

Noise is generated via the use of the central limit theorem according to the common expression:

$$x[k] = \sum_{n=1}^{N} U[n] - \frac{N}{2}. \tag{4.16}$$

The constant N is set to 12 in (4.16). This number represents a reasonable trade-off between processing speed and calculation accuracy [Jeru92]. U[n] is a sequence of independent numbers uniformly distributed over $[0, 2^{31}[$. The generator has a power spectral density of N_0. Its level is normalized to one by multiplying the output of the noise generator by the square-root of half the sampling rate; i.e, $\sqrt{R_s/2}$. The Cumulative Distribution Function (CDF) $F_X(x)$ and the pdf $f_X(x)$ of the Gaussian noise are shown in Figure 4.12. 2,500,000 samples were used to generate each curve. The same results were obtained for both the imaginary and real components of the noise source.

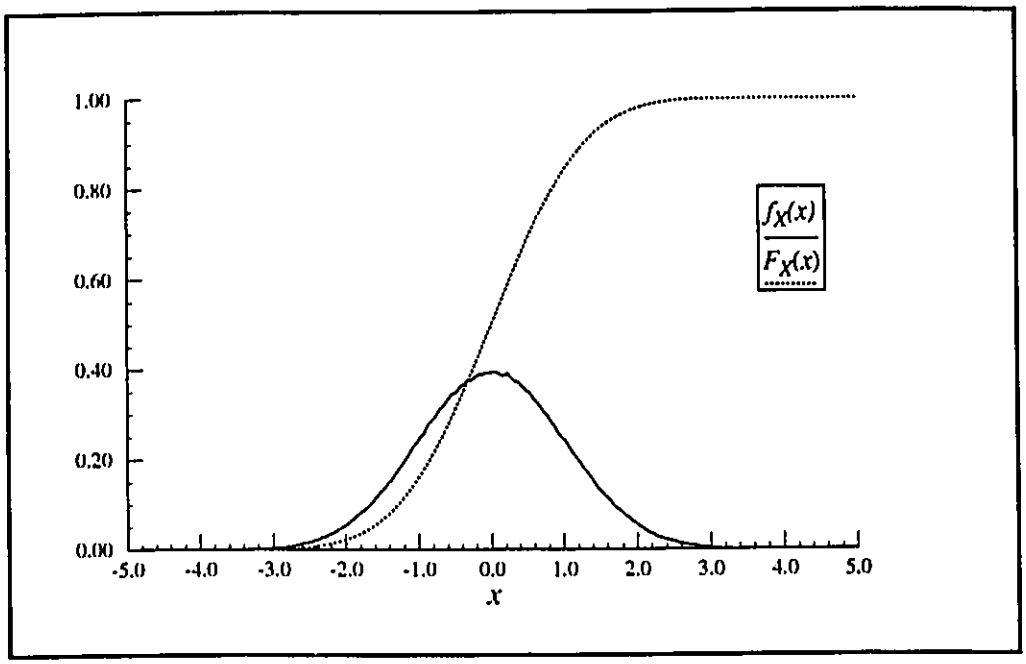

FIGURE 4.12. Probability Density Function $f_X(x)$ and Cumulative Distribution Function $F_X(x)$ of the AWGN Source.

4.2.4 Receiver Description

The block diagram of the RAKE receiver is shown in Figure 4.13. Basically, it consists of a low-pass filter identical to the band-limiting filter used at the transmitter, a tap-delay line with tap separation of one or more samples, an equal-gain combiner, and a decision device. Each tap is composed of a (4:1) decimator followed by a correlator, a local PN generator, an I&D device, and a DPSK demodulator. The deinterleaver and the decoder are treated as separate entities and are discussed in the next sub-sections.

Tap-Delay Line

Construction of the tap-delay line is based on the assumption that both the median delay and the average power of each path are perfectly known, so that each tap of the receiver is perfectly synchronized. The maximum number of taps is limited to 50 or to the number of taps necessary to cover the overall multipath dispersion of the simulated channel; whichever is the smaller. A limit of 50 was chosen based on the memory available and processing power of the simulation platform.

In cases where dispersion extends over $50 \times T_s$, where T_s is the sampling period, the taps belonging to the paths displaying the highest average power level are kept. All other paths are discarded and their energy is considered lost.

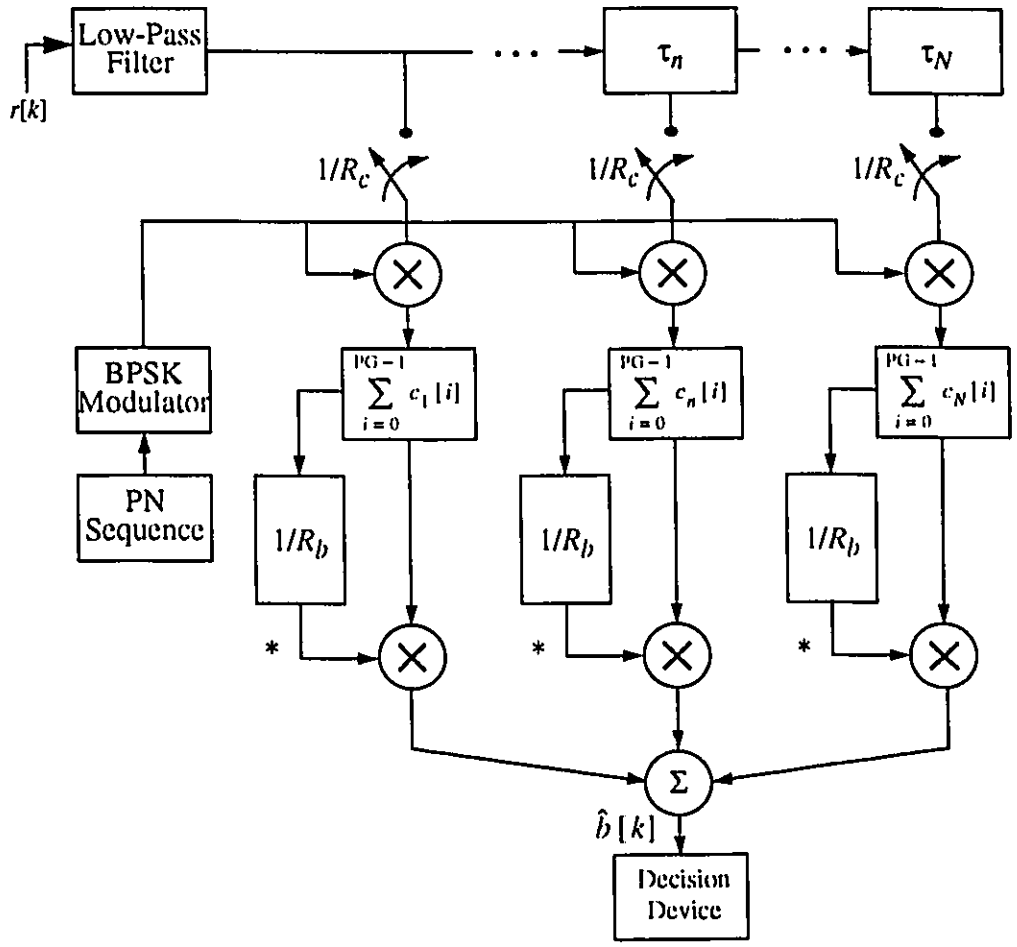

FIGURE 4.13. Rake Receiver

Tap Description

The sample stream entering each tap is decimated by a ratio (4:1). The output values are taken as the values of the received chips. Since synchronization with the transmitter is assumed perfect, the non-zero samples at the transmitter are always chosen as output samples during decimation.

Correlation with the locally generated PN sequence is performed by multiplying the received chips with the complex conjugate of the modulated sequence. Correlation is followed by a discrete I&D operation conducted over one bit interval T_b. DPSK demodulation is then performed with the resulting bit sequence. The outputs of the demodulators are finally combined. It can be seen that for DPSK modulation, the weight of each tap depends on the complex amplitude of the previous bit.

Decision Device

The decision device may either produce hard or soft-decision information. In the case of hard-decision, the received bits are estimated exclusively on the sign of the real component of the combiner output. Thus, if the real part of $\hat{b}[k]$ is greater or equal to zero, then a "0" is decided; else, if the real part of $\hat{b}[k]$ is less than zero, then a "1" is decided. On the other hand, when soft-decision is used, the real part of $\hat{b}[k]$ is kept for decoding. The quantization level is set to 64 bits: the maximum accuracy of the computer used. It may therefore be regarded as infinite. In this work, hard-decision is implemented for RS coding while soft-decision is used for convolutional coding.

Deinterleaving

As mentioned earlier, interleaving is used with convolutional coding only. The deinterleaver simulated has the same structure as the one described in Figure 3.13. The size of the registers is set to 8, while the interleaving delay is set to 2 sec; i.e 4800 code bits.

Decoding

Decoding of the RS codes is performed with the Massey-Berlekamp algorithm described in Chapter 3. In the case where the degree of the error location polynomial $\Lambda(x)$ exceeds the error correcting capability t of the code, no attempt to decode the received codeword is made. In this case, because systematic encoding is performed at the transmitter, the first k symbols of the undecodable codeword are taken as the best symbol estimate.

In the case of convolutional coding, the decoder is based on the Viterbi algorithm where a decoding depth of 16 times the constraint length is used. Although a smaller decoding depth is often sufficient for memoryless channels, the large delay dispersion in the simulated channel prevent us from obtaining adequate performance while a larger value did not provide significant increase in performance.

4.3 Conclusion

In this chapter, the communication model system used for simulation is described. Essentially, it may be regarded as a DSSS modem transmitting at a rate of 2400 bps over a wideband HF channel. The whole communication link is implemented at baseband under the assumption that the transmitter and the receiver are perfectly synchronized. The channel is based on the IPM model with AWGN only. Additional assumptions made on the channel to ease the simulation work are pointed out to set the basis for the result analysis presented in the next chapter.

Chapter 5
Simulation Results

5.1 Introduction

The communication model described in Chapter 4 is used to evaluate the performance of different RAKE receiver implementations over three simulated wideband HF channels. The main criterion of performance is the bit error probability P_b as a function of E_b/N_o.

The main characteristics and assumptions regarding the simulated transmitter/receiver implementations are summarized in Section 5.2. Section 5.3 brings attention on the particularities of the channel being simulated. Ionogram and scattering functions provide a good representation of the wideband HF channel conditions and are included with each channel simulated. Finally, the simulation results of P_b vs E_b/N_o are analyzed in Section 5.4.

5.2 Transmitter/Receiver Characteristics

The main characteristics of the transmitter/receiver model described in Chapter 4 are summarized hereafter. It must be noted that this model is developed at baseband and that perfect synchronization between the transmitter and the receiver is assumed at all time.

- Information data rate: 2400 bps
- Spreading technique: Direct Sequence Spread Spectrum
- Processing gain PG[1]: 1, 25, 33, 50
- Modulation: DPSK
- RAKE receiver:
  - No. of taps: 1 to 50
  - Minimum tap-spacing: 1 sampling period T_s
  - Tap-combiner: Equal-Gain Combining

1. The processing gain is indicated as the number of chips over one bit period T_b.

- Tx/Rx band-limiting filters:
  - Type: 13-coefficient square-root raised-cosine FIR filter
  - Roll-off factor β: 0.2
  - Bandwidth: $PG \times 2400 \times (1 + \beta)$
- Interleaving/deinterleaving:
  - Type: Convolutional
  - Number of registers: 8
  - Interleaving delay: 2 sec or 4800 bits
- Coding/decoding:
  - RS code:
    - 16-error (63,31) and 11-error (63,41)
    - Decoding: Massey-Berlekamp algorithm with hard-decision information
  - Convolutional code:
    - R1/2C7
    - Decoding:
      - Viterbi algorithm with soft-decision information
      - Decoding depth: 112 bits ($16 \times m$)
      - Quantization levels: 64 bits

5.3 Channel Characterization

The simulations have been conducted over three different wideband HF channels selected for their type of dispersion and fading conditions. The first two simulated channels are representative of ionospheric conditions often encountered at equatorial and polar latitudes. The third channel models a communication link established at auroral latitudes where a high level of ionospheric activity is typically observed.

The parameters used for characterizing each HF channel are listed in Table 5.1. These channels were first modeled by Vogler in [Vogl90] and are used "as is" in the simulation except for the time dispersion parameters (T_n and T_τ). Because time dispersion is a function of frequency, it must be adjusted to the signal bandwidth W. Assuming a direct proportionality with W, the values of T_n and T_τ given in [Vogl90] are weighted by a factor:

$$\frac{W(\text{MHz})}{1\,\text{MHz}}; \tag{5.1}$$

where 1 MHz is the channel bandwidth used in [Vogl90], to obtain the values shown in Table 5.1.

TABLE 5.1. Simulated Channel Parameters

	D (km)	f_c (MHz)	σ (km)	f_p (MHz)	h_o (km)	α	T_n (μs)	T_τ (μs)	B_D (Hz)	ν (Hz)	ν_L (Hz)
1	2158	11	7.2	56.7	472	1	880	220	4	0	0
						–	–	–	–	–	–
2	1913	12.5	5.72	19.22	306.8	0.34	250	135	14	0	0
						–	–	–	–	–	–
			5.72	19.22	364.5	0.84	400	100	32	0	0
						0.44	945	135	44	0	0
3	2300	12.5	4.25	8.43	374	1	100	40	0.3	0.2	0.1
						0.5	100	50	0.4	0.2	0
			4.25	8.43	374	0.5	60	25	0.2	−0.2	−0.3
						0.3	100	80	0.4	0	−0.1

The channel conditions are best represented by ionograms and scattering functions. While ionograms help in visualizing the delay dispersion frequency relationship, scattering functions display the short-term statistical characteristics of the channel, that is, the relative amplitude as a function of the Doppler shifts and the delay dispersion. The output of the deterministic model described in Chapter 2 is used to derive the ionogram of each channel selected for a bandwidth of 125 kHz. The scattering functions are produced by applying an impulse to the stochastic model. For the scattering functions plotted in this section, the model is based on the parameters provided for a 1 MHz channel bandwidth.

Equatorial Link

The first set of parameters in Table 5.1 were determined from measurements taken in July from a 2158-km east-west path in the Pacific Ocean. The parameters are representative of an F-layer return for a late night hour equatorial link. The delay dispersion T_n and the double-sided Doppler spread B_D are 880 μsec and 4 Hz respectively. The ionogram and the scattering function obtained by modeling this channel are shown in Figures 5.1, and 5.2.

Polar Link

The second set of parameters in Table 5.1 were determined from a 1913 km north-south path in the polar region over Greenland. The measurements taken in March indicates three skywave returns: one from the E-layer and one from the low and high rays of the F-layer. Considerably more movements in the layers were present, resulting in large Doppler spreads in each skywave return: B_D = 14 Hz, 32 Hz, and 44 Hz respectively. Fur-

thermore, the carrier frequency is close enough to the MUF of each mode to cause a large delay dispersion, T_n = 250 μsec, 400 μsec and 945 μsec, and a partial overlap between the low and high ray returns of the F layer. The ionogram and the scattering function for this channel are shown in Figures 5.3, and 5.4 respectively.

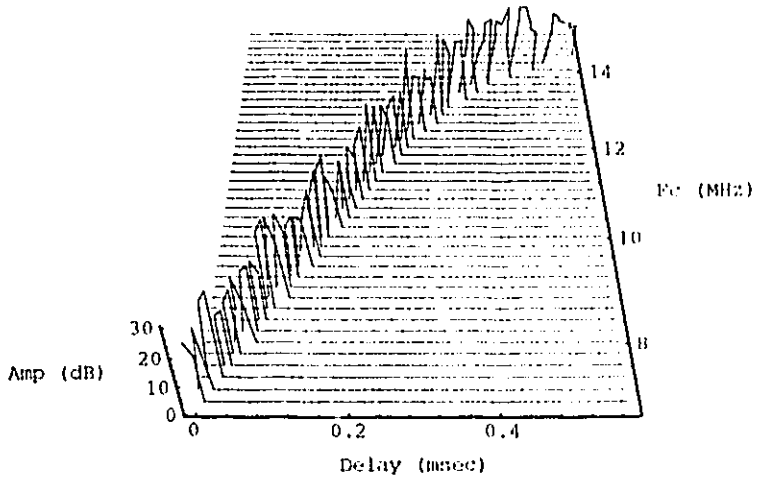

FIGURE 5.1. Ionogram of a 2158-km Equatorial Link

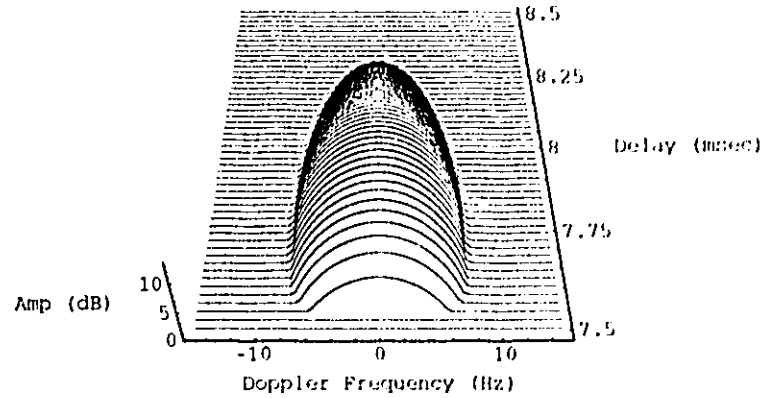

FIGURE 5.2. Scattering Function of a 2158-km Equatorial Link

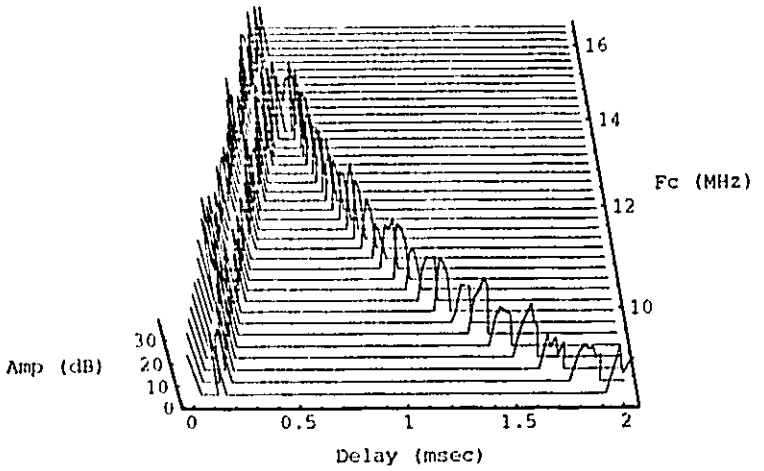

FIGURE 5.3. Ionogram of a 1913-km Polar Link

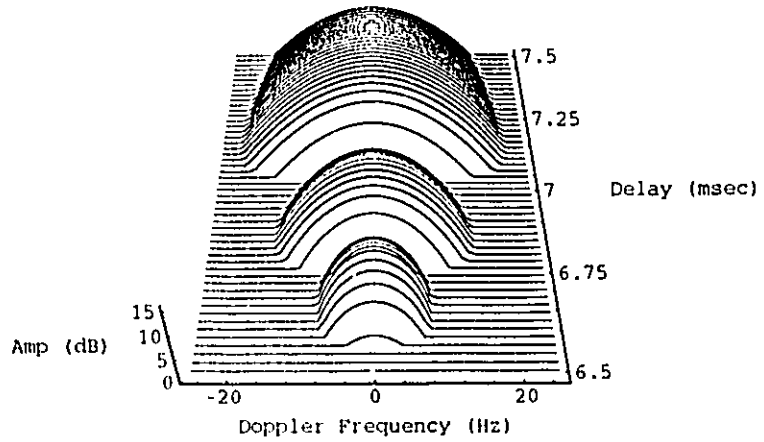

FIGURE 5.4. Scattering Function of a 1913-km Polar Link

Auroral Link

The third set of parameters in Table 5.1 pertains to an auroral link. It consists of two pairs of overlapping skywave returns. The complex ridge structure shown in Figure 5.6 is typical of such links since the ionosphere is much more dynamic at these latitudes. The parameters were determined from a 2300 km path between Verona, NY, and Iqaluit, NWT. The measurements were taken near midday in April under quiet magnetic condi-

tions. The ionogram and the scattering function are shown in Figures 5.5, and 5.6 respectively.

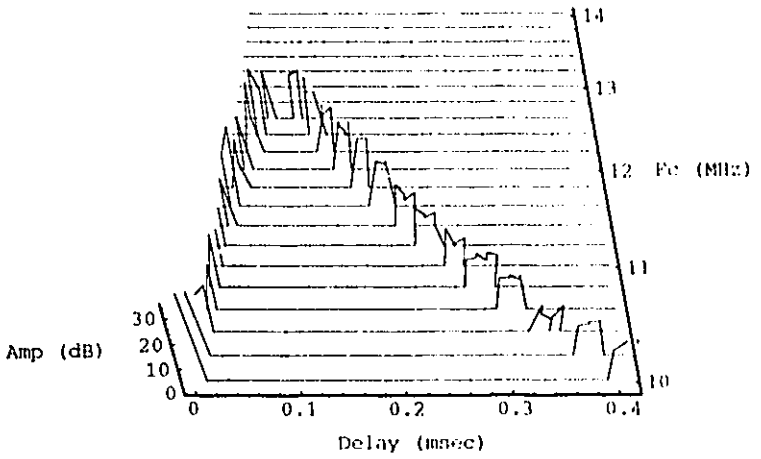

FIGURE 5.5. Ionogram of a 2300-km Auroral Link

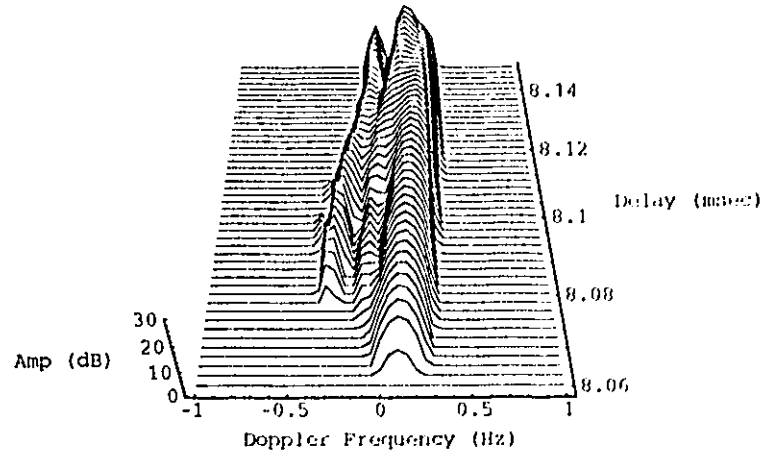

FIGURE 5.6. Scattering Function of a 2300-km Auroral Path

5.4 Performance Results and Analysis

The communication model described in Chapter 4 is used to estimate the bit error probability P_b versus E_b/N_o. The simulations are conducted over a fixed period of time equivalent to the transmission of 250,000 data bits; i.e. approximately 100 seconds,

and are repeated for each of the three channels. A minimum of 20 events (errors) must be recorded over that period in order to consider the measured performance as being acceptable.

Prior to the wideband channel simulation, the transmitter/receiver model has been evaluated for the basic AWGN and flat fading channels. Simulation results are compared with the expected theoretical data in Figure 5.7. It can be observed that in both cases, the simulation and theoretical curves are closely fit except for a divergence of less than 1 dB at their low end. It must be noted that similar performance has been obtained when DSSS was simulated.

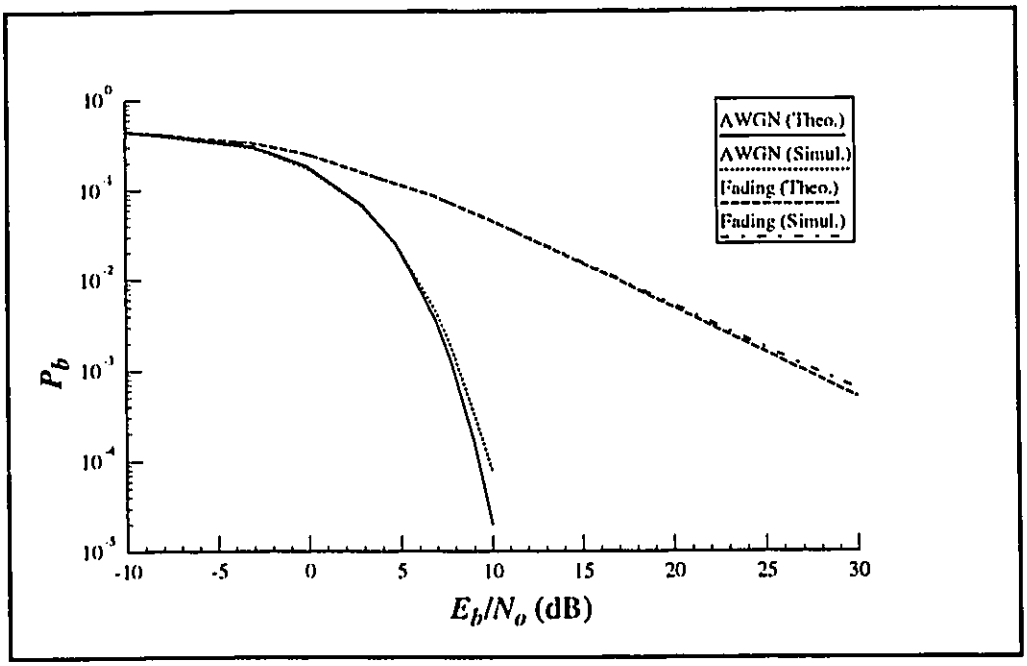

FIGURE 5.7. P_b **vs** E_b/No **for DPSK Transmission over AWGN and Fading Channels**

The simulation results that follow in Sections 5.4.1 to 5.5.1 are divided in three groups. The first group provides the estimate obtained with the correlator receiver shown in Figure 3.6. The second group covers the performance achieved with the Rake receiver model shown in Figure 4.13. Finally, the last set of results describes the performance of the RAKE receiver with error control coding and interleaving.

5.4.1 Performance of the Correlator Receiver

The performance of a simple correlator receiver has been estimated with and without spectrum spreading. Processing gains of 25 and 50 have been used, resulting in bandwidths of 72 kHz and 144 kHz respectively. Performance obtained from the simula-

tion of the three selected channels are shown in Figures 5.8, 5.9, and 5.10. The theoretical performance for a flat fading channel is included for comparison.

Equatorial Link

In the case of a single-path channel such as the simulated equatorial link, it can be observed (see Figure 5.8) that no gain is to be expected through the use of direct sequence spreading. Indeed, performance will degrade as the spreading bandwidth is increased; i.e. as the processing gain is increased.

The channel does not introduce significant delay dispersion when the channel bandwidth is small; i.e. when no spreading is performed. In this situation, the dispersion filter may be regarded as an impulse, reducing the channel to flat-fading conditions. On the other hand, when the signal is spread over wider bandwidth, the transmitted energy is dispersed. Dispersion results in amplitude reduction of the received signal components and inter-symbol interference (ISI) effects. Although the effects introduced by ISI may be partially neglected due to the use of spreading, the dispersed energy cannot be completely recovered by the correlator receiver. Finally, it must be emphasized that the level of dispersion increases with the signal bandwidth. Thus, the performance will degrade as more spreading is used. This is also observed in Figure 5.8.

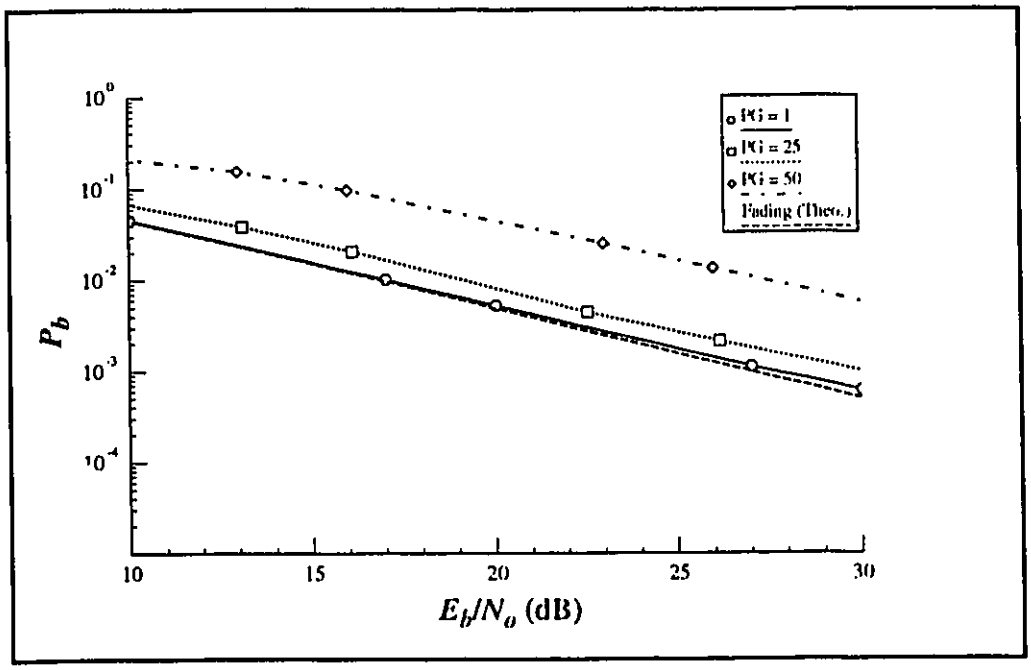

FIGURE 5.8. P_b vs E_b/N_o for the Equatorial Link and the Correlator Receiver

Polar Link

The performance obtained with the correlator receiver under the simulated polar link is shown in Figure 5.9. In this case where three independent skywave returns are present, the benefit of spreading as a means to combat multipath fading can be appreciated. Although performance improves when spreading is used, it may be observed that the use of spreading alone is not sufficient to eliminate the irreducible error rate common to multipath channels. Moreover, it may be noticed that once the level of spreading is sufficient to discriminate between the different returns, further increase of the processing gain does not help to improve performance. Indeed, performance degrades due to the increasing delay dispersion.

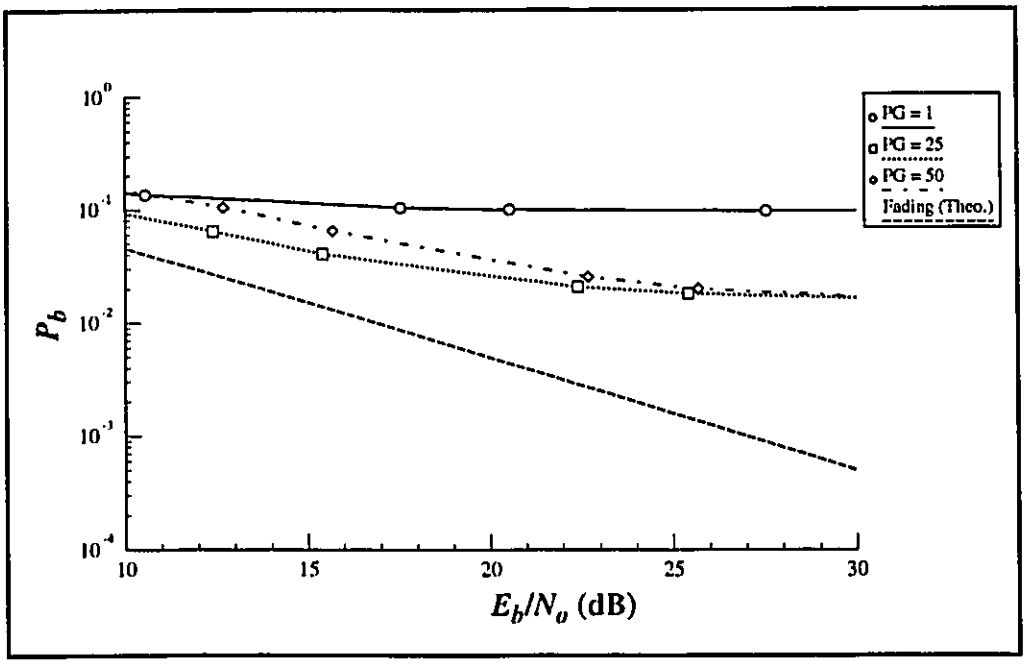

FIGURE 5.9. P_b vs E_b/N_o for the Polar Link and the Correlator Receiver

Auroral Link

The performance obtained with the simulation of the auroral link is shown in Figure 5.10. In the case of no spreading, the differential delay between each return is less than one bit period so that the received signal is nearly seen by the receiver as a single return. Thus, most of the transmitted energy may be recovered at the receiver; explaining why the performance is close to the theoretical flat-fading channel performance. However, it may be noted that the curve slightly levels off as E_b/N_o increases due to the effect of multipath.

In the case of spreading, performance similar to that of the equatorial link simulation may be observed; i.e.,the effects of increasing the processing gain leads to poorer performance. Moreover, the effect of the multiple returns are noticed by bit error rate levelling due to the presence of irreducible errors.

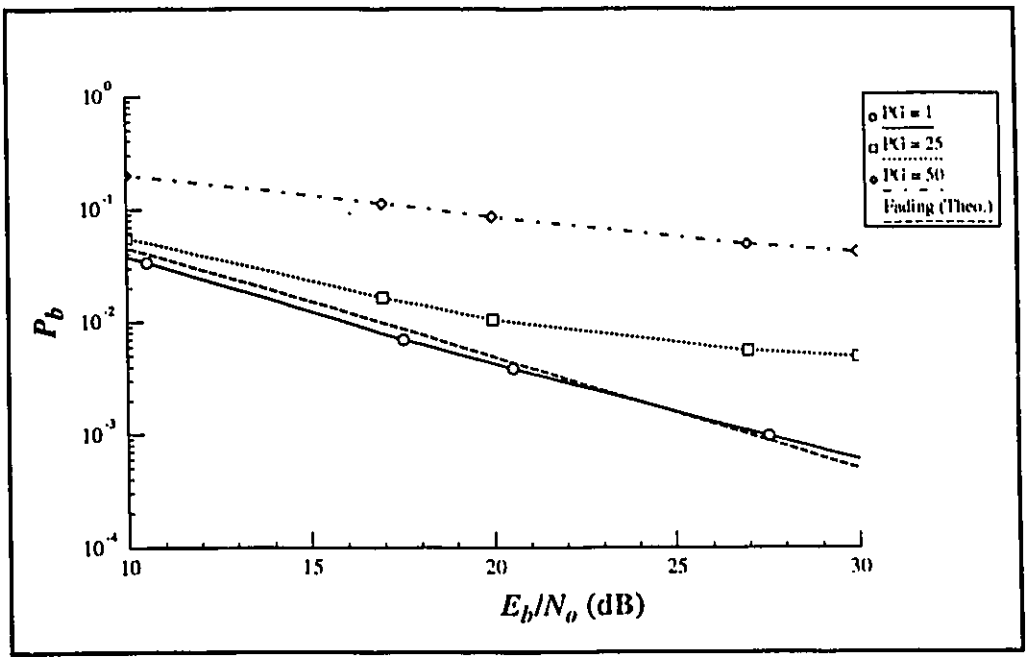

FIGURE 5.10. P_b **vs** E_b/N_o **for the Auroral Link and the Correlator Receiver**

5.5 RAKE Receiver Performance

From the results obtained with the correlator receiver, it may be concluded that more powerful techniques are needed to mitigate the effects of the delay and frequency dispersion. In this section, the performance of the RAKE receiver presented in Figure 4.13 is estimated for the three selected channels. The effects of increasing the number of taps of the RAKE receiver is first evaluated for different spreading bandwidths corresponding to processing gains of 1, 25, and 50. The resulting curves show the relationship between the bit error probability P_b as a function of the number of taps for different levels of E_b/N_o. Then, the P_b vs E_b/N_o performance obtained for different RAKE receiver implementations is analyzed.

Equatorial Link

Figures 5.11 and 5.12 show the performance obtained for different SNR's as a function of the number of taps in the RAKE receiver in the case of an equatorial link. In Figure 5.11, a spreading bandwidth of 72 kHz, corresponding to a processing gain of 25, is used to define the width of the delay dispersion. It may be observed that the delay disper-

sion, which amounts to only three times the chip period T_c, is not sufficient to completely decorrelate the signal components processed in the taps. This results in same performance even when the number of taps is increased.

In Figure 5.12, it may be seen that tap signal decorrelation is achieved to some extent when the delay dispersion introduced by the channel has doubled in terms of the chip duration. This is done by raising the processing gain to 50; thereby doubling the channel bandwidth used. Decorrelation may be assumed by the noticeable performance change obtained when the number of taps is increased from 1 to about 50. Thereafter, performance levels off. This may be explained by the fact that the signal energy being dispersed in the additional taps become small compared to the noise level. The effect of those taps is therefore equivalent to reducing the E_b/N_o ratio by introducing additional noise components.

Based on the result obtained in Figure 5.11 where the performance resulting from a processing gain of 25 was shown to be independent of the number of taps, it was decided not to investigate further the bit error probability vs E_b/N_o performance of the equatorial link with a processing gain of 25. The results are shown in Figure 5.13, where the performance obtained from a 1-tap, 10-tap, and 25-tap RAKE receiver with a processing gain of 50 are compared. As expected, better performance is achieved as the number of taps is increased.

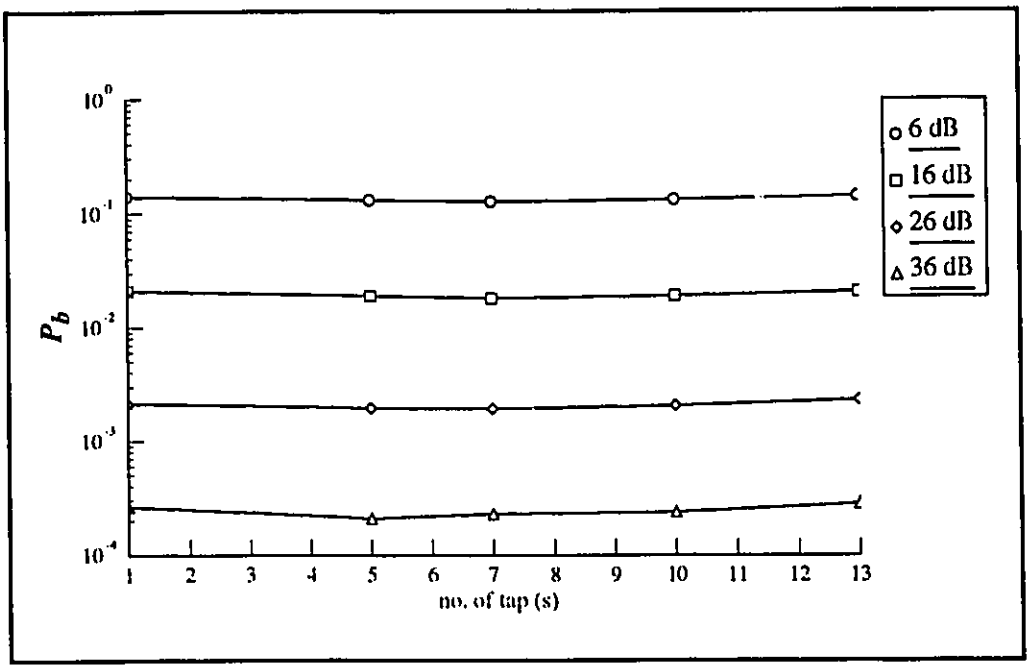

FIGURE 5.11. P_b vs No. of Taps for the Equatorial Link and Processing Gain of 25

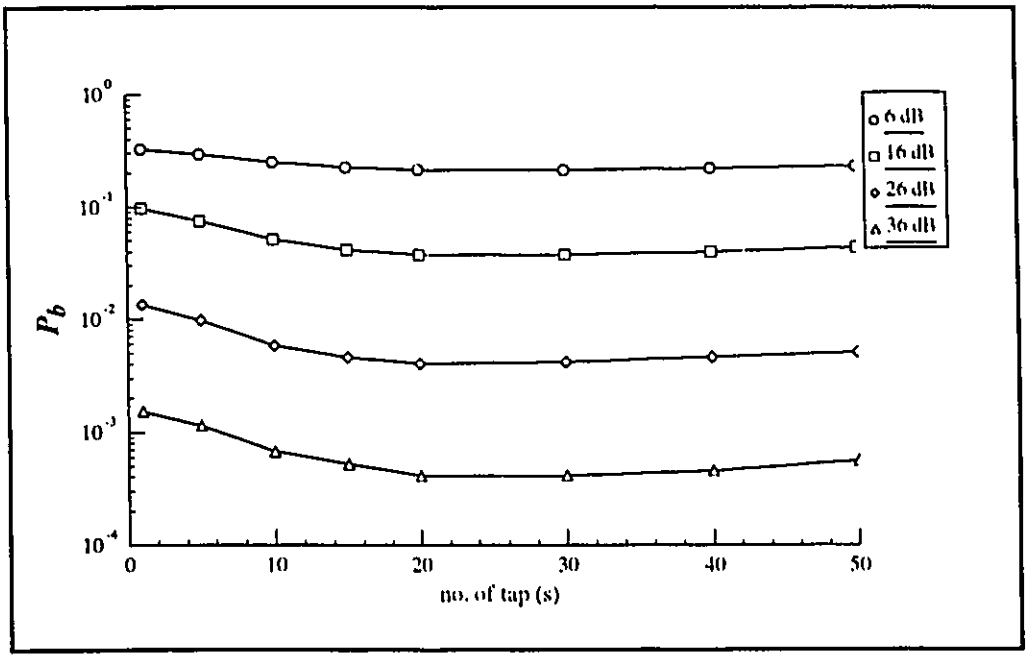

FIGURE 5.12. P_b **vs No. of Taps for the Equatorial Link and Processing Gain of 50**

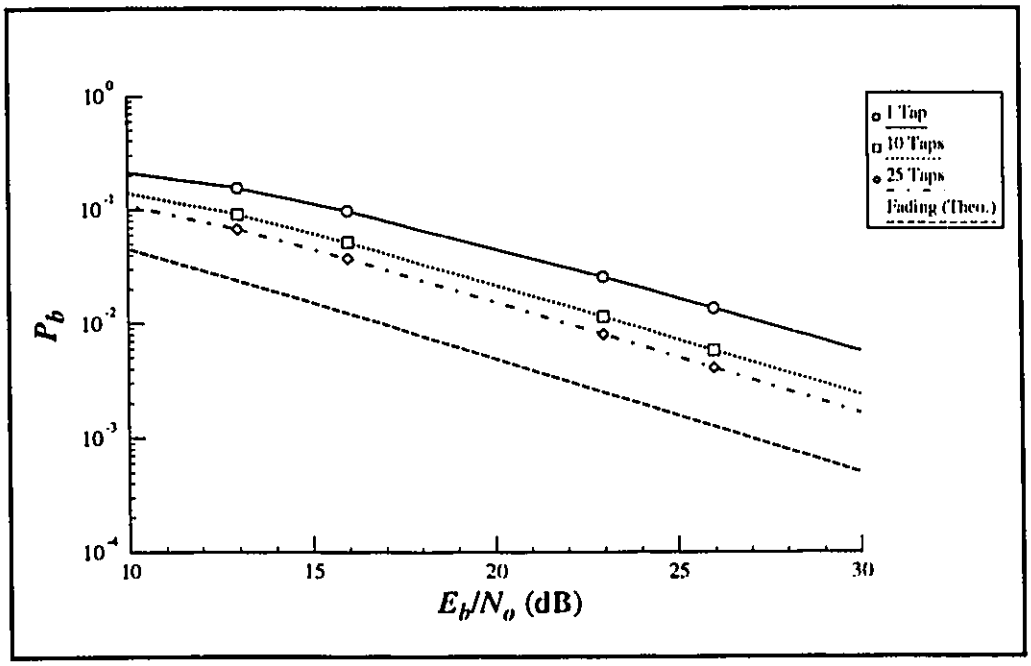

FIGURE 5.13. P_b **vs** E_b/N_o **for the Equatorial Link and Processing Gain of 50**

Polar Link

Figures 5.14 to 5.18 show the RAKE receiver performance obtained for the polar link. While Figures 5.14, 5.15, and 5.16 show performance as a function of the number of taps in the RAKE receiver, Figures 5.17 and 5.18 provide P_b vs E_b/N_o for a selected number of taps.

In Figure 5.14, no spreading is performed and the number of taps in the RAKE receiver is limited to three, the number of skywave returns. The absence of performance improvement may be explained by the fact that the received signal is dominated by the energy returned from the low-ray F layer (see α in Table 5.1). In Figure 5.15, the benefit of a RAKE receiver against the effects of multiple independent returns may be appreciated. Once again it may be noticed that the bit error rate reaches an irreducible floor after about 10 taps.

It is interesting to note that the performance does not improve monotonically; this can be observed in Figure 5.16 where a channel bandwidth corresponding to a processing gain of 50 is used. To explain this performance behavior, it must be recalled that the tap-delay line contains both independent and highly correlated signal components. While the former originates from different skywave returns, the latter originates from the same return. If the number of taps is sufficiently small so that only the components originating from the same return are processed, then performance becomes independent from the number of taps: this phenomenon is identical to the one observed for the equatorial path whose performance was shown in Figure 5.11. In the present case, however, performance starts to improve as the number of taps increases (i.e., beyond 10 in Figure 5.16). The RAKE receivers can then process the uncorrelated signal components originating from both the low and high rays of the F-layer. A second plateau results when the receiver tries to process a number of signal components all originating from the high ray. By further increasing the number of taps, performance starts to improve again. Although not shown in Figure 5.16, it is expected that a third plateau will occur when adjacent[1] components from the first return are processed.

The advantage of using a large number of taps in a RAKE receiver is to reduce the irreducible bit error rate as shown in Figures 5.17 and 5.18. It may also be observed, particularly in Figure 5.17, that a relatively small number of taps may lead to significant performance improvement as long as the delay dispersion in the different returns is not too large.

1. Adjacent components are those that are separated by only one sample period T_s.

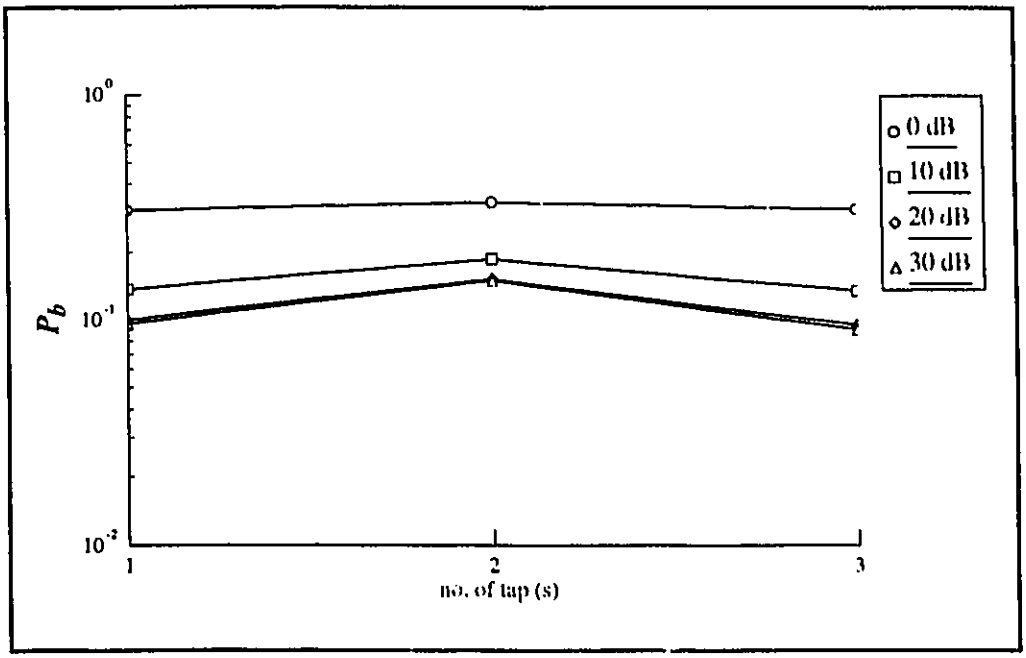

FIGURE 5.14. P_b **vs No. of Taps for the Polar Link and no Processing Gain**

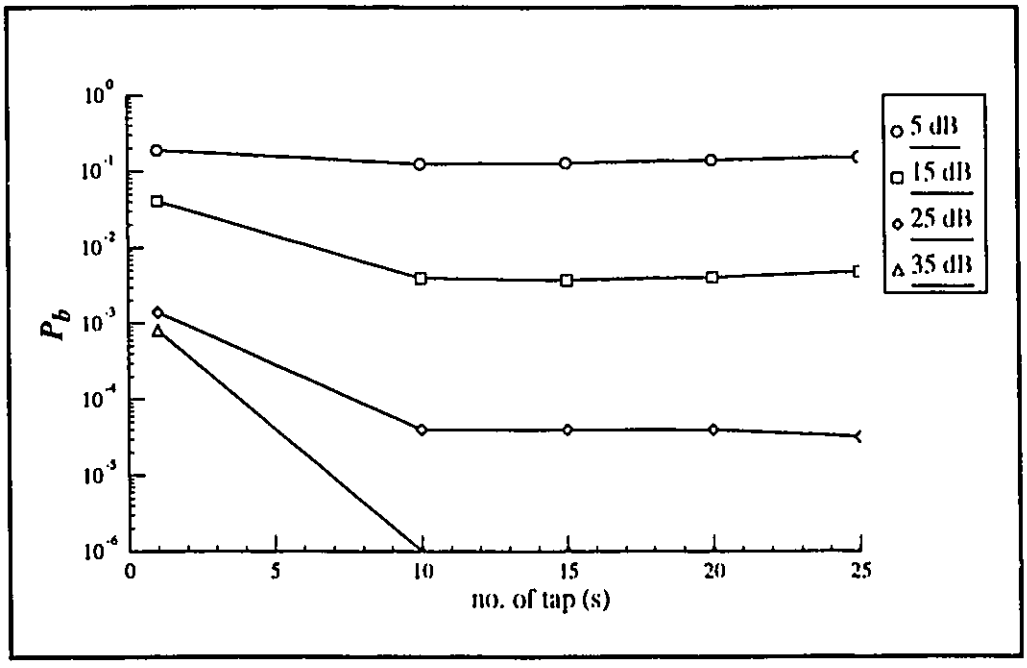

FIGURE 5.15. P_b **vs No. of Taps for the Polar Link and Processing Gain of 25**

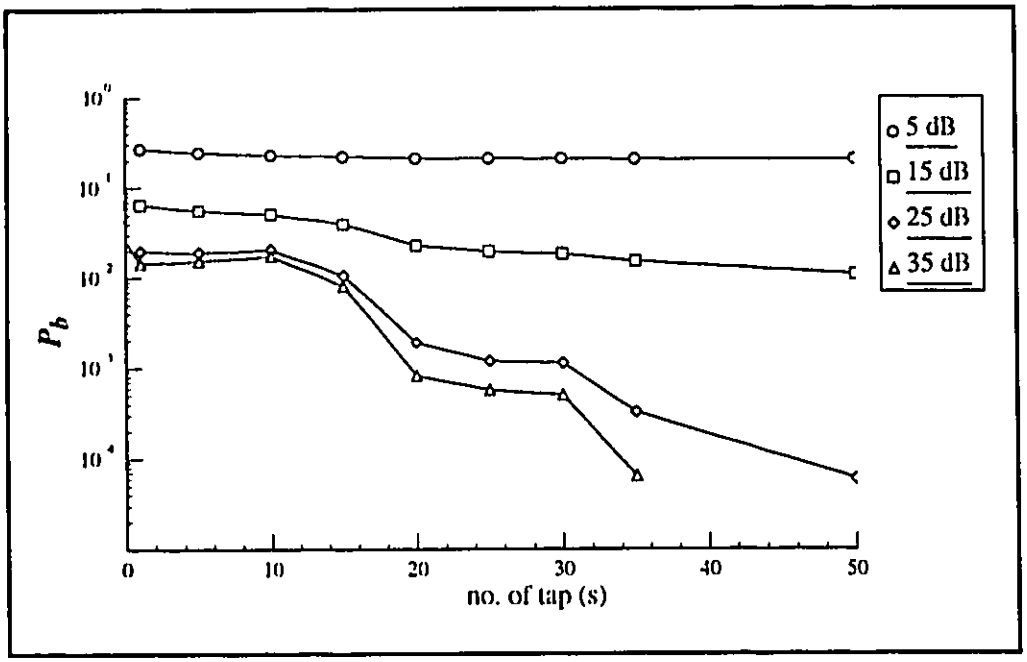

FIGURE 5.16. P_b **vs No. of Taps for the Polar Link and Processing Gain of 50**

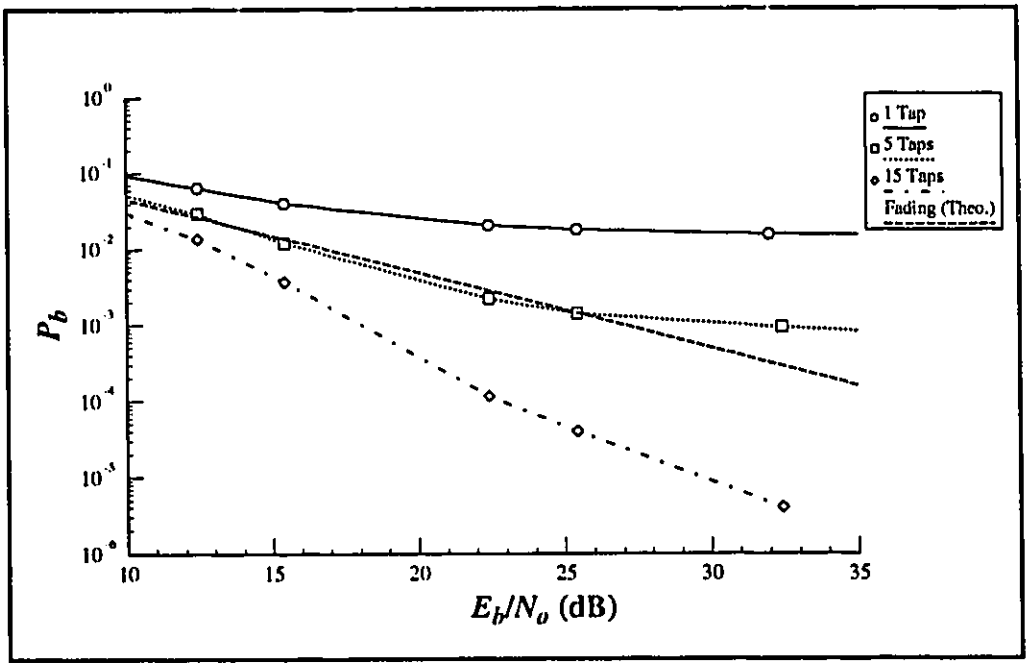

FIGURE 5.17. P_b **vs** E_b/N_o **for the Polar Link and Processing Gain of 25**

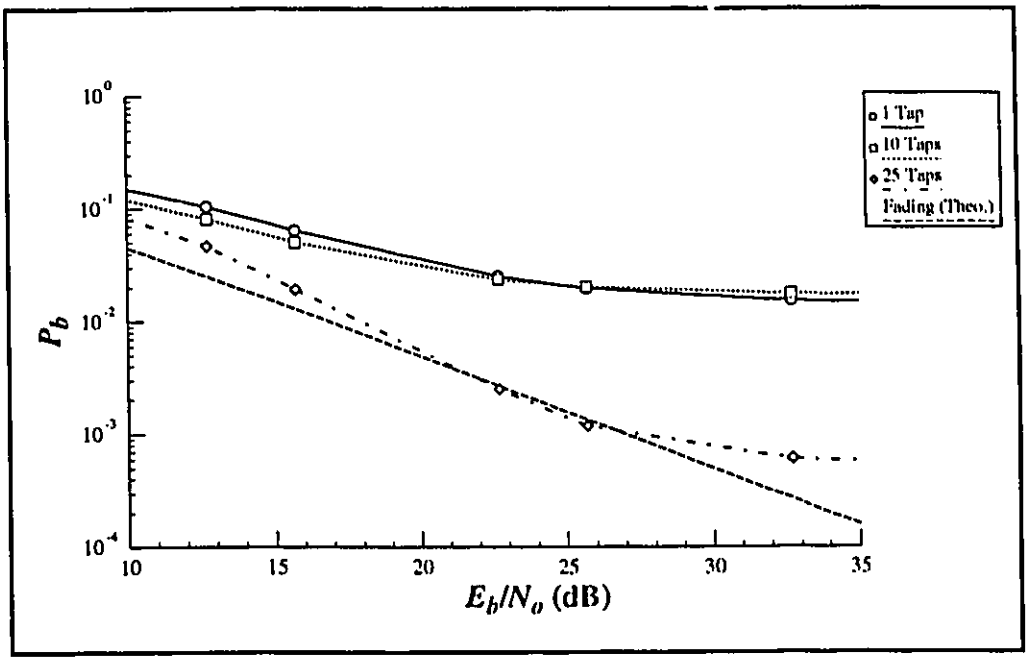

FIGURE 5.18. P_b vs E_b/N_o for the Polar Link and Processing Gain of 50

Auroral Link

The performance results obtained by simulating the auroral link are shown in Figures 5.19 to 5.22. Improvement achieved by increasing the number of taps in the RAKE receiver is shown in Figures 5.19 and 5.20 whereas detailed comparison of the RAKE receiver performance at different processing gain settings follow in Figures 5.21 and 5.22.

As mentioned earlier, the simulated auroral link without spreading consists of four nearly overlapping returns spread over less than on bit interval T_b. Thus, the RAKE receiver is limited to a one-tap implementation and performance similar to those of the correlator receiver are obtained (compare Figures 5.10, 5.19, and 5.20). If the bandwidth is increased by a factor of 25 or 50, the returns may then be discriminated into a pair of two nearly overlapping returns. Figures 5.19 and 5.20 show the advantage provided by a multi-tap RAKE receiver. Because of the small delay dispersion of each return, significant improvement is achieved even for a small number of taps (4 or more in Figure 5.20) implementation.

Figures 5.21 and 5.22 show the performance in terms of P_b vs E_b/N_o for processing gains of 25 and 50 respectively. Once again it may be observed that increasing the processing gain does not necessarily ensure better performance. In fact, as for the correlator receiver, when the minimum bandwidth required to discriminate between distinguish-

able returns is reached, no further gain is obtained by increasing the processing gain, indeed, performance degrades.

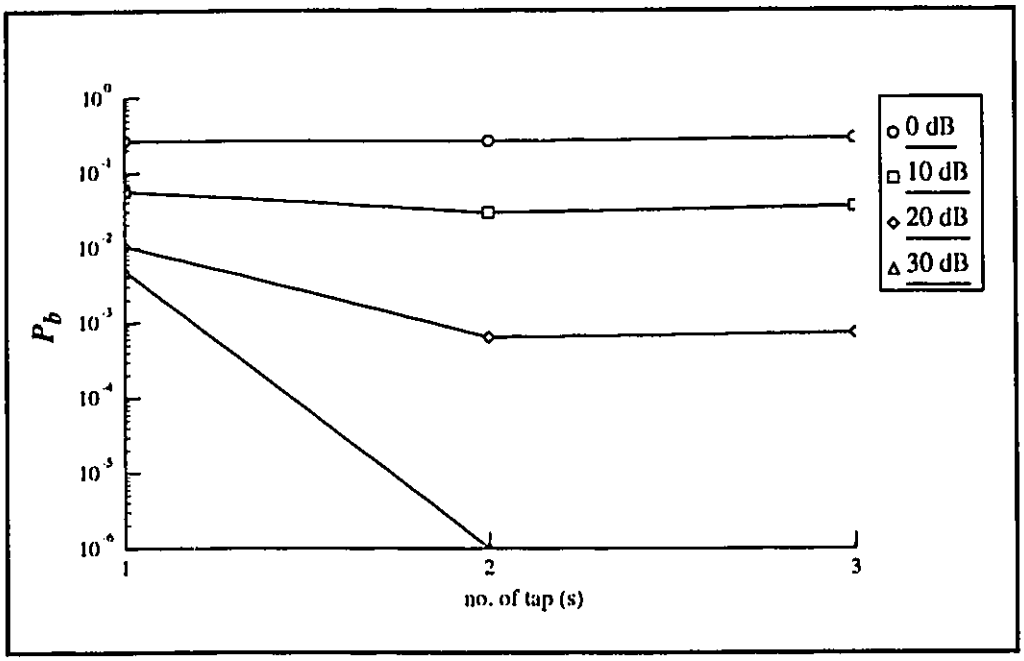

FIGURE 5.19. P_b **vs No. of Taps for the Auroral Link and Processing Gain of 25**

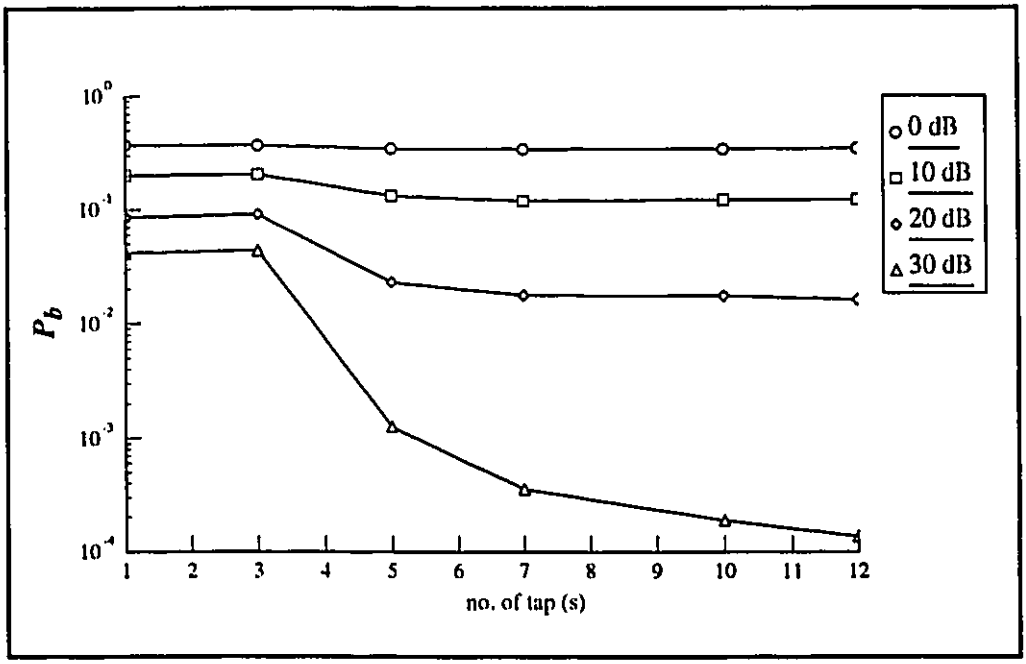

FIGURE 5.20. P_b **vs No. of Taps for the Auroral Link and Processing Gain of 50**

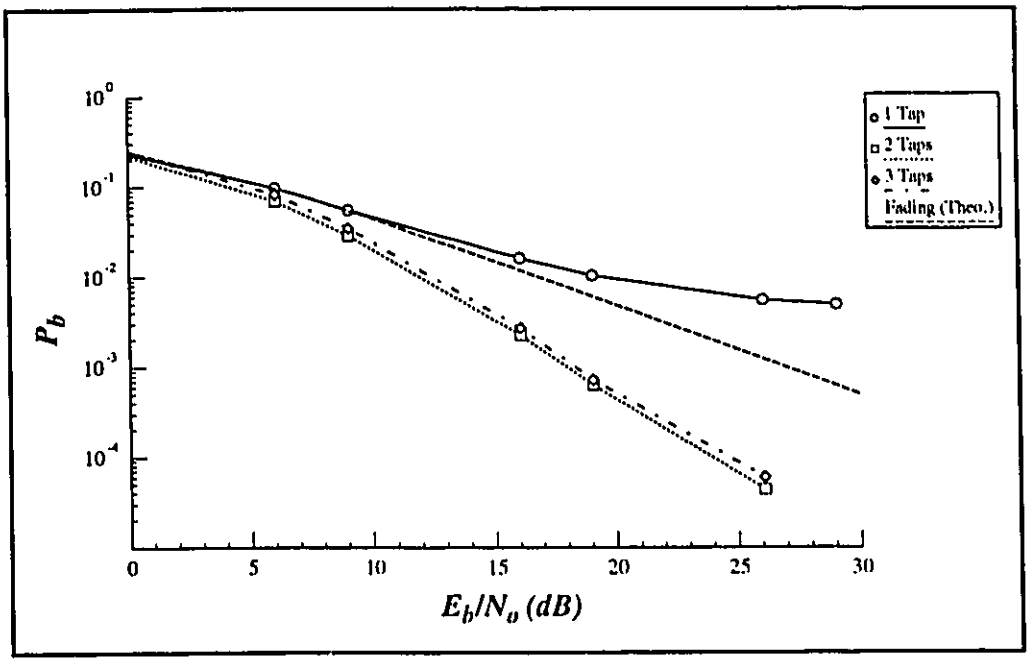

FIGURE 5.21. P_b vs E_b/N_o for the Auroral Link and Processing Gain of 25

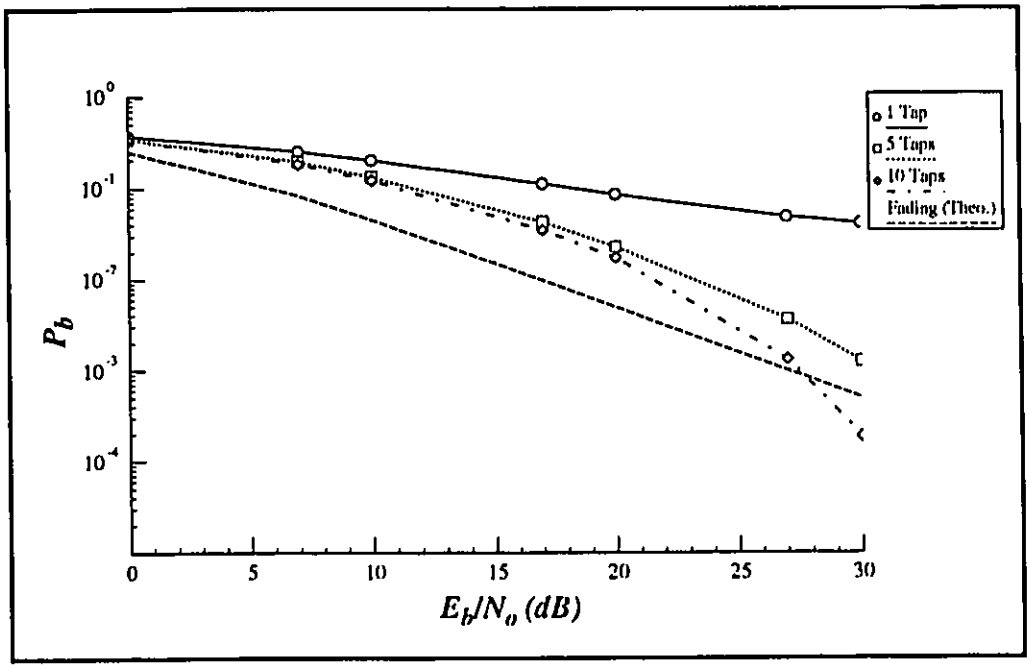

FIGURE 5.22. P_b vs E_b/N_o for the Auroral Link and Processing Gain of 50

5.5.1 Performances With Coding

Based on the previous results, bit error rate performance has been estimated for the different RAKE receiver configurations along with error control coding and interleaving. Simulations have been conducted over a fixed bandwidth equivalent to 50 time the bit rate R_b (PG = 50); i.e 144 kHz. The number of taps in the RAKE receiver was selected based on the results obtained in the previous section. More specifically, a number of taps corresponding to a performance better than 10^{-2} was chosen so that a 10-tap receiver for the equatorial link, a 25-tap receiver for the polar link, and a 5-tap receiver for the auroral link were implemented. Error rate performance has been estimated for an 11-error (63,41) RS code (coding rate ≈ 0.49) and a 16-error (63,31) RS code (coding rate ≈ 0.65) with hard-decision decoding. In addition, performance has also been obtained for a rate 1/2 constraint length 7 convolutional code (R1/2C7) with and without interleaving. In this case, soft-decision decoding was implemented.

Equatorial Link

In the case of the equatorial link, it may be seen in Figure 5.23 that Reed-Solomon codes with hard-decision decoding provide a better performance than does convolutional code with soft-decision decoding. This is expected since RS coding is known for its robustness against error-burst channels. Better performance obtained from the RS code having a higher error correcting capability (RS(63, 31)) may also be noticed. A 15-dB gain achieved at $P_b \approx 10^{-4}$ through the use of a R1/2C7 convolutional code with interleaving compared to the 16-error (63,31) RS code is remarkable, and is indicative of the strong error-burst characteristic of this channel.

Polar Link

Coding performance over the polar link is shown in Figure 5.24. As it can be observed, the advantage of using a block code having a high error-correcting capability is lost when the delay dispersion within the channel is large. This may be explained by the fact that the energy in the coded symbols decreases as does the code rate. The figure shows that at E_b/N_o of 18 dB or higher the convolutional code still provides poorer performance than the RS codes. Once again the strong advantage of using interleaving is clear and translates into a 5-dB gain improvement over the performance achieved by the RS code at a bit error rate around 10^{-4}.

Auroral Link

The performance achieved under the simulated auroral link conditions is shown in Figure 5.25. RS coding still performs better than convolutional coding. However, it is interesting to note that a higher E_b/N_o is required for the auroral link before noticing any

significant coding gain; more specifically about 30 dB is required, whereas an SNR in the order of 20 dB and 10 dB were required for the equatorial link and the polar link respectively. Again by interleaving, a coding gain of 20 dB is achieved at a BER $\approx 10^{-4}$ over the 11-error (63,41) RS code.

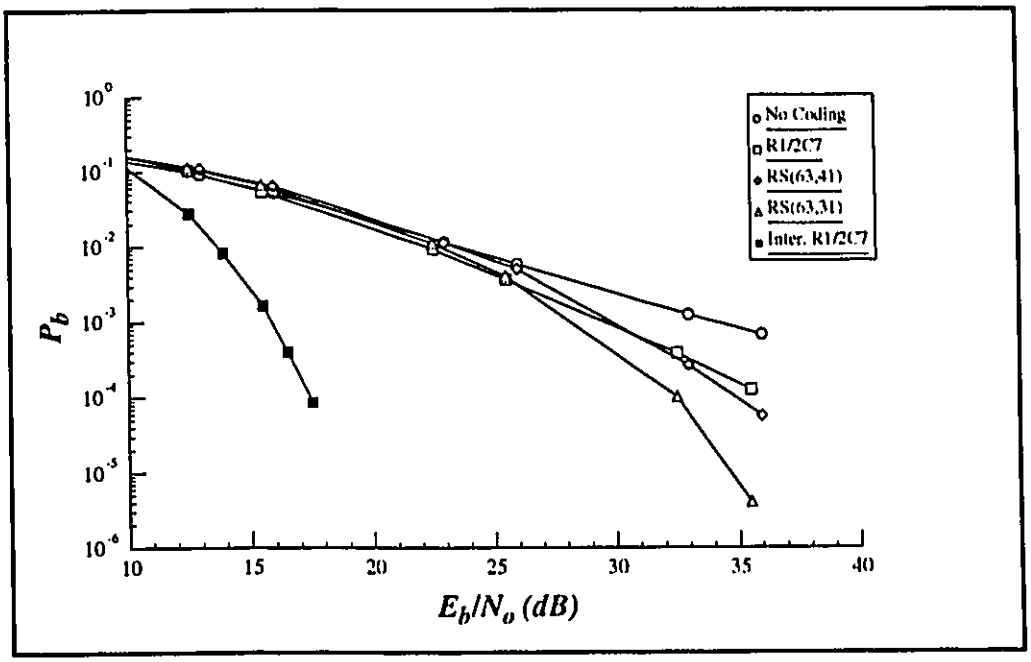

FIGURE 5.23. Coding Performance for the Equatorial Link and a 10-Tap DPSK RAKE Receiver

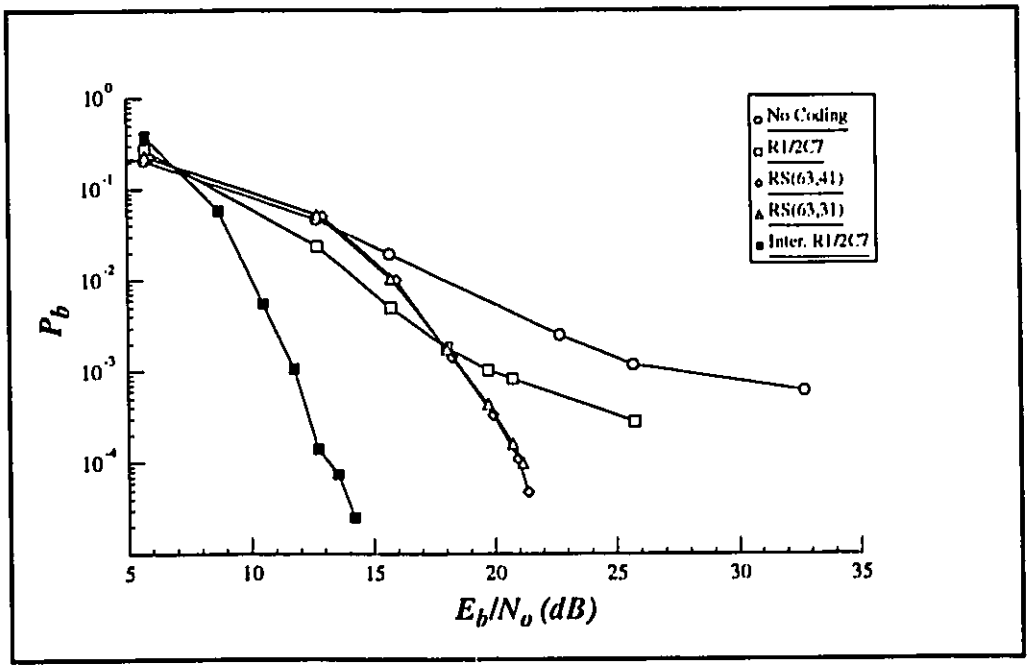

FIGURE 5.24. Coding Performance for the Polar Link and a 25-Tap DPSK RAKE Receiver

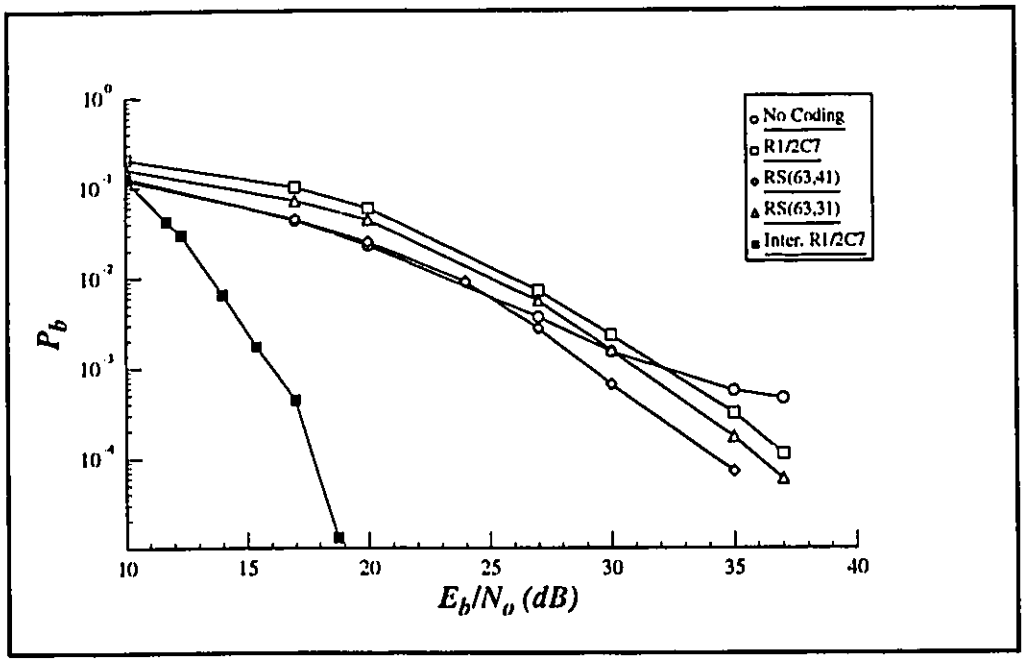

FIGURE 5.25. Coding Performance for the Auroral Link and a 5-Tap RAKE Receiver

5.6 Conclusion

In this chapter, the IPM model is used to characterize selected equatorial, polar, and auroral links with the help of ionograms and scattering functions. The performance obtained from the simulation of a wideband HF communication system operating over these channels is then presented. Although it would be necessary to vary a single channel parameter at a time to perform a thorough evaluation of the system, the simulation results presented in this chapter provide an interesting insight into the advantages of using of direct sequence spread spectrum techniques over different types of wideband HF channel conditions.

Chapter 6
Conclusions and Suggestions for Further Research

6.1 Thesis Summary

The revived interest in the use of the HF channel over the last few years has increased the demand for more efficient and more powerful HF communication systems. One possible approach to improve these systems is to use wideband signalling. In this thesis, performance obtained from a simulated wideband HF system has been studied. More specifically, direct sequence spread spectrum (DSSS) has been investigated over different wideband channel conditions in order to assess its impact on the system performance.

The difficulty of evaluating performance of communication systems over wideband HF channels has been overcome by performing computer simulations of a wideband channel model referred to as the Ionospheric Parameter Model. Although this model offers the possibility to simulate a wide variety of conditions, we restricted our work to three sets of channel parameters, each representative of ionospheric conditions observed at equatorial, polar and auroral latitudes.

The analysis began by considering a simple DSSS correlator receiver. From the results obtained, it is observed that increasing the processing gain, and thereby the signal bandwidth, does not necessarily ensure better performance. Because channel delay dispersion increases as the channel bandwidth becomes wider, the receiver input signal energy disperses as the processing gain is raised. The performance degradation caused by increasing processing gain becomes more acute when the channel consists of one single path. In this case, better performance is obtained from the non-spread signal. Moreover, simulation of the correlator receiver showed that in the case of a multipath channel, a processing gain just sufficient to discriminate between the different skywave returns lead to the best performance. This is particularly interesting in the case where a compromise between transmission rate and processing gain is possible. One would choose to increase the transmission rate whenever a low processing gain is adequate to discriminate between the different returns.

The effects of delay dispersion on the performance of the correlator receiver demonstrated the necessity of implementing a receiver that tries to recover most of the transmitted energy. This conclusion led to the evaluation of a RAKE receiver. In these simulations, it was assumed that the differential delay of each return was known perfectly and that the taps of the receiver were always synchronized to the returns presenting the

lower attenuation level. In general, results showed that performance with the RAKE receiver was improved. In addition to this, results reveal a number of interesting observations. In the case of a single-path wideband channel, performance was shown to be independent from the number of receiver taps but for delay dispersion sufficiently large to decorrelate the different received signal components. It was also noticed that performance over a multipath channel with a multi-tap receiver does not display a monotonic behavior. It is characterized by a succession of "plateaux", each of them attributed to the strong correlation existing within each path. Thus, it is important not to confine the tap selection to one criterion like their average power but also to other parameters such as the correlation level of the different signal components processed by adjacent taps. This would ensure to take full advantage of the channel multipath diversity without unduly increasing the receiver complexity.

Finally, the thesis was concluded by evaluating different coding techniques. Although Reed-Solomon coding provided the best coding gain for all type of channels, it was observed that a code having a stronger error-correcting capability does not necessarily provide better performance. This was particularly true for the cases where large delay dispersion or where disturbed ionospheric conditions were simulated. It was also shown that the use of interleaving with coding far exceeds the performance of any of the codes without interleaving. Thus, it was concluded that interleaving is a necessity over wideband HF channel as long as the introduced interleaving delay may be tolerated.

6.2 Suggestions for Further Research

In this thesis we have limited the performance evaluation to the case where perfect synchronization was assumed. The results must therefore be interpreted as upper bounds. To obtain more realistic results it would be necessary that simulations be performed with a block synchronizer. This is particularly important in the case of spread spectrum since the problem of acquiring and maintaining synchronization to a fraction of the chip period is extremely difficult even in the absence of multipath.

A number of further researches can also be conducted to extend the result presented in this thesis to a larger number of wideband channel conditions. As stated in [Vogl90], an exponential distribution for the correlator factor of the IPM model is more representative of the real channel conditions. It would therefore be appropriate to evaluate how this change affects the performance. Also, it is important to recall that the channel was limited to AWGN conditions even though it is well recognized that the HF channel is corrupted by all sorts of strong interference signals. Moreover, because wide bandwidth receivers accept more interfering power, it would be interesting to quantify the performance under a wideband noise model such as the one presented in Chapter 2.

Finally, this thesis concentrated on evaluating the performance of a communication system using DPSK modulation and transmitting at a rate of 2400 bits per second. Further research could certainly be undertaken for determining the performance obtained with higher transmission rates and different modulation and coding schemes and for comparing bit-error-rate results with adaptive channel equalization techniques.

Appendix A
The Refractive Index of the Ionosphere

This annex provides a summary of the derivation of the refractive index for the ionosphere. The derivation mainly follows the one presented by Budden [Budd61].

A.1 Maxwell's Equations

When a radio wave enters the ionosphere, the electro-magnetic field that is created may be expressed as:

$$F = A_0 e^{j(\omega t + \phi_0)} \tag{A-1}$$

where:

- $\omega = 2\pi f$ = angular wave-frequency,
- f = wave frequency,
- A_0 = real constant, and
- ϕ_0 = phase constant.

If it is assumed that the dependence of the field upon the wave normal is only through a factor $\exp(-jk\eta r)$ where

- $k = \omega/c = 2\pi/\lambda$,
- c = velocity of light in free space,
- λ = wave length in free space, and
- η= refractive index;

then the wave is referred to as a progressive plane wave and it shows general features that follow the Maxwell's equations:

$$\nabla \times \boldsymbol{E} = -j\omega\mu_0 \boldsymbol{H} \tag{A-2a}$$

$$\nabla \times \boldsymbol{H} = j\omega \boldsymbol{D} \tag{A-2b}$$

$$\nabla \cdot \boldsymbol{D} = 0 \tag{A-2c}$$

$$\nabla \cdot \boldsymbol{H} = 0 \tag{A-2d}$$

where $\boldsymbol{E}$, $\boldsymbol{H}$, $\boldsymbol{D}$, and $\boldsymbol{B}$ are vectorial quantities describing the electric intensity, the magnetic intensity, the electric displacement, and the magnetic induction respectively. The electric displacement is defined as:

$$\boldsymbol{D} = \varepsilon_0 \boldsymbol{E} + \boldsymbol{P} \tag{A-3}$$

with

$$\boldsymbol{P} = N_e e \boldsymbol{r} \tag{A-4}$$

where

- $\boldsymbol{P}$ is the electric polarization,
- N_e is the electron density,
- e is the electron charge, and
- $\boldsymbol{r}$ is the average position that the electron would have occupied if there was no field.

Following the assumption that the radio wave entering the ionosphere is a progressive plane wave for which $\partial/\partial x = \partial/\partial y = 0$ and $\partial/(\partial z) = -jk\eta$, it is possible to rewrite (A-2) as:

$$k\eta E_y = -\omega\mu_0 H_x \tag{A-5a}$$

$$k\eta E_x = -\omega\mu_0 H_y \tag{A-5b}$$

$$0 = H_z \tag{A-5c}$$

$$k\eta H_y = \omega D_x \tag{A-6a}$$

$$k\eta H_x = -\omega D_y \tag{A-6b}$$

$$0 = D_z, \tag{A-6c}$$

in order to express the refractive index as a function of the electric displacement and the electric intensity. By isolating H_x in (A-5a) and substituting it in (A-6b), or isolating H_y in (A-5b) and moving it into (A-6a), η may be defined as:

$$\eta^2 = \frac{D_x}{\varepsilon_0 E_x} = \frac{D_y}{\varepsilon_0 E_y} \tag{A-7}$$

where

$$\varepsilon_0 = \frac{1}{\mu_0 c^2} \tag{A-8}$$

The solutions of the Maxwell's equations for determining the refractive index are however incomplete since they do not consider the specificities of the dynamic processes introduced by the earth's magnetic field and the effects of the sun on the ionosphere. It is therefore required to introduce the "so-called" constitutive equations of the medium to obtain a more complete definition of the refractive index.

A.2 Constitutive Equations

Using the Newton's laws, the dynamic of an electron in the ionosphere depends upon the presence of the electric field, $\boldsymbol{E}$, the earth's magnetic induction, $\boldsymbol{B}_0$, and the presence of collisions, ν, between the air molecules and the free electrons. The equation of average motion of an electron may then be written as:

$$m\frac{\partial^2 \boldsymbol{r}}{\partial t^2} = e\boldsymbol{E} + e\frac{\partial \boldsymbol{r}}{\partial t} \times \boldsymbol{B}_0 - m\upsilon\frac{\partial \boldsymbol{r}}{\partial t}; \tag{A-9}$$

where m is the mass of an electron.

Equation A-9 may be rewritten in complex notation as

$$-\varepsilon_0 X\boldsymbol{E} = \boldsymbol{P}(1 - jZ) + j\boldsymbol{P} \times \boldsymbol{Y} \tag{A-10}$$

with:

$$X = \frac{N_e e^2}{\varepsilon_0 m\omega^2} = \frac{\omega_N^2}{\omega^2}, \tag{A-11}$$

$$\upsilon Y = \frac{eB_0}{m\omega} = \frac{\omega_H}{\omega}, \text{ and} \tag{A-12}$$

$$Z = \frac{\upsilon}{\omega}; \tag{A-13}$$

where

- ω_N is the angular plasma frequency defined as:

$$\omega_N^2 = \frac{N_e e^2}{\varepsilon_0 m}; \text{ and} \tag{A-14}$$

- ω_H is the angular gyro-frequency defined as:

$$\omega_H = \left| \frac{eB_0}{m} \right|. \tag{A-15}$$

The gyro-frequency may be seen as the frequency at which a free electron subjected to a magnetic field completes a turn of an helical path.

Equation A-10 written in a matrix form provides the required relations to find the expression for the refractive index in its most general form; i.e, the medium is considered anisotropic (the earth's magnetic field is considered) and dissipative (collisions between free electrons and air molecules are not neglected):

$$-\varepsilon_0 X \begin{pmatrix} E_x \\ E_y \\ E_z \end{pmatrix} = \begin{pmatrix} 1-jZ & jl_3Y & -jl_2Y \\ -jl_3Y & 1-jZ & jl_1Y \\ jl_2Y & -jl_1Y & 1-jZ \end{pmatrix} \begin{pmatrix} P_x \\ P_y \\ P_z \end{pmatrix}; \tag{A-16}$$

where l_1,l_2, and l_3 are the direction cosines of the vector Y.

A.3 Appleton-Hartree Equations

With appropriate manipulations of (A-5), (A-6), and (A-16), a general expression of the refractive index is derived. This expression, known as the Appleton-Hartree formula, may be expressed as:

$$\eta^2 = 1 - \frac{X}{1 - iZ - \frac{\frac{1}{2}Y_T^2}{1 - X - jZ} \pm \sqrt{\frac{\frac{1}{4}Y_T^4}{(1 - X - jZ)^2} + Y_L^2}} \tag{A-17}$$

where

- Y_T is the transverse component of Y; i.e. the wavefront normal is parallel to the earth's magnetic field, and
- Y_L is the longitudinal component of Y; i.e. the wavefront normal is perpendicular to the earth's magnetic field.

A complete discussion of the above expression is beyond the scope of this work; but, it is interesting to look at the case which falls under the same assumptions made for the derivation of the channel model used for the simulations. Because we are more interested in the upper layer of the ionosphere, namely the F_2 layer, to achieve long-range communications links, it is generally accepted that collision frequency may be neglected; i.e., Z may be approximated to zero. Equation A-17 may then be written as:

$$\eta^2 = 1 - \frac{X}{1 - \frac{\frac{1}{2}Y_T^2}{1-X} \pm \sqrt{\frac{\frac{1}{4}Y_T^4}{(1-X)^2} + Y_L^2}} \qquad \text{(A-18)}$$

where the refraction index can take on two values depending on the sign of the square-root. The value corresponding to the positive sign is referred to as the *ordinary* mode while the negative sign corresponds to the *extraordinary* mode. Figure A-1 shows an example of the variation of the refraction index in terms of variations of X for inclination between the front wave normal and the earth's magnetic filed ranging between 0 and $\pi/2$, and for $Y < 1$; i.e., for a transmission frequency greater than the gyro-frequency ω_H.

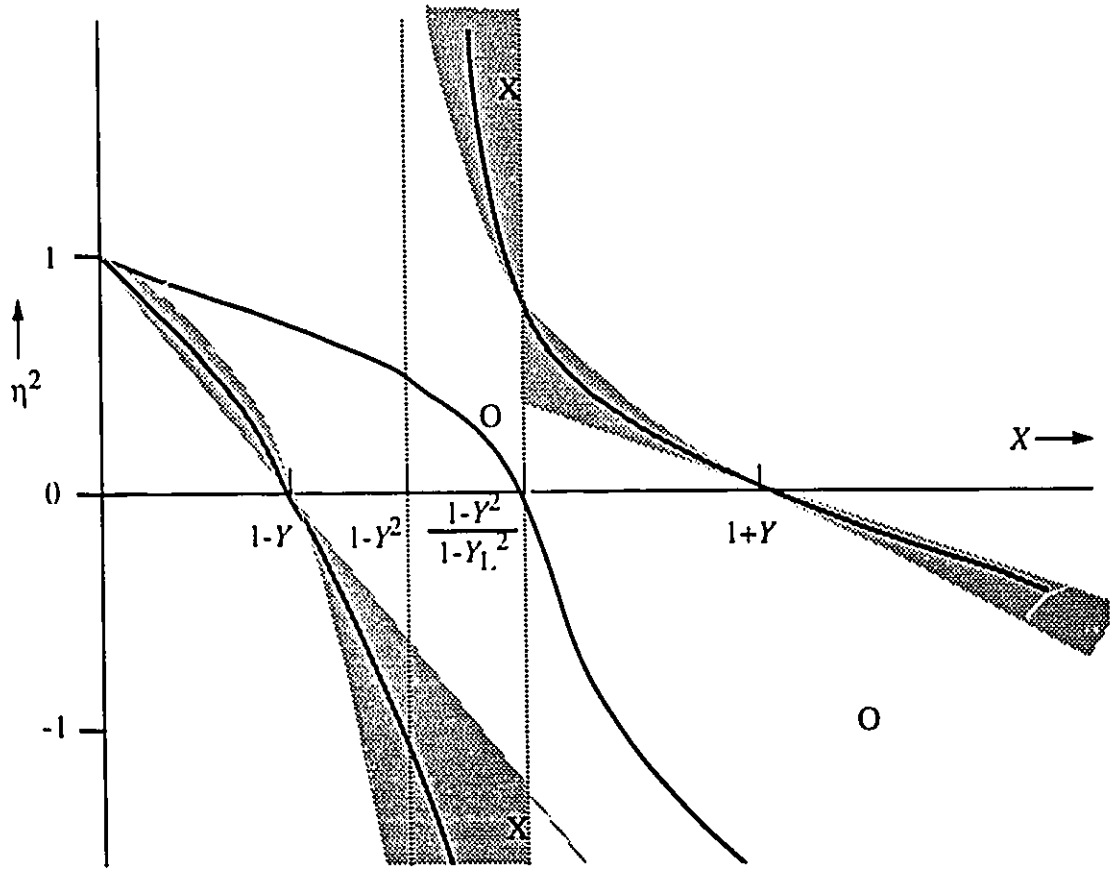

FIGURE A-1. Transition of Refractive Index Curves from Longitudinal to Transverse Propagation in the Case of $Y < 1$ and no Collision

Equation A-18 is still cumbersome to manipulate. For most communications applications, the earth's magnetic field can be neglected as in the case of the channel model used in this thesis. This assumption provides a simple expression where the refractive index is only a function of X:

$$\eta^2 = 1 - X = 1 - \left(\frac{f_N}{f}\right)^2 . \tag{A-19}$$

Appendix B
The Theorems of Breit and Tuve and Martyn

This Annex describes without proofs the theorems due to Breit and Tuve and Martyn regarding the ray geometry for reflection in the ionosphere. The complete proofs for each theorem may be found in [Kels64].

B.1 Theorem of Breit and Tuve

If we neglect the earth's magnetic field and the effects of collisions and considered the ionosphere as being horizontally stratified, the classical ray reflection geometry is shown in Figure B-1.

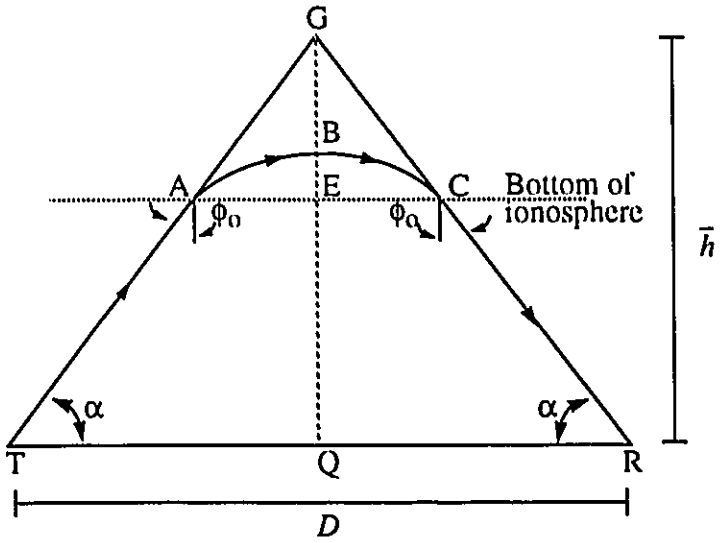

FIGURE B-1. Ray Geometry for Reflection in the Ionosphere

The path actually followed by the ray is the path *P'* defined by the segment $\overline{\text{TABCR}}$. However, for an observer at T or R, the ray transmitted at angle α appears to follow the segment $\overline{\text{TAGCR}}$. This latter segment is referred to as the apparent path and for the specified assumptions, the theorem of Breit and Tuve states that:

"The length of the apparent path is equal to the group path P'."

The theorem shows that we need to know only the ground range D between the two terminals; i.e the length of the segment $\overline{TR}$, and the angle of incidence ϕ_0 to determine the path length P'.

B.2 Martyn's Theorem

Keeping the same assumptions as for the theorem of Breit and Tuve; i.e. the ionosphere is horizontally stratified, and the collision frequency and the earths' magnetic field are negligible, the theorem due to Martyn establishes a simple relationship between the group path P' at vertical incidence ($\phi_0 = 0$) and oblique incidence. The theorem may be stated as:

"For a plane earth and plane ionosphere in the absence of collision and an external magnetic field, the apparent height of reflection for a vertical ray of frequency f_v equals that for an oblique ray of frequency $f = f_v \sec\phi_0$."

In simpler words, it may be said that both the vertical and the oblique rays are reflected at the apparent same height.

B.3 Applicability of the Theorems for the Ionospheric Parameter Model

The major difficulty in deriving a general expression for the path delay resides in the evaluation of the height at which reflection occurs for oblique incidences. However, since Martyn's theorem was derived under the same restrictions that have been assumed for the Ionospheric Parameter Model, the reflection height at oblique incidence is the same as for a wave transmitted at vertical incidence. Thus, the problem is that of determining the apparent reflection height at vertical incidence $\bar{h}_v$ as a function of the frequency f_v. This is done in Section 2.5.2 where it is shown that:

$$\bar{h}_v(f_v) = h_0 - \sigma \ln\left[\left(\frac{f_p}{f_v}\right) - 1\right]. \qquad \text{(B-1)}$$

Knowing the apparent height of reflection at vertical incidence and thereby the apparent height of reflection for oblique incidence $\bar{h}(f)$, it is now possible to determine the group path P' as a function of the frequency f using the theorem of Breit and Tuve:

$$\bar{h}(f) = \bar{h}_v(f_v) \quad \text{<-- Martyn's theorem; and} \qquad \text{(B-2)}$$

$$P'(f) = 2\sqrt{\bar{h}^2(f) + \left(\frac{D}{2}\right)^2} \quad \text{<-- theorem of Breit and Tuve.} \qquad \text{(B-3)}$$

where $f = f_v \sec\phi_0$ under the Secant law defined in Section 2.3.2.

Then, the median path delay $\tau(f)$ which is defined as the median time required by the ray to travel from the transmitter to the receiver, may be expressed as:

$$\tau(f) = \frac{P'(f)}{c}; \tag{B-4}$$

where c is the speed of light in free-space.

Finally, (B-4) may be rewritten to provide the relationship between the median path delay and the apparent height of reflection:

$$\tau_n(f) = \frac{2\bar{h}(f)}{c}\sqrt{1 + \left(\frac{D}{2\bar{h}(f)}\right)^2}. \tag{B-5}$$

Appendix C
IIR Filter For Rayleigh Fading Generator

The 2-pole Butterworth low-pass filter used in the simulation has a Laplace transform given by:

$$H(s) = \frac{A^2}{(s+A)^2}. \tag{C.1}$$

The filter parameter A is related to the 3-dB bandwidth by the relation

$$|H(j\omega_c)|^2 = \frac{1}{2}|H(j0)|^2 = \frac{1}{2}; \tag{C.2}$$

which leads to the definition of the cut-off frequency f_c:

$$f_c = \frac{A\sqrt{\sqrt{2}-1}}{2\pi} \tag{C.3}$$

The impulse invariance method may be applied to (C.1) to obtain a discrete-time equivalent filter. The steps involved in this transformation are:

- The continuous-time impulse response of the filter is:

$$h(t) = \mathcal{L}^{-1}\{H(s)\} = A^2 t e^{-At} \cdot u(t) \tag{C.4}$$

- Making the impulse response values $h(kT_s)$ of the digital filter equal to the sampled values of the impulse response of the analog filter, we have

$$h(kT_s) = A^2 kT_s e^{-AkT_s} \cdot u(kT_s) \tag{C.5}$$

- The discrete transfer function is

$$H(Z) = \sum_{k=0}^{\infty} A^2 kT_s e^{-AkT_s} Z^{-k}$$

$$= \frac{A^2 T_s Z^{-1} e^{-AT_s}}{(1 - Z^{-1} e^{-AT_s})^2} \tag{C.6}$$

If $\{x(k), k = 0, 1, ...\}$ is the input sequence to the filter, then the output sequence is obtained by expanding the above discrete transfer function into the standard difference equation form:

$$H(Z) = \frac{Y(Z)}{X(Z)} \tag{C.7}$$

$\Rightarrow$

$$Y(Z)\,[1 - 2e^{-AT_s}Z^{-1} + e^{-2AT_s}Z^{-2}] = X(Z)\,[A^2T_sZ^{-1}e^{-AT_s}] \tag{C.8}$$

$\Rightarrow$

$$y[k] = 2e^{-AT_s}y[k-1] - e^{-2AT_s}y[k-2] + A^2T_se^{-AT_s}x[k-1] \tag{C.9}$$

To reduce the effects of round-off errors, (C.9) was manipulated into a form in which the change in the filter output, rather than the output itself, is iterated each sampling interval.

Defining

$$E[k] = y[k] - y[k-1] \tag{C.10}$$

$$E[k-1] = y[k-1] - y[k-2]\,; \tag{C.11}$$

then the output can be expressed as

$$y[k] = E[k] + y[k-1]\,; \tag{C.12}$$

where $E[k]$ may be obtained from

$$E[k] = B_1\,y[k-1] + B_2\,E[k-1] + B_3\,x[k-1]\,; \tag{C.13}$$

where:

$$B_1 = -(1 - e^{-AT_s})^2 \tag{C.14a}$$

$$B_2 = e^{-2AT_s} \tag{C.14.b}$$

$$B_3 = A^2T_se^{-AT_s} \tag{C.14.c}$$

Equations C.3, C.12, and C.13 are the design relations for this filter.

For the real and imaginary components, the filter's output variance σ^2_{out} is given by:

$$\sigma_{out}^2 = \frac{T_s}{2\pi} \int_{-\pi/T_s}^{\pi/T_s} \sigma_{in}^2 |H(\omega)|^2 d\omega; \qquad \text{(C.15)}$$

where it is assumed that the input signal has a uniform power spectrum density.

Substituting $\sigma_{in}^2 = 1$ and $H(\omega) = H(Z)|_{Z = e^{\omega T_s}}$ in (C.15), we obtain

$$\sigma_{out}^2 = \frac{A^4 T_s^2 \cosh(AT_s)}{4\sinh^3(AT_s)} \qquad \text{(C.16)}$$

An output variance of one can then be obtained by multiplying each output samples by the square-root of the reciprocal of (C.16).

Bibliography

[AGAR90] AGARDograph no. AG-326, " *Radio Wave Propagation Modeling, Prediction and Assessment*", pp. 32-67, 1990.

[Bell88] P.A. Bello, "*Performance of Some Rake Modems Over the Non-Disturbed Wide Band Channel*", 1988 IEEE Military Communications Conference Record, vol. 1, pp. 4.3.1-4.3.7, October 1988.

[Bell65] P.A. Bello, "*Some Techniques for the Instantaneous Real-Time Measurement of Multipath and Doppler Spread*", IEEE Transactions on Communication Technology, vol. 13, no. 3, pp.285-292, September 1965.

[Bell63] P.A. Bello, "*Characterization of Randomly Time-Variant Linear Channels*", IEEE Transactions on Communications Systems, vol. CS-11, no. 4, pp. 360-393, December 1963.

[Belr88] J.S. Belrose and al., "*An Overview of Canadian Radio Propagation/Communications Technologies Research*", AGARD Conference Proceedings CP-442: Propagation Effects and Circuit Performance of Modern Military Radio Systems with Particular Emphasis on those Employing Bandspreading, pp. 2.1-2.30, NATO 1988.

[Bern91] A. Bernardini and al., "*Computer Simulation performance Evaluation in HF Radio Links: System and Coding Schemes Optimization*", Proceedings of the 5th Conference on HF Communications and Techniques, Conf. Pub. No. 339, pp.253-257, July 1991.

[Boit83] L. Boithias, "*Propagation des ondes radioélectriques dans l'environnement terrestre*", Paris: Dunod, 1983.

[Bray87] K. Brayer, "*HF Data Transmission: Lessons from the Past, Directions for the Future*", IEEE Journal on Selected Areas in Communications, vol. SAC-5, no. 2, pp. 90-101, February 1987.

[Budd61] K.G. Budden, "*Radio Waves in the Ionosphere*". Cambridge: University Press, 1961.

[CCIR90] CCIR, "*HF Ionospheric Channel Simulators*", Recommendations of the CCIR (1990), vol. III: Fixed Service at Frequencies Below About 30 MHz, Report 549-3, ITU, Geneva, 1990.

[CCIR82a] CCIR, "*Ionospheric Propagation Characteristics Pertinent to Terrestrial Radio Communication Systems Design (Fading)*", Recommendations and Reports of the CCIR (1982), vol. VI: Propagation in Ionized Media, Report 266-5, ITU, Geneva, 1982.

[CCIR82b] CCIR, *"Ionospheric Properties"*, Recommendations and Reports of the CCIR (1982), vol. VI: Propagation in Ionized Media, Report 725-1, ITU, Geneva, 1982.

[Chow82] S. Chow, J.K. Cavers, and P.F. Lee, *"A Spread Spectrum Modem for Reliable Data Transmission in the High Frequency Band"*, Proceedings of the 2nd Conference on HF Communications and Techniques, IEE 206, pp. 125-130. February 82.

[Clar89] A.P. Clark and S. Hariharan, *"Adaptive Channel Estimator for an HF Radio Link"*, IEEE Transactions on Communications, vol. 37, no. 9, pp. 918-926. September 1989.

[Cohn68] D.L. Cohn, A.H. Levesque, and al.. *"Performance of Selected Block and Convolutional Codes on a Fading HF Channel"*, IEEE Transactions on Information Theory, vol. IT-14, no. 5, pp. 627-640. September 1968.

[Davi65] K. Davies, *"Ionospheric Radio Propagation"*. National Bureau of Standards Monograph 80, 1965.

[Daws84] J. Dawson. *"An HF Simulator for use with Real-Time Channel Evaluation Systems"*, AGARD Conference Proceedings CP-363: Propagation Influences on Digital Transmission Systems: Problems and Solutions, pp. 24.1-24.15, NATO 1984.

[Dhar82] S. Dhar and B.D. Perry, *"Equalized Megahertz-Bandwidth Channels for Spread Spectrum Communications"*, 1982 IEEE Military Communications Conference Record, vol.2, pp. 29.5.1-29.5.5. October 1982.

[Ehrm82] L. Ehrman, L.B. Bates, J.F. Eschle, and J.M. Kates, *"Real-Time Simulation of the HF Radio Channel"*, IEEE Transactions on Communications, vol. COM-30, no. 8, pp.1809-1816, August 1982.

[Gong90] K.S. Gong, M.T. Lyons, and R.R. Kurth, *"A Frequency Tracking Demodulator for Multipath Channels"*, 1990 IEEE Military Communications Conference Record, vol. 2, pp. 50.2.1-50.2.5, September 1990.

[Good90] J.M. Goodman and J. Aarons, *"Ionospheric Effects on Modern Electronic Systems"*, Proceedings of the IEEE, vol. 78, no. 3, pp. 512-527, March 1990.

[Gott91] G.F. Gott, *"HF Systems Operating Beneath the Ionosphere"*, AGARD Lecture Series LS-172: Propagation Limitations for Systems Using Band-Spreading, pp. 5.1-5.27, NATO 1991.

[Hoff91] J.A. Hoffmeyer, L.E. Vogler, J.F. Mastrangelo, L.E. Pratt, and C.J. Behm, *"A New HF Channel Model and its Implementation in a Real-Time Simulator"*, IEE Proceedings of the 5th International Conference on HF Radio Systems and Techniques, pp. 173-177, July 1991.

[Jeru92] M.C. Jeruchim, P. Balaban, and K.S. Shannugan, *"Simulation of Communication System"*. New-York: Plenum Press, 1992.

[Kane90] R.E. Kane Jr., K.S. Gong, and R.R. Kurth, *"Performance of a RAKE Demodulator with Pre-Decision Multipath Thresholding"*, 1990 IEEE Military Communications Conference Record, vol. 2, pp. 50.3.1-50.3.5, September 1990.

[Kels64] J.M. Kelso, *"Radio Ray Propagation in the Ionosphere"*. New-York: McGraw-Hill, 1964.

[Lemm90] J.J. Lemmon, *"Recent Progress in the Development of a Wideband HF Noise/Interference Model"*, 1990 IEEE Military Communications Conference Record, vol. 3, pp. 60.1.1-60.1.10, September 1990.

[Lin90] K.H. Lin and K.C. Yeh, *"Some Measured Properties of the Ionosphere Reflection Channel at High Frequencies"*, 1990 IEEE Military Communications Conference Record, vol. 3, pp. 60.3.1-60.3.6, September 1990.

[Lin83] S. Lin and D.J. Costello, *"Error Control Coding, Fundamentals and Applications"*. Prentice-Hall. 1983.

[Low82] J. Low and S.M. Waldstein, *"A Direct Sequence Spread-Spectrum Modem for Wideband HF Channels"*, 1982 IEEE Military Communications Conference Record, vol.2, pp. 29.6.1-29.6.6. October 1982.

[Maca91] R.C.V. Macario, *"Personal & Mobile Radio System"*. London: Peter Pergrinus Ltd, 1991.

[Mala85] A. Malaga, *"A Characterization and Prediction of Wideband HF Skywave Propagation"*, 1985 IEEE Military Communications Conference Record, vol. 1, pp. 12.5.1-12.5.8, October 1985.

[Mala81] A. Malaga, *"A Global Model Wideband HF Skywave Propagation"*, Proceedings of IES'81, pp. 1-12, April 1981.

[Masl87] N.M. Maslin, *"HF Communications: A Systems Approach"*. New-York: Plenum Press, 1987.

[Masl82] N.M. Maslin, *"High Data Rate Transmissions Over HF Links"*, The Radio and Electronics Engineer, vol. 52, no. 2, pp. 75-87, February 82.

[Mast91] J. Mastrangelo, J. Hoffmeyer, C. Behm, and L. Pratt, *"A New HF Simulation System for Testing HF Radios"*, 1991 IEEE Military Communications Conference Record, vol. 3, pp.49.5.1-49.5.6, November 1991.

[Merz70] E. Merzbacher, *"Quantum Mechanics"*. New-York: John Wiley & Sons, 1970.

[Mons80] P. Monsen, *"Fading Channel Communications"*, IEEE Communications Magazine, vol. 18, no. 1, pp. 16-25, January 1980.

[Ochs87] H. Ochsner, *"Direct-Sequence Spread-Spectrum Receiver for Communication on Frequency-Selective Fading Channels"*, IEEE Journal on Selected Areas in Communications, vol. SAC-5, no. 2, pp. 188-193. February 1987.

[ORei82] E.P. O'Reilly, *"A Real-Time HF Channel Simulator"*, Proceedings of the 2nd Conference on HF Communications and Techniques, IEE 206, pp. 41-45. February 82.

[Papo84] A. Papoulis, *"Probability, Random Variables and Stochastic Processes"*. New-York: McGraw-Hill, 1984.

[Perl86] J.M. Perl and D. Kagan, *"Real-Time HF Channel Parameter Estimation"*, IEEE Transactions on Communications, vol. COM-34, no. 1, pp. 54-58, January 1986.

[Perr87] B.D. Perry, E.A. Palo, R.D. Haggarty, and E.L. Key, *"Trade-Off Considerations in the Use of Wideband HF Communications"*, 1987 IEEE International Communications Conference Proceedings, vol. 2, pp. 26.2.1-26.2.11. June 1987.

[Perr83] B.D. Perry, *"A New Wideband HF Technique for MHz-Bandwidth Spread-Spectrum Radio Communications"*, IEEE Communications Magazine, vol. 21, no. 6, pp. 28-36, September 1983.

[Perr82] B.D. Perry, *"Megahertz Bandwidth HF Skywave Communications Techniques"*, Proceedings of the 2nd Conference on HF Communications and techniques, IEE 206, pp. 91-95, February 82.

[Pric58] R. Price and P.E. Green, *"A Communication Technique for Multipath Channels"*, Proceedings of the IRE, vol. 46, no. 2, pp. 555-570, March 1958.

[Proa89] J.G. Proakis, *"Digital Communications"*. New-York: McGraw-Hill, 1989.

[Purs87] M.B. Pursley, *"The Role of Spread Spectrum in Packet Radio Networks"*, Proceedings of the IEEE, vol. 75, no. 1, pp. 116-134. January 1987.

[Rifk90] R. Rifkin and B.D. Perry, *"Bandwidth Effects of Signal Fading for the Mid-Latitude HF Channel"*, 1990 IEEE Military Communications Conference Record, vol. 3, pp. 60.4.1-60.4.8, September 1990.

[Rush86] C.M. Rush, *"Ionospheric Radio Propagation Models and Predictions - A Mini-Review"*, IEEE Transactions on Antennas and Propagation, vol. AP-34, no. 9, pp. 1163-1170, September 1986.

[Salo86] S. Salous and E.D.R. Shearman, *"Wideband Measurements of Coherence over an HF Skywave Link and Implication for Spread Spectrum Communication"*, Radio Science, vol. 21, No. 3, pp.463-472. May-June 1986.

[Schw66] M. Schwartz, W.R. Bennett, and S. Stein, *"Communication Systems and Techniques"*, vol. 4. New-York: Inter-University Electronic Series, McGraw-Hil, 1966.

[Simo85] M.K. Simon and al., *"Spread Spectrum Communications"*, vol. 1. Rockville MD: Computer Science Press, 1985.

[Stei87] S. Stein, *"Fading Channel Issues in System Engineering"*, IEEE Journal on Selected Areas in Communications, vol. SAC-5, no. 2, pp. 68-89, February 1987.

[Turi80] G.L. Turin, *"Introduction to Spread-Spectrum Antimultipath Techniques and Their Application to Urban Digital Radio"*, Proceedings of the IEEE, vol. 68, no. 3, pp. 328-353. March 1980.

[Vite91] A.J. Viterbi, *"Wireless Digital Communications: A View Based on Three Lessons Learned"*, IEEE Communications Magazine, vol. 29, no. 9, pp. 33-36. September 1991.

[Vite76] A.J. Viterbi, *"Spread Spectrum Communications - Myths and Realities"*, IEEE Communications Magazine, vol. 14, no. 5, pp. 11-18. May 1976.

[Vogl90] L.E. Vogler and J.A. Hoffmeyer, *"A New Approach to HF Channel Modeling and Simulation - Part II: Stochastic Model"*, NTIA Report 90-255, February 1990.

[Vogl88a] L.E. Vogler and J.A. Hoffmeyer, *"A New Approach to HF Channel Modeling and Simulation - Part I: Deterministic Model"*, NTIA Report 88-240, December 1988.

[Vogl88b] L.E. Vogler, J.A. Hoffmeyer, J.J. Lemmon, and M. Nesembergs, *"Progress and Remaining Issues in the Development of a Wideband HF Channel Model and Simulator"*, AGARD Conference Proceedings CP-442: Propagation Effects and Circuit Performance of Modern Military Radio Systems with Particular Emphasis on those Employing Bandspreading, pp. 6.1-6.19, NATO 1988.

[Wagn89] L.S. Wagner, P.A. Bello, and al., *"The Skywave Channel: Measured Scattering Functions for Midlatitude and Auroral Channels and Estimates for Short-Term Wideband HF Rake Modem Performance"*, 1989 IEEE Military Communications Conference Record, vol. 1, pp. 48.2.1-48.2.10, October 1989.

[Watt70] C.C. Watterson, J.R. Juroshek, and W.D. Bensema, *"Experimental Confirmation of an HF Channel Model"*, IEEE Transactions on Communication Technology, vol. COM-18, no. 6, pp. 792-803, December 1970.

[Ziem85] R.E. Ziemer and R.L. Peterson, *"Digital Communications and Spread Spectrum Systems"*. New-York: Macmillan Publishing Company, 1985.